Master Degree Thesis in Nuclear Physics

Department of Physics and Technology

University of Bergen

Simulations of a Therapeutic Proton Beam with FLUKA Monte Carlo Code and Varian Eclipse Proton Planning Software

Author:
Kine Johnsen
Supervisors:
Professor Dieter Röhrich
Dr. Scient. Odd Harald Odland

November 20, 2013

Acknowledgements

I would like to express my gratitude towards my supervisors, Professor Dieter Röhrich and Dr. Scient. Odd Harald Odland.

Professor Dieter Röhrich, your inspiring lectures aroused my initial interest towards this topic, and throughout the course of this project you have enabled me to gain new knowledge and to work with many interesting people. Thank you for your guidance and for our clarifying conversations.

Thank you Dr. Scient. Odd Harald Odland for your guidance and encouragement during this project. Your thorough supervision and comprehensive feedback have been most valuable for the execution and completion of this work. Thank you for introducing me to Haukeland University Hospital (HUS), and providing me with the possibility to work with, and learn from, a lot of great people.

Thanks to Camilla Hanquist Stokkevåg, Kristian Ytre-Hauge and Grete May Engeseth for being utmost helpful and supportive. Thank you Professor Ludvig Muren for good advice and suggestions along the way. Thanks also to Jostein Sæterstøl and Kristine Fasmer at the Medical Physics Section at HUS for your encouragement.

A great thank you to Daniel Aadnevik for your insightful input and for always taking your time to help me with challenges occurring along the way, both technical and scientific. I appreciate our friendship, and I wish you all the best for your future endeavours. To my fellow students; Julia, Tonje, Tordis, Agnethe, Christer, Tjalve, Steffen and Rune; thank you for your friendship and companionship during our years at UiB.

A special thanks to my parents, Laura and Holm Eirik Johnsen, for endless encouragement, support and baby sitting services. Thanks to Solbjørg and Berge Aadland; you are always helpful and supportive, and for that I am forever grateful.

And finally I would like to thank the two most important people in my life; Jostein, your patience and unconditional support are beyond my comprehension, and my baby boy Ask; your smiles and hugs are my source of inspiration.

Abstract

The goal of radiation therapy is to eradicate the cancer cells by delivery of a high enough dose of ionizing radiation to the tumour, while at the same time sparing the surrounding healthy tissue. This dual purpose has motivated the development of hadron therapy.

The sharp dose deposition from protons in a medium has some clear advantageous aspects for use in cancer treatment. When charged particles, for instance protons, traverse matter, most of their energy are deposited at the end of their range, causing a sharp peak, the Bragg peak, at a depth determined by the proton range in the medium. This range is a function of the initial proton energy and of the characteristics of the traversed medium.

Treatment techniques for delivery of proton therapy have evolved from passive scattering systems into sophisticated beam spot scanning techniques, providing additional degrees of freedom for the treatment delivery. In order to deliver a precise and efficient treatment to a patient, it is vital to calculate the dose distribution from protons applying an accurate calculation of the proton range in the patient. A well defined range of the proton beam is not only the characteristic that makes protons beneficial for cancer treatment, it is also the characteristic that makes the method vulnerable for uncertainties. Computer simulations are frequently used to estimate the proton range and the associated dose deposition in a patient. The Monte Carlo simulation method is optimal for estimating particle transport in matter, and thus it can serve as the tool to enable detailed knowledge about dose deposition in a medium, and hence in a patient. However, Monte Carlo simulations can be time consuming and thus not compatible with the clinical demands. In most dose planning programs applied in the clinical routine, somewhat simpler algorithms than Monte Carlo simulations are used to create the dose distributions in treatment plans. These algorithms calculate the dose distribution partly based on mathematical models for dose distribution and partly based upon input from Monte Carlo simulations and the calculated dose is

calculated from a geometry input generated by the attenuation of photons in a CT voxel geometry.

The purpose of this project has been to apply Monte Carlo software to simulate a proton beam resembling a therapeutic beam, and to study the interactions of this beam in phantoms of various design. The simulations were produced with FLUKA Monte Carlo code version 2011 2b. Further the purpose has been to apply Varian Eclipse proton planning (version 11) software to create treatment plans on similar phantoms, in order to study the differences between a time-effective, clinically optimized tool and an accurate, yet time consuming, Monte Carlo simulation tool.

A fundamental criteria for a therapeutic beam is that the beam must have the ability to deliver a homogeneous dose to an extended volume. To meet this criteria, the energy of the applied protons must be spread out in order to create a plateau of dose covering the target volume, which is the tumour with some specified margins. This implies that an otherwise monoenergetic beam needs to be energy modulated in order to produce a weighted energy spectrum, resulting in a spread-out Bragg peak (SOBP). In this project, two different approaches were followed in order to obtain a dose deposition with a flat dose plateau at the desired depth. By (1) passively modulating the beam range by inserting material into the simulated beamline, which is the equivalent of the use of a range modifier positioned in the beamline, and by (2) actively modulating the proton energy from the beam source. The resulting dose distributions from these two approaches showed that the dose falloff at the distal part of the target volume was sharper with the active energy modulation approach than when passively using material to modulate the beam energy.

In treatment planning, the stoichiometric method is used to obtain an approximated relation between the CT deduced Hounsfield Unit value and the proton stopping power. With the stoichiometric method the CT value of a given human tissue is coupled to the proton stopping power, calculated using known physical parameters of the medium such as physical density, elemental composition and mean ionization energy. Since the CT Hounsfield Unit value and the proton stopping power reflects different physical interactions, ie attenuation of a photon beam versus energy deposition of a proton beam, this relation is not straightforward or one-to-one in general. Thus, there is an uncertainty in a proton range calculation based on CT images. With Monte Carlo codes for particle transport, one can model the geometry in an accurate way, assigning materials with its elemental composition and their

physical properties.

The final goal of this project was obtained by the use of a commercial treatment planning system to produce simple treatment plans, and further; to compare the dose profiles to similar treatment plans created with a Monte Carlo simulated beam and geometry. The overall agreement between the two calculation methods were adequate, especially with respect to dose coverage within the defined target volume. However, when introducing different materials such as bone, air and aluminium into the geometry, the differences between the two methods became apparent and it illustrates the tentative limitations of a fast, clinical optimized, dose planning tool compared with a more accurate and detailed, hence tentatively slower, Monte Carlo simulation tool.

Contents

Chapter 1

Introduction

Cancer is a generic term for a large group of diseases that can affect any part of the body. Two defining features of cancer are; 1) the occurrence of abnormal cells that divide without control, and; 2) the cancer cells have a metastatic feature, and thus, if not treated, these may invade other organs and healthy tissue. Cancer is a leading cause of death worldwide, accounting for 7.6 million deaths in 2008 [1]. About half of all cancer patients in Norway are treated with radiation therapy [2]. The number of patients undergoing radiation therapy in Norway in 2010 was 11370 [3].

The goal of radiation therapy is to inactivate cancer cells by delivery of a high enough dose to the tumor, while at the same time spare the surrounding healthy tissue. Ever since Roentgens' discovery of X-rays in 1895, efforts have been made to reach this goal. Especially the development of sophisticated medical imaging modalities, such as CT, MRI and PET, has provided a huge leap forward in better dose delivery in radiation therapy.

The most common and widespread modality within radiation therapy is external radiation therapy, ie irradiation of a patient from the outside, and this with the use of photons. Photons in the MeV energy range are produced in medical linear accelerators and aimed towards the target volume. Following the development of better imaging techniques and improved computing power, innovations such as Intensity-Modulated Radiation Therapy (IMRT) and Volumetric-Modulated Arc Therapy (VMAT) has made it possible to produce quite complex dose plans optimized in order to deliver the desired dose to the tumour, and at the same time minimize the dose to healthy tissue and organs surrounding the tumour.

In particle therapy, the physical properties of charged particles, such as pro-

tons or heavier ions are utilized to irradiate the defined target volume. As early as 1946, the American physicist Dr. Robert Wilson suggested that proton beams could be used to treat cancer. He argued that protons had therapeutic advantages over photons due to their superior depth-dose characteristics [4] [5]. The first proton therapy facilities where mainly physics research laboratories. In Scandinavia, Uppsala University in Sweden treated their first patient with protons as early as in 1957. Now there exists several dedicated particle facilities for cancer treatment, most of them proton facilities. Many future facilities are currently on the sketch board. In September 2013, the Norwegian Minister of health announced that there will be established proton therapy facilities at the University Hospitals in the administrative health regions in Norway.

Before the patient starts receiving radiation therapy treatment, many steps have to be taken. Diagnostic medical imaging is performed, and an oncologist determines and defines the volume to be treated. A treatment planning program is used to determine how the target volume should be irradiated to achieve the best possible and satisfactory dose distribution. A 3D Computed Tomography (CT) image set is imported into the treatment planning program. The CT image consists of information from voxels representing the X-ray radiation absorption in each voxel, each representing a position in the part of the human body that is imaged. The dose distribution from the radiation is calculated based on how the radiation interacts with the material, applying a normalized Hounsfield Unit scale representing the density of the material in each voxel.

An accurate calculation of the dose in the patient is one of the keys to a successful treatment, especially during particle therapy where the longitudinal dose gradients are very sharp. To make an accurate prediction of the proton range in the human body valid during each treatment fraction can be complicated due to varying physical properties in bone, gas and liquids, and given the movement and variations that continuously occur in the human body. In this project a therapeutic proton beam will be modelled and investigated using the FLUKA Monte Carlo simulation tool and the Varian Eclipse Proton planning system, as applied at Haukeland University Hospital.

The overall goals for this project has been:

- Investigate how various materials such as bone, air and metal influence the proton behavior in an otherwise homogeneous water phantom by using a Monte Carlo simulated monoenergetic proton pencil beam.

- With the same Monte Carlo program, create a spread-out Bragg peak (SOBP) suitable for treatment of an extended volume inside the phantom, by modulating the beam energy applying both passive and active methods and then comparing the two methods.
- Creating basic treatment plans with the Varian Eclipse treatment planning software and with the FLUKA Monte Carlo tool and compare the dose profiles and dose distributions calculated by the two methods when irradiating a similar phantom in both systems.

In **Chapter 2** the basic physics most relevant for radiation therapy is presented. This includes interactions of photons and charged particles with matter. In this chapter there will be a short summary of radiation biology and the introduction of properties such as linear energy transfer (LET) and relative biological effectiveness (RBE).

Chapter 3 addresses radiation therapy. The chapter begins with a description of medical imaging used in radiation therapy. A short explanation about photon therapy and its radiation source (the linear accelerator) and treatment techniques is followed by a more comprehensive description of radiation therapy with protons.

A general summary of the Monte Carlo method is presented in **Chapter 4**.

In **Chapter 5** the method, procedures and results of this project are outlined. A short description of FLUKA and Eclipse, the software used to perform the simulations, is given. Further, the simulation set-ups and the results of each simulation are addressed.

Finally the conclusion and outlook is given in **chapter 6**.

All FLUKA Monte Carlo simulations shown in this thesis is produced by the author, unless otherwise specified.

Chapter 2

Radiation Physics

In this chapter the basic radiation physics most relevant for radiation therapy will be presented. In general, as radiation penetrates matter, several interaction mechanisms will be invoked and a variety of interactions can occur, all depending on the characteristics of both the projectile traversing the matter and the matter itself. Parameters most prominent in governing the interaction between radiation and matter are; the type of radiation, the energy and electrical charge of the incoming radiation, and material properties such as physical density, elemental composition and mean ionization energy. In the case of irradiation with photons and charged particles, as is the situation during radiation therapy, the electromagnetic interactions are the dominating processes [6].

2.1 Interactions of Photons with Matter

A photon is a quantum gauge particle carrying electromagnetic energy, and it is considered a neutral, massless particle. As the photon wavelength drops to lower than about $10^{-11} - 10^{-12}$ m the photon energy will be such that the photon is in the X-ray and gamma (γ) part of the electromagnetic spectrum. When passing through tissue, γ photons can be scattered and absorbed, leading to a decrease in the radiation intensity. This attenuation of the beam depends on the material it traverses. The intensity can be calculated by the following formula:

$$I = I_0 e^{-\mu x} \tag{2.1}$$

Here I is the intensity at a certain depth, x, I_0 is the initial intensity, x $[cm]$ is the thickness of the given material and μ $[cm^{-1}]$ is the linear attenuation coefficient of the given material. The linear attenuation coefficient decreases with energy of the γ and increases with atomic number and density of the absorber. The fraction of the photons transmitted is represented by the factor $e^{-\mu x}$. The photon beam will, to first order, not experience a decrease in energy, only an attenuation of its intensity [7]. However, if a photon beam with an energy spectrum enters an absorber material, there will be a "beam hardening" effect as a function of depth in the absorber; the low energy photons being attenuated more rapidly than the high energy photons.

The three main processes leading to this attenuation of intensity are:

1. Photoelectric Effect
2. Compton Scattering
3. Pair Production

These processes will lead to either scattering or absorption of the photon, thus removing the photon from its original path and, by this, reducing the beam intensity. In figure 2.1 these three processes are illustrated. A fraction of the photons in a photon beam will not undergo any interactions, due to the stochastic and statistical nature of the fundamental interaction mechanisms in nature, these photons will emerge unscattered beyond an absorber. The probability, or cross section, of each of these processes depends on the photon energy and the material it traverses, as can be seen in figure 2.2. The cross section is used as a measure of the likelihood for a given interaction [6].

2.1.1 Photoelectric Effect

The incoming photon can interact with an orbital electron of the absorber atom, causing the atom to eject the electron, called the photoelectron. The photoelectron will have a kinetic energy determined by the photon energy and by the electrons' binding energy:

$$E_{kin} = E_{\gamma} - E_{binding} \tag{2.2}$$

The cross section for the photoelectric effect depends on the energy of the photon and on the atomic number Z of the target material. The Z-dependence goes as Z raised to between 4th to the 5th power [6] (p. 55). In diagnostic X-ray images this effect is utilized, showing a sharp contrast between material with different densities, such as bone and tissue.

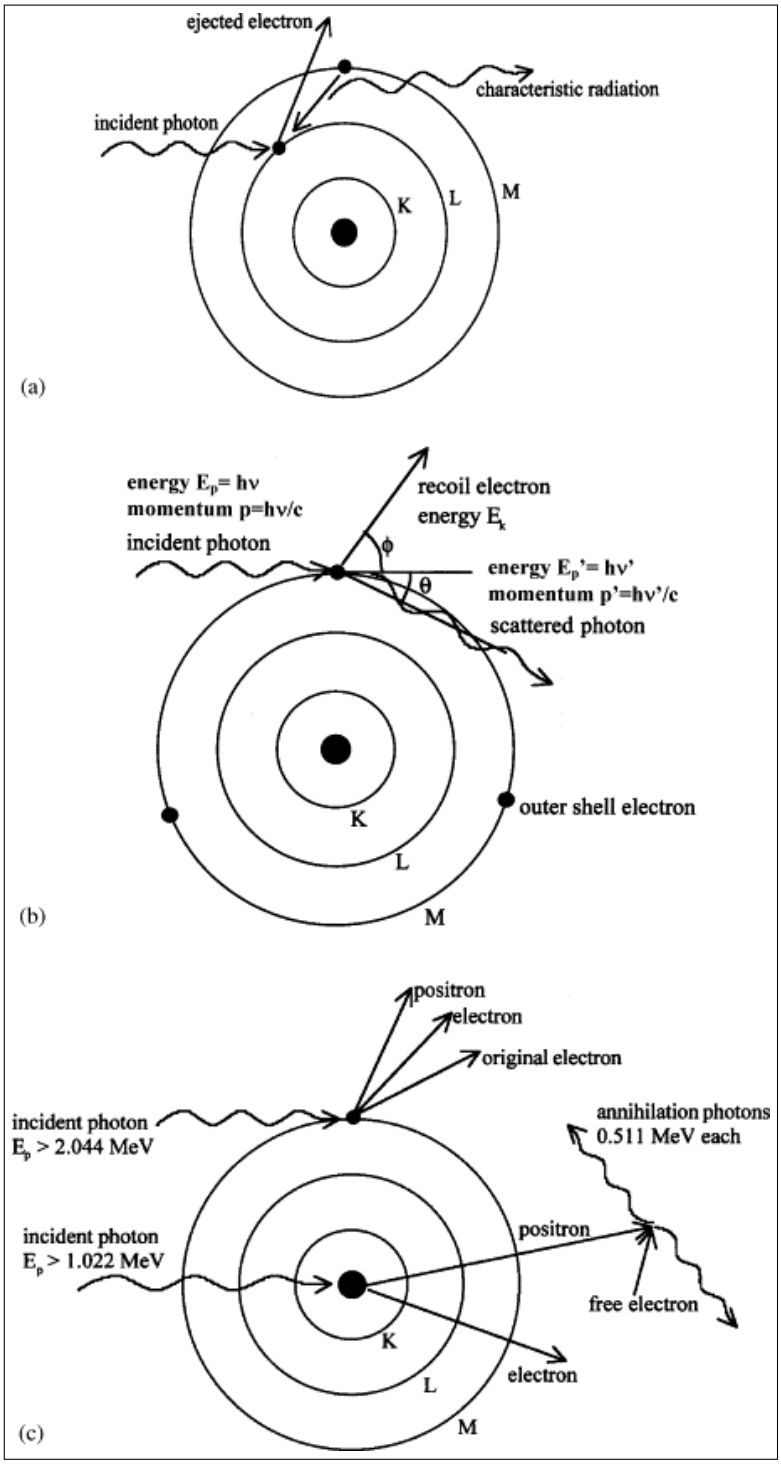

Figure 2.1: The three main interactions between photons and matter [8]. a) The Photoelectric effect, b) Compton scattering, and c) Pair production.

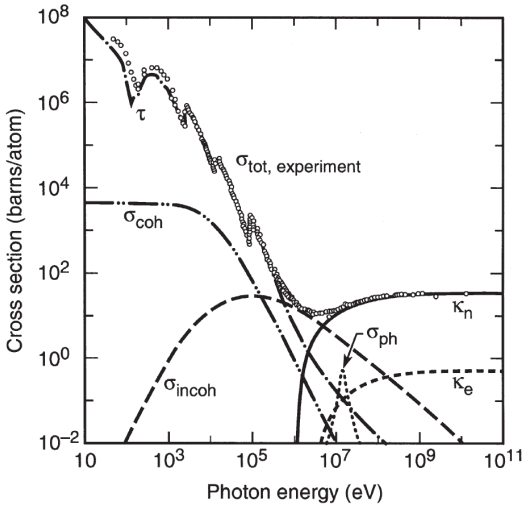

(a) Fundamental photon processes in lead.

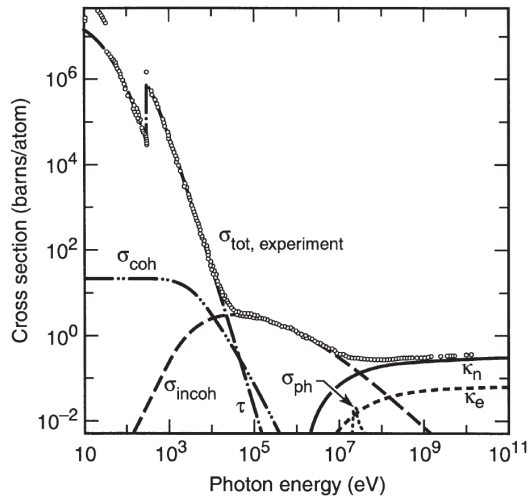

(b) Fundamental photon processes in carbon.

Figure 2.2: The total photon cross section in (a) lead and (b) carbon as a function of energy [9]. The cross section for the photoelectric process dominates for the lowest energies, the keV range, while the cross section for pair production becomes dominating for higher energies, starting at 1.022 MeV. The Compton cross section reaches its maximum in the MeV range.

2.1.2 Scattering

Compton scattering is the process where the photons get scattered off a loosely bound electron. The kinematics of this process is given by the conservation of momentum and energy.

$$\begin{aligned} E_\gamma &= h\nu, \\ h\nu' &= \frac{h\nu}{1+\gamma\,(1-cos\theta)}, \\ E_e &= h\nu - h\nu' = h\nu\frac{\gamma\,(1-cos\theta)}{1+\gamma\,(1-cos\theta)} \end{aligned} \tag{2.3}$$

The cross section for Compton scattering depends on the electron density of the material traversed. Since the Z-dependence is not as strong as it is for the photoelectric effect, imaging with photons in the Compton range will not produce as sharp images as when using photons in the photoelectric energy range. The difference between kV and MV images is illustrated in figure 2.3. For therapeutic purposes, the energy of the photons is in the MeV region, the energy region where the cross sections for Compton scattering and pair production are dominating.

In addition to Compton scattering, photons can undergo what is known as Rayleigh scattering or coherent scattering. In Rayleigh scattering the photon passes near an atomic electron, setting it into oscillation. The electron will reradiate the energy at the same frequency as the incident photon. Thus the only effect of this process is the scattering of the photon at a small angle. Rayleigh scattering occurs in high-Z materials and at low photon energies [11].

2.1.3 Pair Production

When the photon energy is above 1.022 MeV, which is twice the rest mass of an electron, the process of pair production can occur. This process involves the production of an electron-positron pair. This interaction becomes dominant as the photon energy increases above the threshold energy. This interaction becomes dominant as the photon energy increases above the threshold energy, as can be seen in figure 2.2.

2.1.4 Neutron Production

In addition to the processes mentioned above, photons can also undergo interactions producing neutrons. In photon therapy the photons will interact

Figure 2.3: Comparison of the kV CT slice (left) and MV cone beam CT (right) of the head-and-neck patient for three orthogonal views [10].

with the beamline components and with the patient's body, producing secondary particles such as neutrons. Neutron production can be significant, especially during radiation treatment applying techniques that involves collimation material in the beamline during irradiation, such as dynamic Multi Leaf Collimators (MLCs) and/or having placed collimation devices and other beamline equipment close to the patient [12] [13]. The advanced techniques applying dynamic MLC motion, such as IMRT and VMAT, will be addressed in chapter 3.

2.2 Interactions of Charged Particles with Matter

Charged particles interact with matter in a different way than photons. When travelling through matter the projectile particle will either lose energy or be deflected from its original path through the interactions that take place. This results mainly from inelastic collisions with atomic electrons and elastic scattering from nuclei. Other processes that can occur are emission of Čerenkov radiation, nuclear reactions and bremsstrahlung, but these are rare compared to the incident rate of collisions for charged particles such as protons. Bremsstrahlung is the dominating process for electrons and positrons traversing matter [6].

The interactions are mediated by the Coulomb force between the electric field of the projectile particle and the electric field within the atom. In addition to the Coulomb force, nuclear reactions occur for heavier particles than electrons and positrons. When a beam of protons pass through matter, for instance a human body, there will be produced short-lived radioisotopes such as ^{11}C, ^{13}N and ^{15}O due to nuclear fragmentation processes.

In the case of the inelastic collisions, energy will be transferred from the projectile particle to the atom by ionization or excitation. The average energy loss per unit path length, $\frac{dE}{dx}$, is given by the Bethe-Bloch formula (equation 2.4). In figure 2.4 the stopping power in various media is plotted against momentum. The mass stopping power is the energy loss per unit track length divided by the material density, $-\frac{dE}{dX} = -\frac{1}{\rho}\frac{dE}{dx}$.

The Bethe-Bloch formula reads;

$$-\frac{dE}{dx} = 2\pi N_a r_e^2 m_e c^2 \rho \frac{Z}{A}\frac{z^2}{\beta^2}\left[ln\left(\frac{2m_e\gamma^2 v^2 W_{max}}{I^2} - 2\beta^2 - \delta - 2\frac{C}{Z}\right)\right] \quad (2.4)$$

r_e: classical electron radius = 2.817×10^{-13} cm
m_e: electron mass = 511 MeV/c^2
N_a: Avogadros's number = 6.022×10^{23} mol^{-1}
I: mean excitation potential
Z: atomic number of absorbing material
A: atomic weight of absorbing material
ρ: density of absorbing material
z: charge of incident particle in units of e
β: $\frac{v}{c}$ of the incident particle
γ: $\frac{1}{\sqrt{1-\beta^2}}$
δ: density correction
C: shell correction
W_{max}: maximum energy transfer in a single collision

As can be seen from equation 2.4; when the traversing particle slows down, the particle will deposit more energy per unit of length. The result of this velocity dependency is that most of the particles' energy will be deposited at the end of the particle range, just before it stops completely. One will see a sharp dose enhancement, the Bragg peak, as the particle stops. When the particle beam is monoenergetic this peak will be very sharp. Due to the statistic nature of the processes mentioned above there will be a distribution in where monoenergetic particles come to rest, some particles will stop before others, this is referred to as range straggling, thus giving the Bragg peak a finite thickness. The proton is a nuclear particle with charge +1e and it has a mass of 938 MeV/c^2. In figure 2.5 the longitudinal dose profile for proton beams of three different energies are displayed. Figure 2.6 shows the dose deposition in 2D color wash of a 150 MeV proton beam simulated in FLUKA. As seen in the Bethe-Bloch formula, this process also depends on the square of the particle charge. Thus for heavier nuclei such as ^{12}C this effect is even more pronounced [11] [15].

Multiple Coulomb Scattering

As the charged particle traverses the matter it can undergo repeated elastic Coulomb scattering from nuclei. Due to the large mass of the nuclei compared to the incoming particle, the energy transfer is negligible, however the direction of the particle can alter. This results in divergence of the beam.

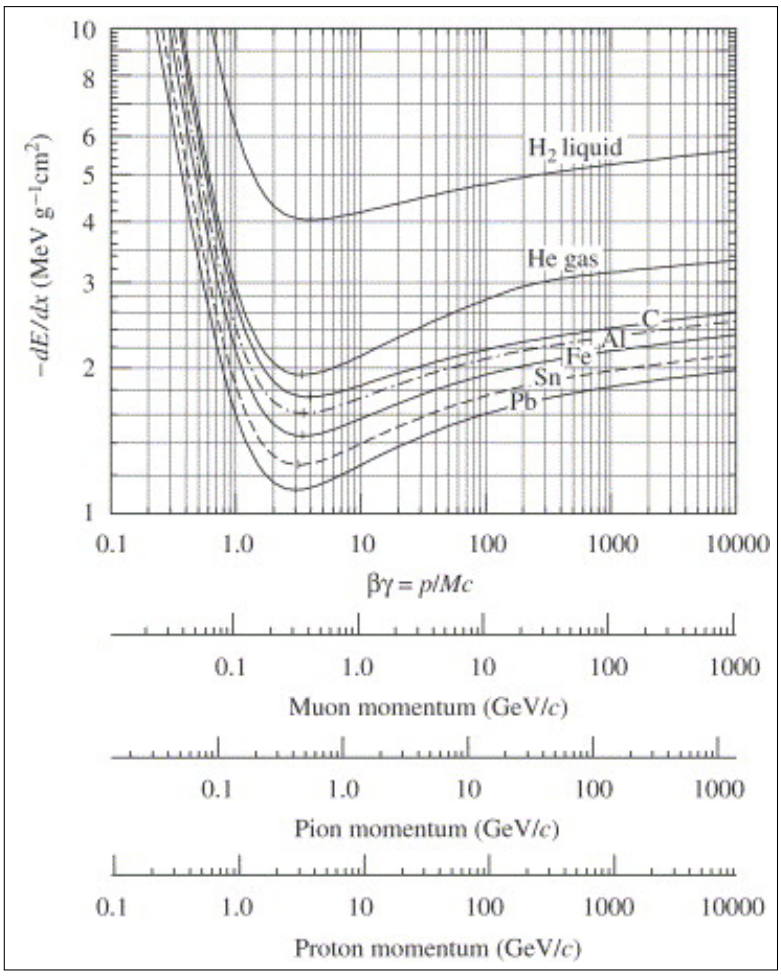

Figure 2.4: The stopping power $-\frac{dE}{dX}$ in different materials [14].

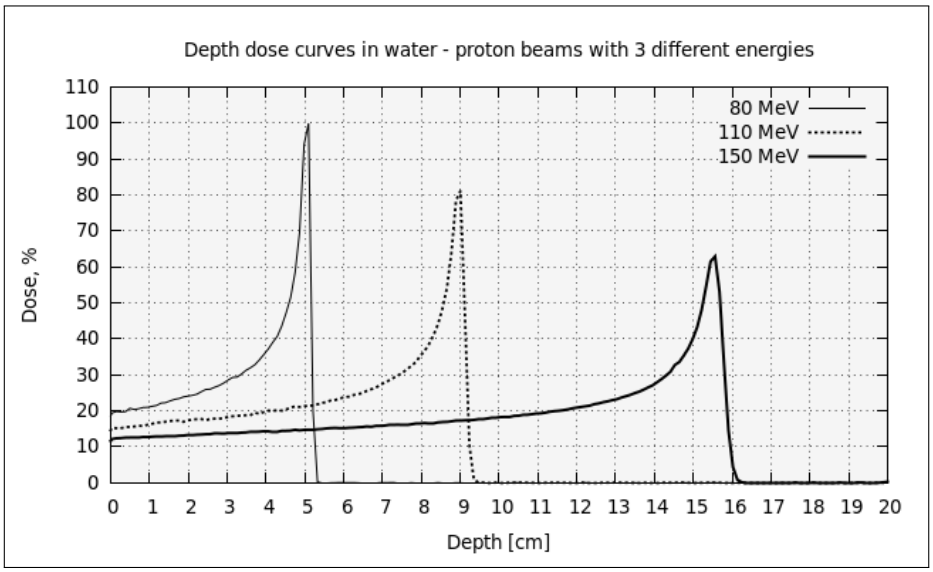

Figure 2.5: FLUKA Monte Carlo simulation. Dose deposition from 3 proton pencil beams with the energies; 80 MeV, 110 MeV and 150 MeV.

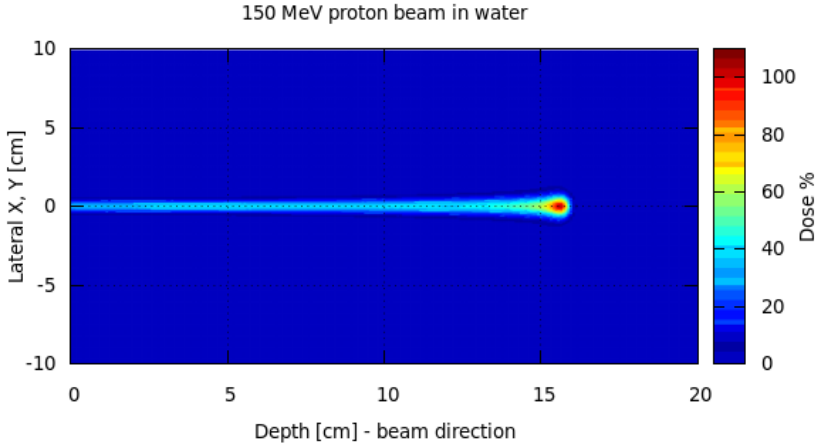

Figure 2.6: FLUKA Monte Carlo simulation. The 2D projection of dose deposition in water from a 150 MeV proton pencil beam.

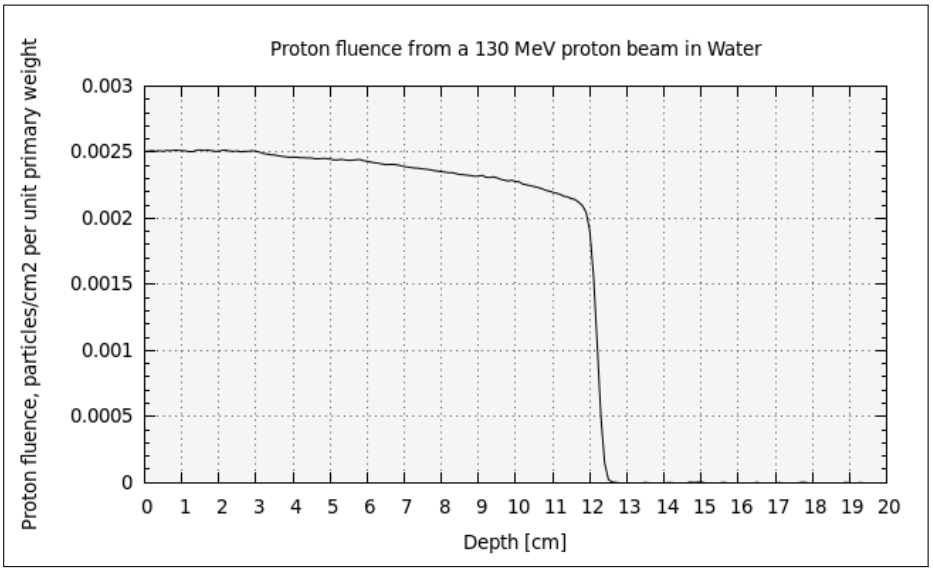

Figure 2.7: FLUKA Monte Carlo simulation. Proton fluence from a 130 MeV pencil beam in water. The unit for the fluence in FLUKA is particles pr area (cm^2) pr primary particle [16].

Nuclear Reactions

Charged particles can interact with matter via nuclear reactions. This is rare, and can be neglected when the initial kinetic energy is lower than the Coulomb barrier.

Fluence

The fluence, Φ , is defined as the number of particles crossing an infinitesimal element of area dA normal to z (beam direction).

$$\Phi = \frac{dN}{dA} \tag{2.5}$$

For a beam of protons, the fluence of primary protons is very consistent towards the Bragg peak. The reduction of proton fluence is about 1-2 % per cm in water, as illustrated in figure 2.7 [15].

2.3 Radiation Biology

Radiation biology is invoked when quantifying the relationship between a physical absorbed dose in the tissue, and the resulting effect. There is yet

not enough systematic data for a comprehensive description of the dose response relationship for human beings, hence no unambiguous limit of dose tolerance is known, but experiments on animals and records of dose exposure and casualties in historical events, such as the atomic bombs in Japan 1945, have displayed a range of doses during which the risk of damage increases from 0 % to 100 % as a function of increasing dose. A diagram displaying the effect of irradiation as a function of dose is commonly known as the dose-response curve.

The clinical most important impact of radiation is caused by ionization. It is the ability of ionization of the medium traversed that makes the particles attractive for treatment of cancer, since the ionization can cause damage to the DNA molecules in a cell. Radiation causes damage to the DNA by breaking one or both molecular strands. Cells are regarded as killed when they have lost their reproductive ability.

2.3.1 Linear Energy Transfer (LET)

The linear energy transfer (LET) is defined as the energy transferred to the absorbing medium per unit track length of the particle. LET is usually given in units of keV/μm. Therapeutic photons are regarded as low-LET particles, with an LET value of about 0.2 keV/μm, while 2.5 MeV α particles have an LET value of 166 keV/μm and are categorized as high-LET particles. A 150 MeV proton have an LET value of about 0.5, and are considered among the low-LET particles [17].

2.3.2 Relative Biological Effectiveness

There is a difference in what biological effect a certain dose provided by different particles will have. The Relative Biological Effectiveness (RBE) is given by the ratio of the dose of a reference radiation and the dose of the applied radiation to give equal biological effect. Historically 250 kV X-rays are regarded as the standard reference radiation which to normalize the effect other types of particles will have.

$$RBE = \frac{\text{Dose of 250 kV X rays}}{\text{Dose of test radiation}} \tag{2.6}$$

In clinical proton therapy an RBE value of 1.1 is used. This is mainly based on experiments with animals conducted in the early days of proton therapy.

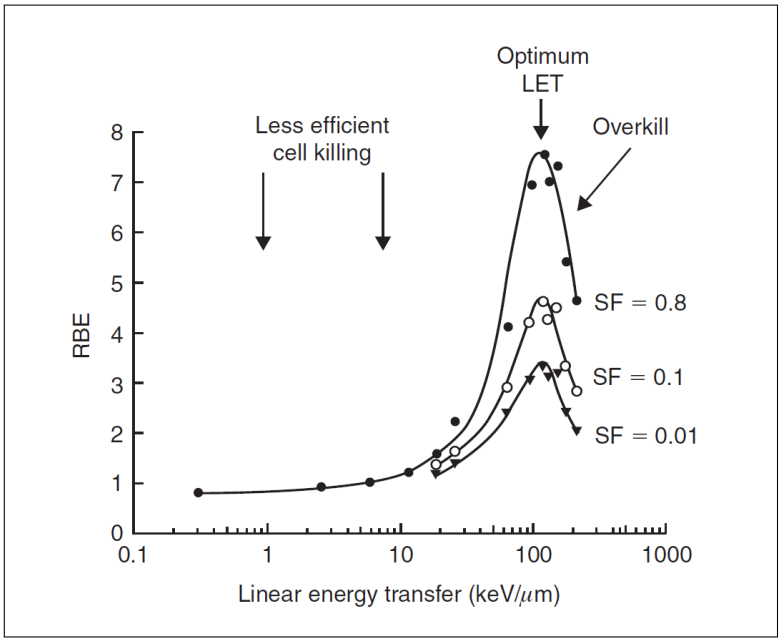

Figure 2.8: The dependence of Relative Biological Effectiveness (RBE) on linear energy transfer (LET). SF is an abbreviation of survival fraction [20].

The RBE is not a constant, rather it depends on various properties such as proton beam energy, depth in tissue and dose per fraction [15]. Studies have shown that the proton RBE can deviate from the value of 1.1, and that this generic value is more of an average value [18].

The RBE depends on the LET and increases with increasing LET until it reaches a maximum around 100 keV/μm, and declines above this value. To ensure that a cancer cell is killed, a sufficient amount of energy must be deposited in the cell in order to destroy the DNA molecule. Low-LET particles are sparsely ionizing and many particles are needed to kill a cell. Very high-LET particles with LET higher than 100 keV/μm are densely ionizing and deposit even more energy in the DNA than what is required in order to kill the cell [19]. This effect is illustrated in figure 2.8.

2.3.3 Dose

The term absorbed dose is defined as the amount of energy (Joule) absorbed per unit of mass (kg). The definition is that 1 Joule/kg corresponds to the S.I. unit of 1 Gray (Gy). The energy lost by the protons exceeds the energy absorbed by the medium. The reason for this discrepancy is that some of the protons lose energy by the production of neutral secondary particles, such as photons and neutrons, that can carry the energy away from their origin and deposit it elsewhere outside the volume of interest [15].

Since different types of radiation have different effects on matter, one needs to take into account various factors to predict the effect of a given radiation dose. In order to be able to compare the biological effectiveness of different types of radiation in tissue, the term equivalent dose has been established. The equivalent dose H_T is the product of the absorbed dose D_T and the radiation weighting factor W_R. The S.I. unit for equivalent dose is Sievert (Sv) [17]. Table 2.1 displays the weighting factors for different types of radiation.

$$H_T = \sum W_R D_T \tag{2.7}$$

Table 2.1: Quality factor W_R for different types of radiation [21].

Type of radiation	*Energy*	*Quality factor*
Photons, electrons	all energies	1
Neutrons	$<$ 10 keV	5
	10 - 100 keV	10
	100 keV - 2 MeV	20
	2 - 20 MeV	10
	$>$ 20 MeV	5
Protons	$<$ 20 MeV	5
Alfa particles, fission fragments, heavy nuclei		20

Different organs and tissue in the body have different sensitivities for radiation. To estimate the risk of damage caused by radiation in humans, the entity effective dose is more describing. In the term effective dose a tissue-specific weighting factor, W_T is added. The unit of effective dose is Sievert. Table 2.2 summarize tissue-specific weighting factors for organs.

The differences in radiation tolerance within the human body is something that has to be considered when making a treatment plan for a patient. Some

Table 2.2: Tissue-specific weighting factors W_T given by ICRP (International Comission on Radiation Protection).

Organ/tissue	W_T *ICRP (2007)*	W_T *ICRP (1991)*
Breast	0.12	0.05
Bone marrow	0.12	0.12
Colon	0.12	0.12
Lung	0.12	0.12
Remainder	0.12	0.05
Stomach	0.12	0.12
Gonads	0.08	0.20
Bladder	0.04	0.05
Liver	0.04	0.05
Oesophagus	0.04	0.05
Thyroid	0.04	0.05
Bone surfaces	0.01	0.01
Brain	0.01	-
Salivary glands	0.01	-
Skin	0.01	0.01

organs are considered "serial", such as the spinal cord. A damage to one part of the spinal cord can be fatal for the whole organ. In the clinical regime, serial organs have to be treated with special care to avoid over dosage. At the same time some organs are considered "parallel" such as liver or lung. Parallel organs can operate even if one part of it is damaged. Knowledge of the dose delivered to a critical organ, and the uncertainties that need to be considered, is important when making decisions about treatment.

Stopping Power

In particle therapy the term stopping power has its use. Stopping power is the rate at which a single proton loses kinetic energy:

$$S = -\frac{dE}{dx}\frac{MeV}{cm} \tag{2.8}$$

The mass stopping power is corrected for density:

$$\frac{S}{\rho} = -\frac{1}{\rho}\frac{dE}{dx}\frac{MeV}{g/cm^2} \tag{2.9}$$

The physical absorbed dose is related to the mass stopping power and the fluence:

$$D = \Phi \frac{S}{\rho} \tag{2.10}$$

The dose rate is given by the relation:

$$\dot{D} = \frac{i_p}{A} \frac{S}{\rho} \frac{Gy}{s} \tag{2.11}$$

where i_p/A is the proton current density in nA/cm^2. A high dose rate is a goal for the development of treatment techniques. Reducing the overall treatment time reduces the uncertainties related to patient movement [15].

Chapter 3

Radiation Therapy

About half of all cancer patients receive radiation therapy [2]. Radiation treatment can be given in combination with chemotherapy or surgery, or both. Treatment techniques have evolved radically during the last decades, alongside the increased availability and quality in medical imaging and computing power.

3.1 Medical Imaging

Medical imaging has been one of the key factors enabling precise treatment in many fields within medical science. Efforts have been successfully made to reduce noise, increase resolution, reduce imaging time and also to reduce exposure to ionizing radiation.

3.1.1 Computed Tomography (CT)

Within diagnostic imaging prior to radiation therapy, Computed Tomography (CT) is the imaging modality most commonly used. In short, a CT scanner consists of a rotating X-ray tube that produces bremsstrahlung, and an array of detectors that can detect and read out the signals. With the use of X-rays, a 3D image of the body is created, slice by slice. Figure 3.1 illustrates the principle of CT. A CT examination maps the various attenuation coefficients throughout the body. The attenuation of a photon beam in a given tissue is presented in a scale which is normalized with respect to the attenuation of photons in water, and this is displayed in a normalized (grey) scale, this scale is the Hounsfield Unit (HU) scale, and the HU is defined as;

$$HU = 1000 \times \frac{\mu_{tissue} - \mu_{water}}{\mu_{water}} \tag{3.1}$$

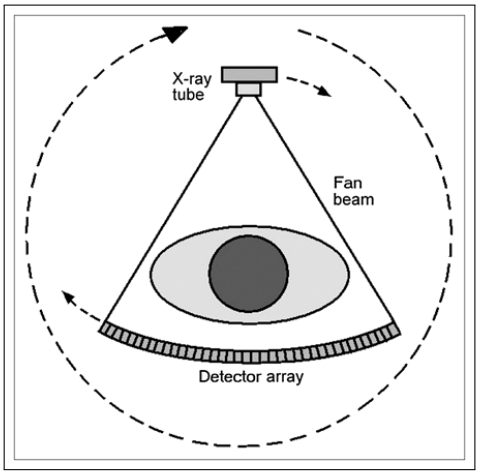

Figure 3.1: The principles for Computed Tomography. An X-ray tube revolves around the patient, and a detector array detects the attenuated X-rays on the other side of the patient. The signals from the detectors are read out and based on the information about the attenuation in the body, a map of body is made. This is repeated slice by slice through the patient [22].

The HU for water is set to 0, for air it is -1000 and for bone and denser materials it is +1000 and upwards. The HU range from -1000 to about +3000 in human body tissue. Metal implants can have a HU of up to around +5000.

Imaging with Computed Tomography (CT) is a well established image modality. Most hospitals are in possession of a CT scanner. A CT examination performed in one clinic should be possible to interpret in another clinic. CT is a versatile tool and it provides a detailed anatomical presentation of the body. In CT images there will be a sharp contrast between bone and tissue. A CT scan can be conducted during one breath hold cycle, if necessary or desired. When a patient has undergone a diagnostic CT scan, the images will be examined by radiologists and oncologists. Thereafter the CT image set is imported to a treatment planning software, and a plan for the radiation therapy prescription will be created. In the treatment planning software an oncologist will delineate the volume(s) to be treated and critical organs around the tumour and thereby creating the Clinical Target Volume(s) and Organs At Risk (OAR).

There are some limitations when using CT images, which displays tissue density, as the basis for tumour delineation. The exact locations of where healthy tissue ends and tumour tissue starts can be hard to identify based

on CT images without additional diagnostic information. The density of tumour tissue may be almost identical to that of nearby healthy tissue or of organs at risk close to the tumour. Further, the CT images can be noisy and contain artefacts, this is more frequent when a patient has a metal implant. For particle therapy these uncertainties can alter the dose calculation. The conversion from Hounsfield Units to proton stopping power can be a source of uncertainties. This topic is further addressed in section 3.5. Sharp density gradients can cause a problem since the CT images has a finite resolution and small objects and sharp gradients may be influenced by the partial volume effect. Since the photon depth dose profile does not possess the sharp distal dose gradient characteristic for charged particles, these uncertainties do not have the same impact in photon therapy as in particle therapy.

DICOM DICOM is a standard for handling, storing, printing and transmitting information in medical imaging. DICOM is an abbreviation from Digital Imaging and Communication in Medicine. Both CT-,MR- and PET-CT images are stored in DICOM format files and the information can be exchanged between two clinical treatment units or hospitals provided they all apply the DICOM standard.

3.1.2 Positron Emission Tomography (PET)

Positron Emission Tomography (PET) is an image modality where the photons detected in the scanner originate from the body, as a result of positron emission. The most common PET scan in oncology involves injection of the radioactive tracer fluorodeoxyglucose (^{18}F-FDG) into the bloodstream of the patient in order to obtain images displaying the uptake of this radiopharmaceutical in the patients body. The metabolic processes in the human cells use glucose as a source of energy. Since cell-division in tumours demand a lot of energy, they will take up ^{18}F-FDG. The ^{18}F is a radioactive isotope with a half-life of around 110 minutes. ^{18}F decays to ^{18}O via positron emission. As the positron annihilates with an electron, two gamma photons will be emitted back-to-back and these will be detected by the PET camera based upon coincidence criteria. Most PET scanners in use on hospitals has a combined PET-CT scanner system where the PET image is fused into the CT image in order to obtain PET and CT information in the same images.

PET can also be useful for tracing the deposited dose in particle therapy. As mentioned in chapter 2, there will be production of radioisotopes such as ^{11}C, ^{13}N and ^{15}O in a patient's body during particle therapy. This will lead to positron emission in the tissue traversed, and this positron emission can

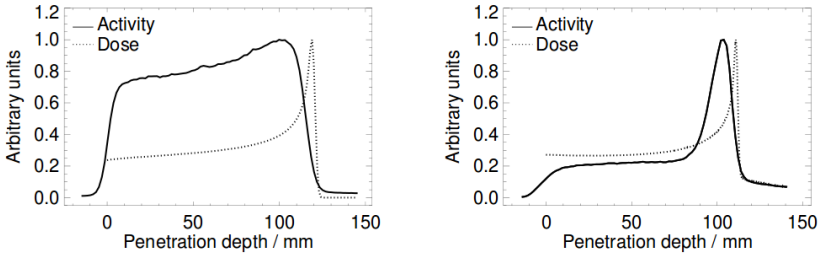

Figure 3.2: An example of application of a PET signal as a measure of dose deposition; Measured positron activity (solid line) and dose (dashed line) as result of protons (left) and ^{12}C ions (right) hitting a PMMA target. For the ^{12}C ions there is a peak activation shortly before the Bragg peak (right image), while for proton beam activation, the activation is a result of target fragmentation along the beam path (left image). From Parodi, PhD thesis [23].

be mapped with a PET camera. Dose imaging by this method must be carried out either during the treatment, or within some minutes after treatment. By using this method, the actual dose distribution in the patient can be deduced, and this can be compared with the predicted dose from the treatment plan. The unavoidable activation of the patient can thus be utilized without invasion or additional dose to the patient as a measure of dose deposition in the patient's body.

In figure 3.2 the β^+ activation for proton beams and ^{12}C ion beams are shown. Protons can only produce positron emission from target nuclei in the media traversed. The isotopes (such as ^{11}C, ^{15}O and ^{13}N) are formed along the beam path, until a few millimeters in front of the Bragg peak. For heavier ions, such as ^{12}C, positron-emitting projectile fragments are also produced. This activation will happen shortly before the dose Bragg peak [15] [23].

3.2 The Therapeutic Ratio

The term "the therapeutic ratio" is referred to as an outcome assessment of the treatment in radiation therapy. The therapeutic ratio is the ratio of the probability for tumour eradication and normal tissue complication and these entities are modelled and represented in so-called dose-response curves. The efforts made to improve delivery techniques and treatment modalities focus mostly on improving the therapeutic ratio and hence broaden the "therapeu-

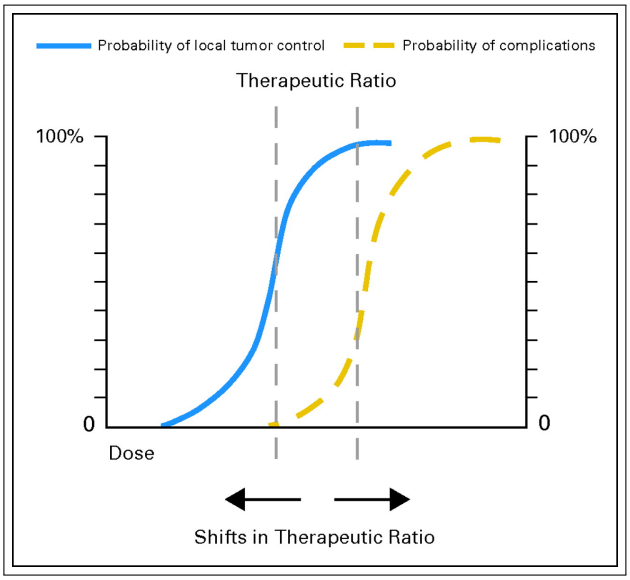

Figure 3.3: Sigmoid dose-response curves. The therapeutic ratio is the ratio between the probability for local tumour control and normal tissue complication [24].

tic window" [15]. The dose-response curve has a sigmoid shape, as illustrated in figure 3.3.

3.3 Fractionation

A radiation treatment course is split into fractions. The reason for this is that the healthy tissue needs some time to repair after being irradiated. The tumour cells can also repair their damage, but their ability is inferior compared to healthy cells, and as the treatment course continues, the cancer cells are gradually inactivated and thus put out of reproductive action. A typical treatment course can for instance consist of delivery of a prescribed dose of 50 Gy delivered in 25 fractions of 2 Gy each. The total dose and fractionation scheme depends on the diagnosis and whether the treatment is curative or palliative.

The fractionation scheme applied in proton therapy differs little from the fractionation scheme applied for a corresponding treatment with photons. A proton beam will have a $\sim$10 % higher biological effectiveness compared to photons, this enhanced RBE has not yet motivated a very different fractiona-

tion regime for proton therapy compared to photon therapy. For heavier ions such as ^{12}C-ions, the RBE will be higher (ranging from 2 to 3) and thus a more effective tumour eradication is invoked. Hence, the prescribed dose can be delivered in fewer fractions. At the ^{12}C-ion treatment facility HIMAC, operated by the Japanese National Institute for Radiological Science, NIRS in Chiba, Japan, patients have been treated with as few as one fraction [25].

3.4 Radiation Therapy with Photons

Radiation therapy with photons are considered the standard radiation treatment of cancer worldwide. The field has undergone a tremendous development since the early days of radiation therapy, more than a hundred years ago. Medical linear accelerators are being used to provide photon beams with energies ranging from a few MV to about 20 MV.

3.4.1 The Medical Linear Accelerator

The medical linear accelerator (linac) uses high-frequency electromagnetic waves to accelerate electrons towards a target. The electromagnetic wave can be travelling or stationary, depending on the design. When the electrons strike the target, usually made of a high-Z material, such as tungsten, bremsstrahlung X-rays will be produced. It is also possible to remove the target and utilize the energetic electrons in treatment of superficial lesions. The energy of the X-rays are spectrum distributed with the maximum energy equal to the acceleration gap electron energy, given in units of MV (mega volts). The radiation field will be shaped for the treatment fields to cover the tumour volume with some margins. The field shaping is done in the treatment head with collimators, scatter foils and filters. Figure 3.4 shows a schematic view of the treatment head of a typical medical linac.

3.4.2 Treatment Techniques

Various treatment techniques have been developed alongside the development of better imaging equipment and also with vastly improved computing power. When a more accurate and detailed patient anatomy is available for the oncologists, this enhances the possibilities for them to improve the target definitions and for them to delineate the target volumes more precisely. This induces in turn the possibility and a need for a more targeted treatment and treatment delivery. Based on the geometry provided by 3D CT images, a dose plan is created, in which all the details about the treatment, such

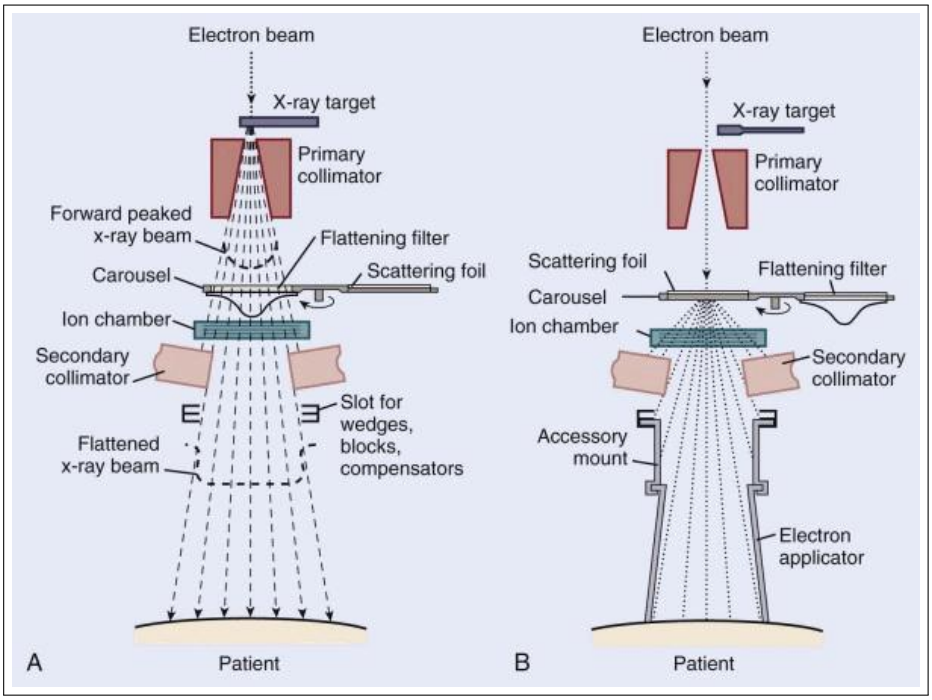

Figure 3.4: The major components in a typical linear accelerator treatment head. In image A: photon therapy mode. The first collimation is done by the fixed primary collimator. The beam passes through a flattening filter in order to create a homogeneous field of photons. The dose rate and field symmetry are monitored in the dose monitoring chambers located above the adjustable secondary collimators. In image B: electron therapy mode [11].

as treatment dose, dose distribution, treatment machine, treatment energy, beam angles, collimator angles, patient position etc, are described.

In order to reduce the uncertainties during radiation treatment as much as possible, patient immobilization is a fundamental factor to be dealt with. The immobilization revolves around how to fixate the patient to the treatment position with masks and other equipment tight enough for helping the patient to remain fixated but comfortable enough for the patient to lay still during irradiation. Frequently used are; headmasks, upper body masks, special fixation mattresses, knee fixation pillows and bite blocks moulded to fit the patient's jaw. The tumour can move inside the body, this is especially important to handle for cases with tumours in the thorax or abdomen. To take into account these unavoidable and involuntary movements, the target volume needs a margin, thus the clinical target volume must have margins so that the irradiation will cover the tumour at all times during the treatment, these margins added to the clinical target volume produces a larger volume covering the clinical target volume, the planning target volume. In order to spare healthy tissue, one wishes and tries to reduce these margins as much as possible. A robust treatment plan is characterized by the ability to maintain a satisfactory dose coverage of the target volume, despite changes in the geometry.

3D Conformal Radiation Therapy

With the 3D anatomic information from a planning CT scan, the tumour will be delineated in all dimensions. With 3D conformal radiation therapy, the beams will be shaped and designed to fit the target shape and position. To cover the target volume and at the same time spare surrounding tissue, the number of beams, the beam angles, the beam intensity and beam shape will be determined using a treatment planning program. Hardware such as collimators are used to obtain the desired beam shape and properties.

Intensity Modulated Radiation Therapy (IMRT)

Intensity Modulated Radiation Therapy utilizes the initial non-uniform beam if the treatment machine is Flattening Filter Free (FFF) as recent linacs now can bee, otherwise the IMRT will be delivered from the flattened radiation fields. The target volume is irradiated from multiple directions around the patient. The intensity and shape of the beam is adjusted step-by-step to fit to the target shape. IMRT relies on advanced computer algorithms. The user will set a list of criteria, such as desired dose to the target volume, max dose

to the surrounding tissue and organs at risk, and also a relative priority, by weights, for each of these criteria. The treatment planning program will then optimize the radiation intensity with a set of (user specified) beam directions to meet these criteria, thus this technique is called inverse planning. Especially for tumours with a challenging shape, IMRT will in general be able to provide a better tumour dose coverage than conformal techniques, while at the same time keep the dose to surrounding tissue low [26].

Volumetric-Modulated Arc Therapy (VMAT)

With Volumetric-modulated Arc Therapy, VMAT, the concept from IMRT and using multiple beam directions is further utilized. With VMAT the gantry delivers photon radiation continuously while rotating around the patient. The beam is continuously modified by both multileaf collimators and gantry movement to cover the target volume structure, and to spare healthy tissue [27].

3.5 Particle Therapy

Particle therapy is also referred to as hadron therapy or ion therapy; regardless of the name, it all refer to use of charged nuclear particles in radiation therapy. The particles used are protons (hydrogen ions), helium ions, lithium ions, oxygen ions, neon ions and carbon ions, of which protons are the far most common particle used followed by carbon ions as of 2013. When applying charged nuclear particles, given their characteristic depth dose distribution one enables delivery of higher doses to the tumour while maintaining the total dose to surrounding structures, and even reducing the total dose to these structures. By deposition of the nuclear particle's Bragg Peak in the target volume area, the maximum dose deposition will be in the tumour itself and hence the therapeutic ratio will increase, and thus this will potentially increase local control, decrease occurrence of side-effects and improve quality of life of the patient [15]. In figure 3.5 a cubic volume of water, placed inside a larger water phantom is treated with a) protons and b) photons, both with one treatment field. A clinical case is shown in figure 3.6, where a patient geometry is subject to a proton treatment plan and a photon treatment plan. The patient is a child with medulloblastoma cancer, a condition for which a part of the treatment includes irradiation of the entire spinal cord axis. One can see that in the photon plan, the whole upper body gets unwanted and unavoidable dose. This includes critical organs such as the heart, lungs, intestines and the oesophagus. In figure 3.7 the photon and proton depth

dose profiles in water are plotted together. The photon beam will have its dose maximum a couple of cm into the water volume, and then the dose deposition decreases with depth.

To estimate the stopping power in a patient is a key point when making decisions about treatment. This issue will be addressed further in section 3.6.

The range of the proton depends on the energy of the proton beam. Figure 3.8 shows the range in water as a function of initial energy. In proton therapy the energies for therapeutic use is roughly 50 MeV - 250 MeV. The theoretical range in units of g/cm^2 in a homogeneous material is given by equation 3.2.

$$R\left(E_{initial}\right) = \int_{E_{initial}}^{E_{final}} \left(\frac{1}{\rho}\frac{dE}{dx}\right)^{-1} dE = \int_{E_{final}}^{E_{initial}} \frac{dE}{S/\rho} \tag{3.2}$$

This relation between range and energy can be fitted to a simple equation, the Bragg-Kleeman rule. The range of a proton beam is defined to be the position in depth of the distal 80 % (d_{80}) dose level of the Bragg peak [15].

$$R = \alpha E^{p_0} \tag{3.3}$$

Where $\alpha = 0.0022\ cm/MeV$ and $p_0 = 1.77$.

If a beam of protons with the exact same initial energy enters a material, they will not stop at the exact same depth. This is due to the statistical nature of the interactions each proton undergo. This leads to what is known as range straggling. The range straggling is about σ_{RS}= 1.2 % of the range for light materials. A realistic proton beam will have a small energy spread σ_{beam} [15]. Straggling makes the Bragg peak broaden. The width between the position in depth of the distal 80 % dose level, d_{80}, and the position in depth of the distal 20 % dose level, d_{20}, of the Bragg peak will depend on these two properties:

$$d_{20} - d_{80} = 1.3 \times \sqrt{\sigma_{RS}^2 + \sigma_{beam}^2} \tag{3.4}$$

The transversal distribution of a proton beam is nearly Gaussian. This smearing out of the distribution of beam particles is a result of multiple Coulomb scattering, many tiny angular deflections. The multiple Coulomb scattering occurring in the patient sets the lower limit for the resolution of the treatment.

The lateral penumbra of a proton beam limits the accuracy, or the resolution, of the treatment. This effect is less pronounced when applying heavier charged particles such as helium, and the effect is even smaller for carbon ions, as illustrated by figure 3.9.

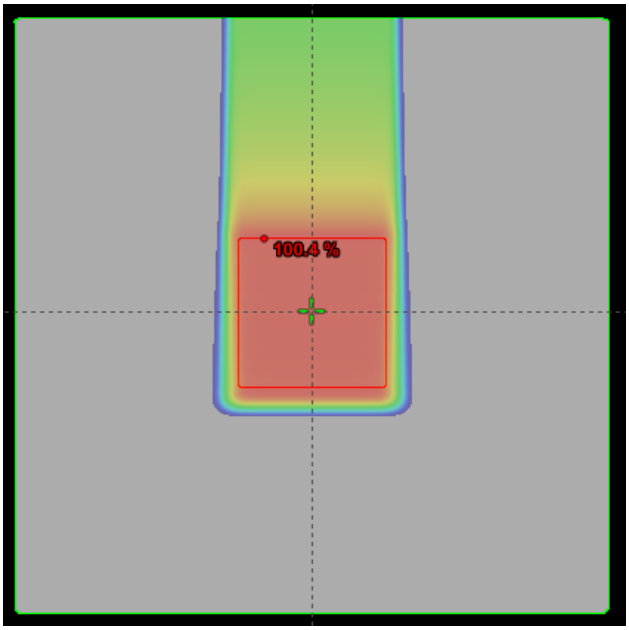

(a) The target volume irradiated with protons.

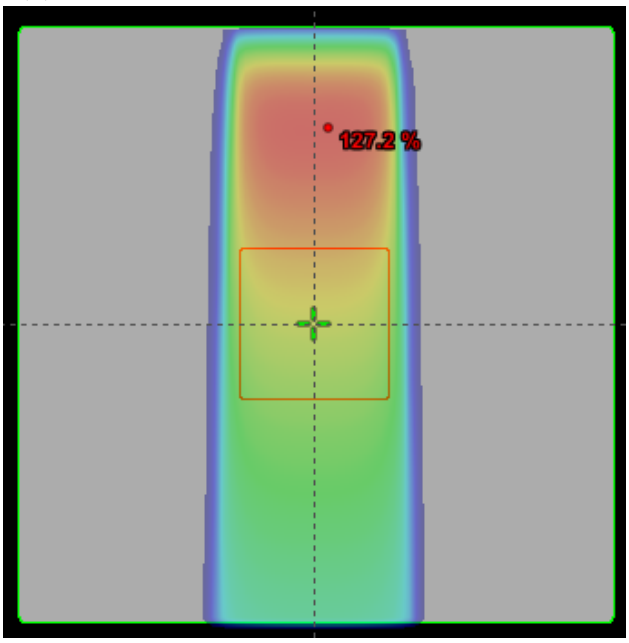

(b) The target volume irradiated with photons.

Figure 3.5: The calculated dose to a volume irradiated with a) protons and b) photons, both with one treatment beam. One can see that the photons has a dose maximum located a couple of cm into the phantom. The target volume is $5 \times 5 \times 5$ cm^3 and is located in the center of a water phantom. The software used for this calculation is Varian Eclipse Proton Planning.

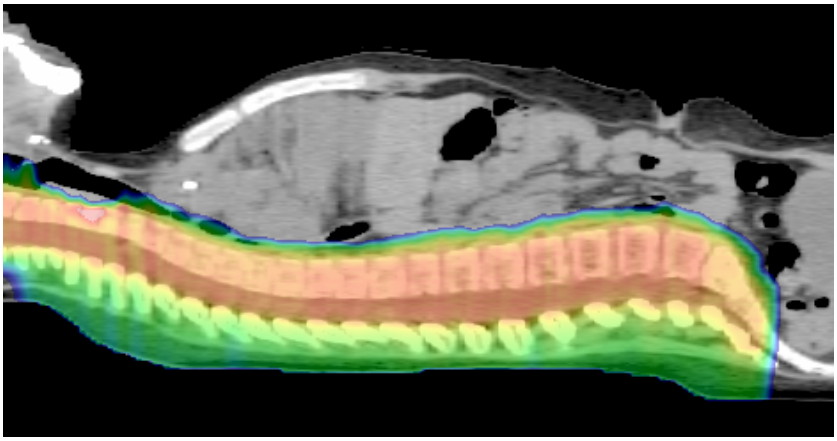

(a) The target volume irradiated with protons.

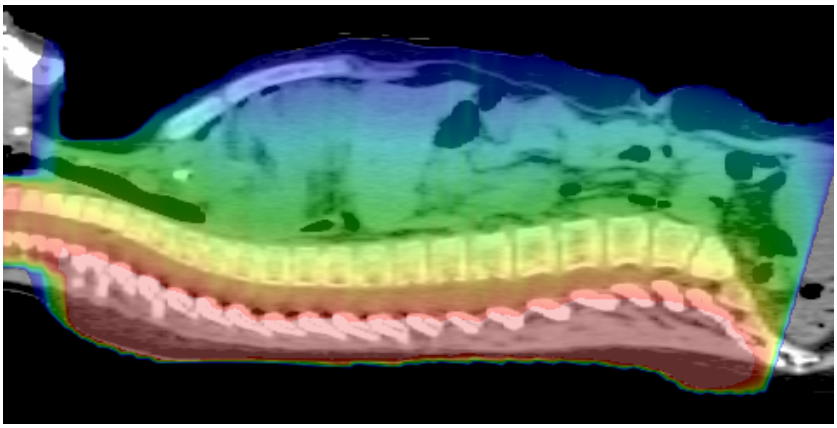

(b) The target volume irradiated with photons.

Figure 3.6: Treatment plans made with a) proton therapy and b) photon therapy, both plans are calculated with Varian Eclipse software. The patient is a child with medulloblastoma, a condition that occurs more often for children than for adults. Part of the treatment involves irradiation of the entire spinal axis. These treatment plans are part of ongoing doctoral work [28].

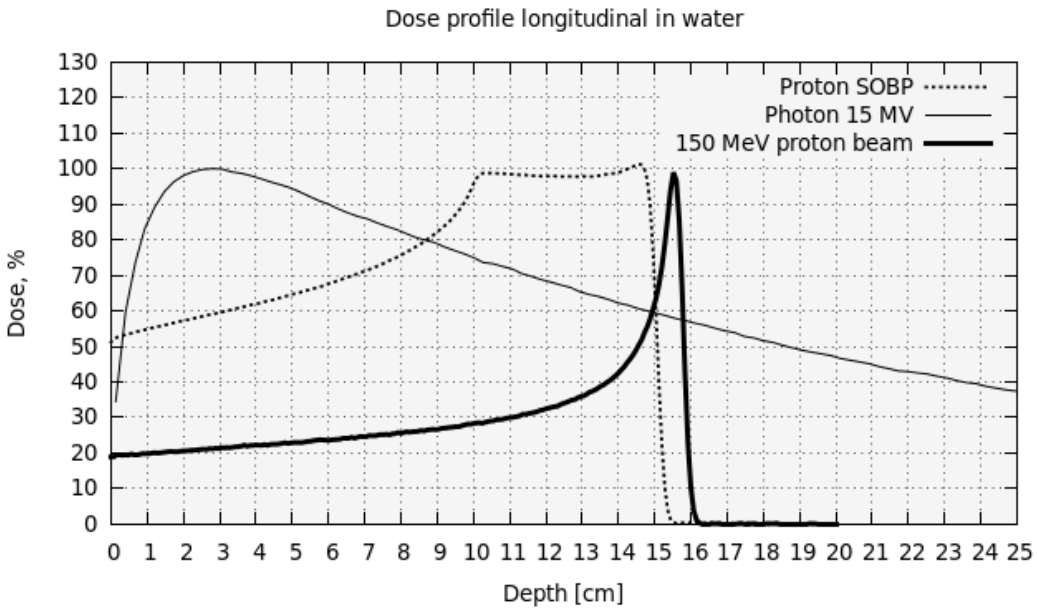

Figure 3.7: FLUKA Monte Carlo simulations. Depth dose profile plotted for 15 MV photons, 150 MeV protons and a spread-out Bragg peak with proton beam energies from 116 MeV to 146 MeV in water. Photon beam data used with permission from [29].

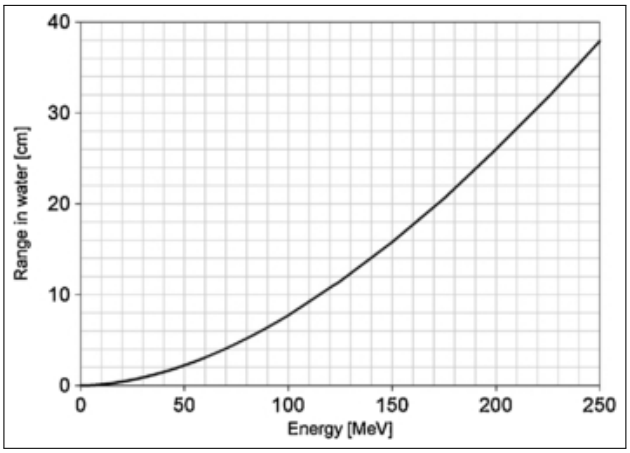

Figure 3.8: The proton range in water as a function of initial energy [15].

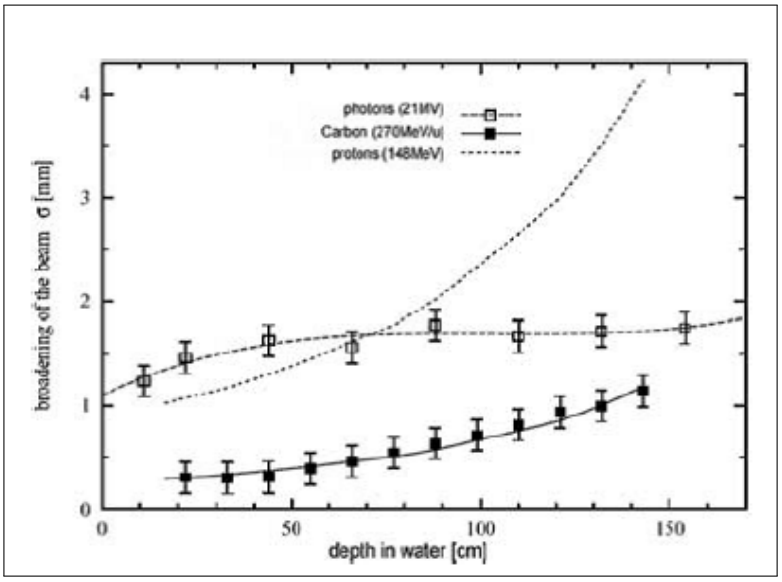

Figure 3.9: The lateral penumbra of photons, protons and carbon ions in water [30].

3.5.1 Particle Accelerators

In order to deliver particles with the sufficient energy for therapeutic use, a particle accelerator is needed. During the first decades after the introduction of particle therapy, patient treatment were conducted at nuclear physics laboratories equipped with a particle accelerator, usually a cyclotron or a synchrocyclotron. Once the treatment with protons had proved to be feasible, dedicated treatment facilities started to emerge. For a proton treatment unit to fit within limited spacing such as hospitals and clinics, especially in urban cites, efforts are being made to develop compact accelerator systems. Still the particle sources are quite space consuming, not only the accelerator itself, but also the radiation shielding (walls) and beam line hardware (magnets) [15].

There are two main accelerator types in use today: cyclotrons and synchrotrons.

Cyclotron

In a cyclotron there is an ion source located in the centre. The ions are pulled out of the ion source, and pushed into a vacuum chamber. The particles are accelerated by a radio frequency (RF) system and their trajectories are bent

and confined by a strong magnetic field. The ions will follow a spiral shaped orbit, allowing repeated acceleration by the RF-voltage. As their velocity increases, their radius increases until the desired energy is reached and an extraction system will maneuver the ions out of the cyclotron and into the beamline [15]. The electrical nodes giving rise to the electric field in the accelerating gap are historically called "dees" for their resemblance to the letter, as can be seen in figure 3.10 [31].

The Lorentz force acts as the centripetal force, giving us the relation:

$$Bqv = \frac{mv^2}{r} \tag{3.5}$$

$$Bq = \frac{p}{r} \tag{3.6}$$

$$v = \frac{2\pi r}{T} \tag{3.7}$$

$$T = \frac{2\pi m}{qB} \tag{3.8}$$

The radio-frequency of the accelerating system is synchronized to the path of the particle, and it is given by the cyclotron equation:

$$\omega = \frac{qB}{m} \tag{3.9}$$

Synchrocyclotrons will adjust their RF frequency to compensate for the relativistic change in the particle mass as their velocity increase. The Lorentz factor γ increase with v:

$$\gamma = \frac{1}{\sqrt{1 - \frac{v^2}{c^2}}} = \frac{1}{\sqrt{1 - \beta^2}} \tag{3.10}$$

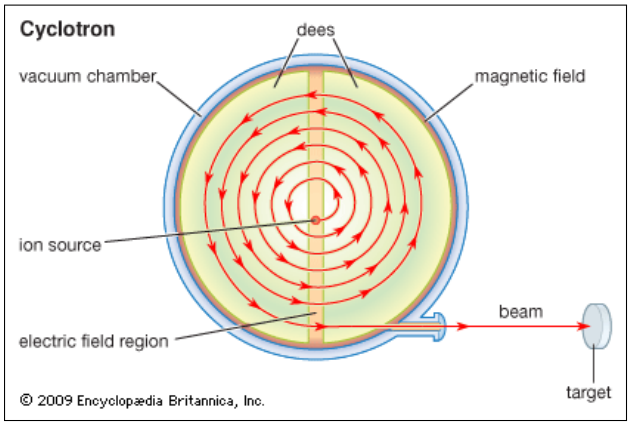

Figure 3.10: Schematic drawing of a cyclotron.

The particle beam from an isochronous cyclotron will have a continuous character while the particle beam from a synchrocyclotron will have a pulsed character. For both types the intensity is easily adjusted to almost any desired intensity within the accelerator specifications. The beam energy is fixed at the maximum energy of the accelerator. The cyclotrons used in proton therapy have a diameter of 3.5 - 5 m depending whether or not they are equipped with superconducting magnets.

Currently cyclotrons are only in use for proton therapy, not for heavier particles such as carbon ions.

Synchrotron

In a synchrotron the radius is fixed while the magnetic field is adjusted as the particles are being accelerated. The particles need some initial kinetic energy before they enter the synchrotron ring. This is typically provided by a linear accelerator, providing the particles with an energy of 3 to 7 MeV. For each time the particles have been pushed forward by the accelerating RF cavity, the magnetic field provided by the focusing and bending magnets along the ring must increase. Figure 3.11 shows a simple schematic drawing of a synchrotron. Figure 3.12 is a photograph displaying the synchrotron at CNAO in Pavia, Italy. At CNAO patients are treated both with protons and carbon ions [32].

The protons are accelerated to the desired energy between 70 and 250 MeV, and then extracted. In this way, the beam energy can be modulated during operation. The beam does not have the continuous nature of the

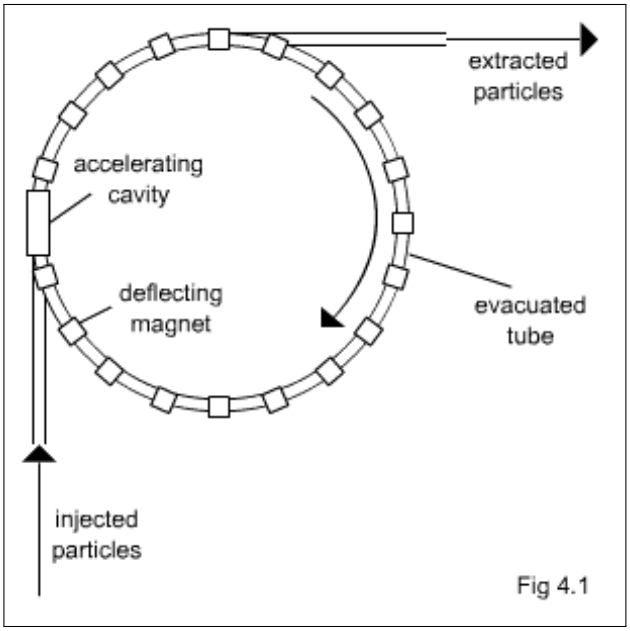

Figure 3.11: Schematic drawing of a synchrotron [31].

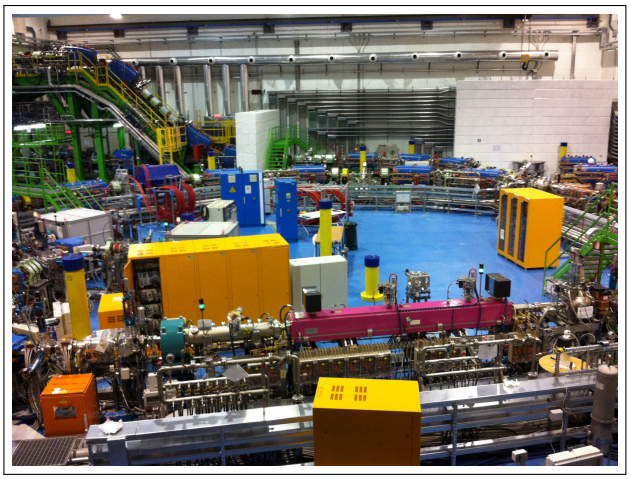

Figure 3.12: The synchrotron at the hadron therapy facility CNAO in Pavia, Italy. At CNAO the synchrotron accelerates both protons and carbon ions. Photograph by the author, March 2013.

isochronus cyclotron beam. The particles come in pulsed "spills", and the energy can be adjusted between the spills.

For heavy ion therapy, synchrotrons are currently the only option for particle acceleration. The diameter of synchrotrons in therapeutic use are 6 - 25 meters, depending on the type of particle produced. The energies applied in heavy ion therapy range up to about 400 MeV pr nucleon, which corresponds to a range of 25 cm i water [31].

3.5.2 Energy Modulation - Creating a Spread Out Bragg Peak

The proton beam from an accelerator will be almost monoenergetic and exhibit a narrow Bragg peak. To cover the target volume in its full depth, the beam energy has to be adjusted in order to create a so-called spread-out Bragg peak (SOBP). Beams of different ranges are added either by altering the initial energy from the accelerator, either by adding material in the beam line, or by directly adjusting the beam energy in the accelerator (only possible with synchrotrons).

To produce an SOBP with a flat dose plateau at the desired depth and with a given thickness, each energy interval needs to be weighted relative to the other intervals. The highest energy, which constitutes the distal edge of the SOBP, is attributed the highest weight. In figure 3.13 two plots are shown. In figure 3.13 a) 21 beam energies are plotted in the same diagram, unweighted. In figure 3.13 b) all the beams are weighted in order to obtain an SOBP when the beams are added.

Range Modulator Wheel Many facilities use a range modulator wheel (figure 3.14) to create the correct spread in energy. There are many designs available, but the basic idea is the same. The radius of the wheel is constant, while the thickness is distributed in a steplike fashion, where the area of each step reflects the weight of the corresponding energy, or range.

Ridge Filter The principle behind the ridge filter (figure 3.15) is the same as for the range modulator wheel mentioned above. However, the ridge filter is a static component positioned in the beamline. The beam is spread to a monoenergetic, homogeneous field of protons before entering the ridge filter. The shape of each of the ridges determines the shape of the SOBP. Ridge filters are commonly used in carbon therapy facilities, but are also used for protons.

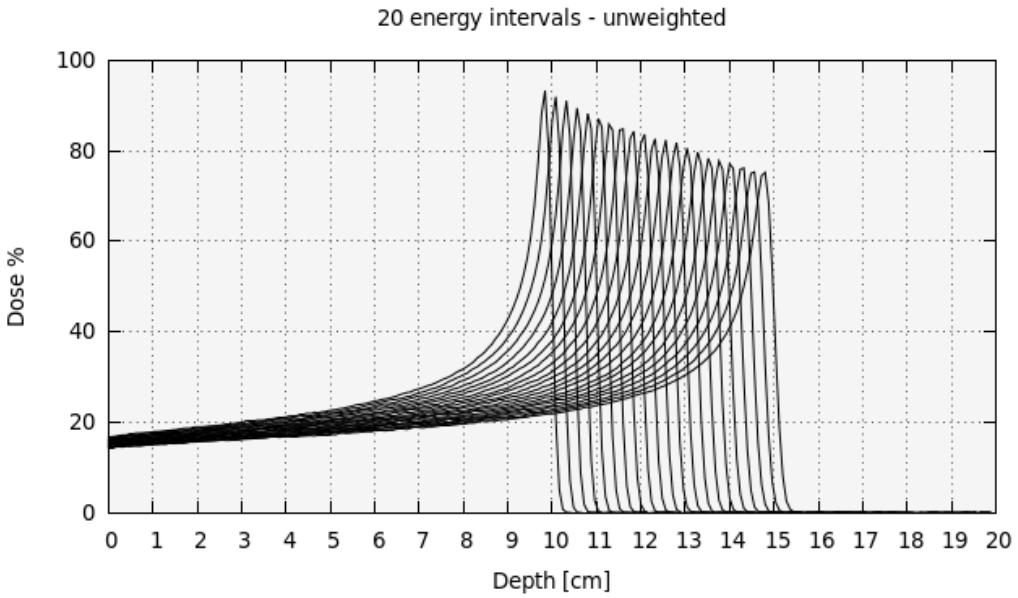

(a) The longitudinal depth dose profile from the 21 beams with energies ranging from about 116 MeV to 146 MeV. In this plot all beams have the same weight.

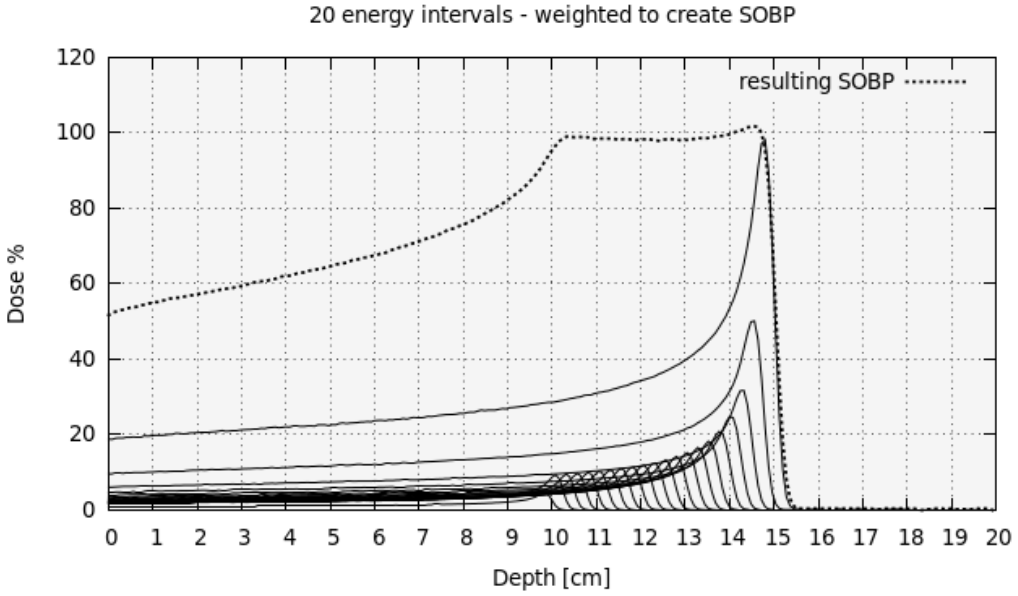

(b) The longitudinal depth dose 21 beams are weighted and added to create an SOBP.

Figure 3.13: FLUKA Monte Carlo simulations. The principle behind the spread-out Bragg peak. Beams of different energies are added in a certain way to obtain a flat dose plateau at the desired depth.

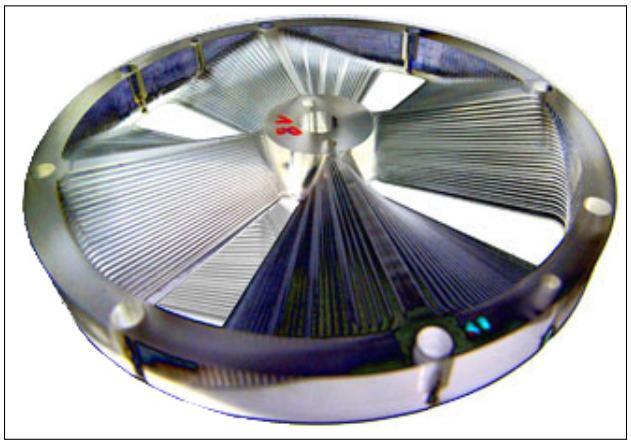

Figure 3.14: Photograph of a typical range modulator wheel. The wheel will rotate in the beamline, making the beam traverse different thickness of material at each step in the wheel [33].

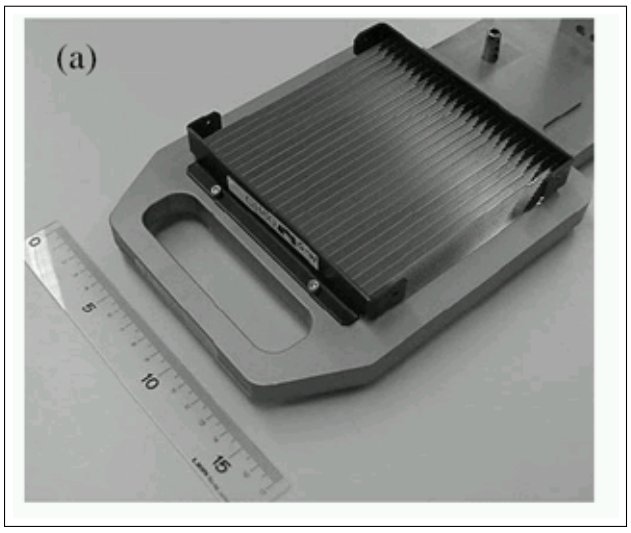

Figure 3.15: Photograph of a ridge filter. The beam is spread twice before entering the ridge filter. The height and width of the ridges determines the shape of the SOBP. An additional range shifter can be used to position the SOBP at the desired depth [15].

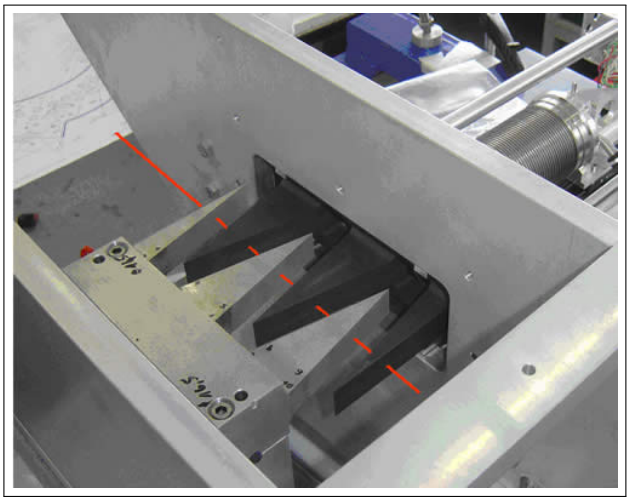

Figure 3.16: Photograph of a range shifter wedge. The wedges are programmed to be positioned in the beam to create the desired dose profile [34].

Lamination A slightly more sophisticated way of modulating the range of the beam is by the method called lamination. Instead of applying prefabricated hardware, designed for each thickness or shape, the range modulation can be achieved by placing material in the beam in a programmed way. Thin layers of lead and plastic, wedges (figure 3.16) or an adjustable water column can be controlled by a computer to apply a certain thickness in the beam.

Choice of Material in Energy Modulators The materials used in energy modulation has to be carefully chosen. Once the beam enters a range modulator, further scattering of the beam is not desired. Hence, a low-Z material such as aluminium, carbon or even plastic is usually applied in range shifter wheels and ridge filters. The lateral spread of the beam cam be accomplished by the use of scatter foils in the beam line. For scatter foils a combination of high-Z (such as lead) and low-Z materials are usually applied.

Proton Nozzle A schematic layout of how a proton treatment head, a proton nozzle, can be constructed is shown in figure 3.17.

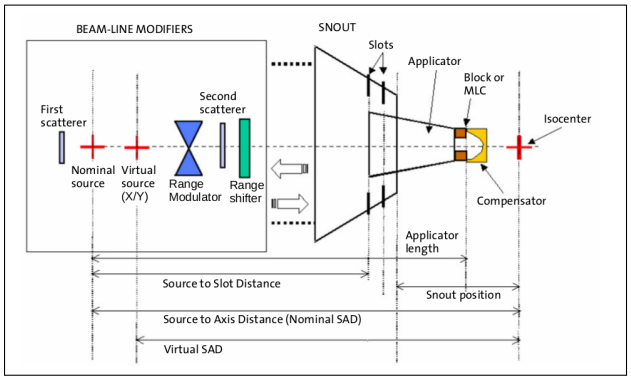

Figure 3.17: Schematic layout of a proton nozzle, from Varian's Eclipse Proton Planning reference guide [35].

3.5.3 Treatment Techniques

The treatment techniques used in proton therapy can be split into two main categories: the scattering technique and the scanning technique. The basic principles are illustrated in figure 3.18.

Scattering The scattering technique was the first technique used to modulate the proton beam to achieve the desired coverage of the treatment volume. It was developed during the 1960's and it is still a widespread technique. In a scattered beam system, the narrow beam from the accelerator is scattered to a larger area, to become a field, with a uniform intensity. To create a spread-out Bragg peak that covers the depth of the target volume, a range shifter wheel or ridge filter is used. To fit the structure of the treatment volume, a collimator, usually made of brass, is used to shape the field, while a compensator, usually made of plexi glas, is placed in the beam to make the maximum range of the protons follow the distal end of the tumour. The collimator and the compensator are field-specific and has to be produced for each patient (each tumour and each field).

Scanning The scanning technique is an active way of covering the target volume. By utilizing the narrow pencil beam obtained in the accelerator, varying magnetic fields will bend the beam and close to the patient steering magnets will enable a precise lateral scan through the each energy layer of the target volume. To distribute the dose deposition in order to cover the target volume in the longitudinal direction, in depth, the energy of the beam is modulated. The energy can be modulated using a range modulator such as

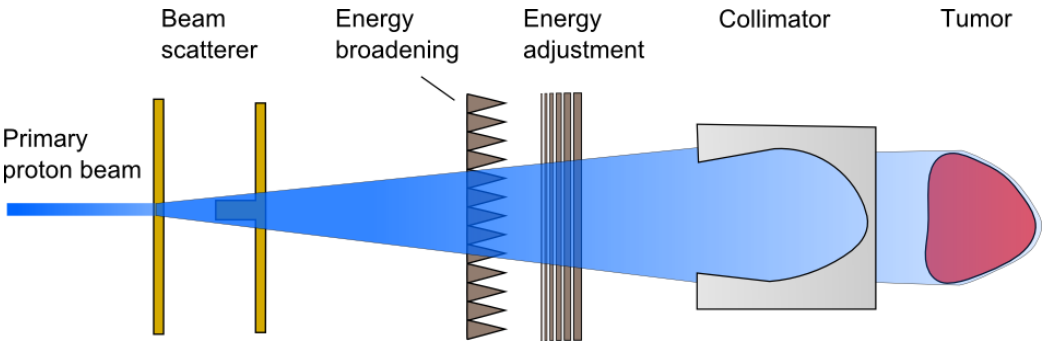

(a) The scattering technique beam delivery.

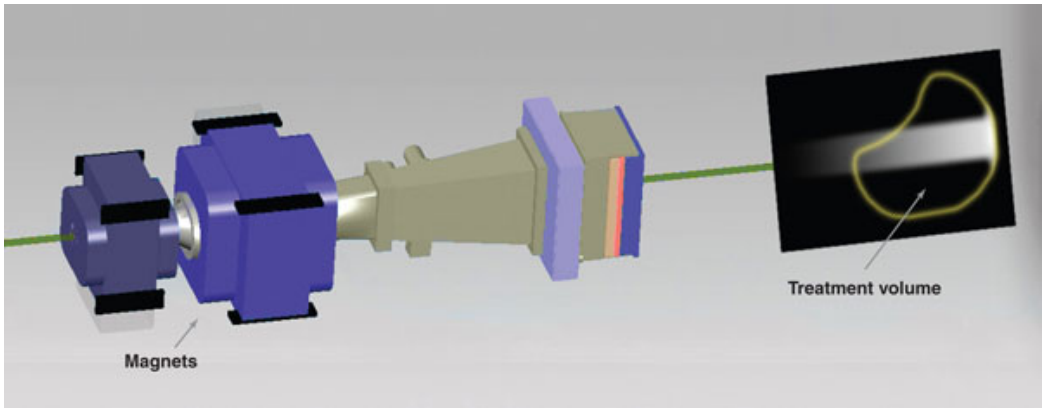

(b) The scanning technique beam delivery.

Figure 3.18: The principles behind the two main categories of treatment techniques, a) scattering [29] and b) scanning, [36].

a lamination system. Or if the accelerator is a synchrotron, the energy from the accelerator can be adjusted.

The scanning technique is a relatively new treatment method and it is developing rapidly as more and more clinics start using it. It has many advantages over the scattering technique. With the scattering technique there is extensive use of hardware such as collimators and compensator that has to be uniquely designed and manufactured for each patient and even each field direction. The generation of secondary particles such as neutrons is also reduced when using the active scanning approach. With a scanned beam there are multiple degrees of freedom and based on the experience from dose calculation and dose planning with photons, advanced techniques such as IMPT has emerged.

Uniform Scanning The uniform scanning technique uses a fixed scanned beam, and field shaping devices to cover the target volume. Constant beam intensities that are adjusted relative to the others are used to produce a flat dose plateau along the beam direction. As with the scattering technique, beam collimators and range compensators are used to fit the dose to the tumour. The production of secondary particles in the beam shaping aperture is still less than what is the case for scattered beams. This is due to the fact that for uniform scanning beams, the lateral width of the beam is adjusted to fit the collimators. The overall dose distribution in uniform scanning is more or less the same as for the scattering technique [15] (p. 108).

Single-field Uniform Dose (SFUD) With the SFUD technique the beam intensities and scanning pattern is customized for the field. The dose distribution for each field is uniform over the treatment volume [15] (p. 108). To make a more robust treatment plan, one can apply the SFUD technique on multiple fields, yet the fields are independent of each other.

Multifield Uniform dose (MFUD) Multifield uniform dose, or Intensity Modulated Proton Therapy (IMPT) is an active scanning technique analogous to intensity modulated radiation therapy (IMRT). With this technique the uniform dose coverage of the treatment volume is obtained as the resulting dose from two or more fields. With both MFUD and SFUD the SOBP is no longer the same concept as for uniform scanning or scattering. The treatment plan will assign an array of Bragg peaks, each calculated to hit one spot in the target volume. This way the volume will be irradiated spot by spot, layer by layer.

3.6 Range Uncertainties

As in photon therapy there are a number of uncertainties in proton therapy that one needs to be aware of. Setup errors, patient motion, physiological changes and stopping power estimation errors are all factors that can alter the precision of the treatment. Uncertainties in the proton range related to tissue heterogeneities and the estimated stopping power in the patient must be considered in order to deliver clinically adequate proton therapy. A common property used in proton therapy is the water equivalent path length (WEPL). The proton range depends heavily on the conditions leading to the WEPL along the beam path. If the material contents in the planned beam path changes during treatment, and thus the WEPL changes by a certain amount, the distal dose falloff will change correspondingly. This can lead to unwanted under dosage of the target volume and over dosage to the surrounding tissue, both compromising the quality of the treatment. Due to the depth dose characteristics of photons, a similar change in WEPL will not have the same impact on the delivered dose with photon therapy [15] [14].

Predicting the proton beam behaviour in a homogeneous water phantom of is straightforward. However, predicting the proton behaviour in a dynamic human body can be challenging. Inhomogeneities such as bone of varying size and density, gas or even medical implants can have large effects on the proton range. In addition there can be movement related to the respiratory cycle, heartbeats, digestion and other voluntary or involuntary movements.

From Hounsfield Units to Stopping Power Conversion The range of the proton beam, and thus the energy required to direct the Bragg peak at the target, is calculated based on the CT images. As mentioned above, CT Hounsfield Units are derived from the attenuation of X-rays. The proton stopping power depends on the physical density, elemental composition and mean ionization energy of the absorbing material. The CT HU numbers are converted to proton stopping power using a calibration curve. The method used to obtain this curve is called the stoichiometric method. Stoichiometry refers to the description of the quantitative relationship among substances in for instance a compound involved in a reaction. For a number of human tissues, the HU value is measured with X-ray CT, as well as calculated based on knowledge of the material. The theoretical proton stopping power is calculated based on the material's known elemental composition and the material properties, using a simplified version of the Bethe-Bloch equation [15]. The HU values are plotted against the relative proton stopping power, and a curve is fitted to this plot. The resulting fit is commonly a combination of three

linear fits; the first curve fits the lung data, the second fits the various organs and the last fits the bone tissues [37]. The stoichiometric approach was proposed by Pedroni, Schneider and Lomax in 1996 [37]. Figure 3.19 displays the CT calibration curve implemented in the Eclipse Proton Planning software.

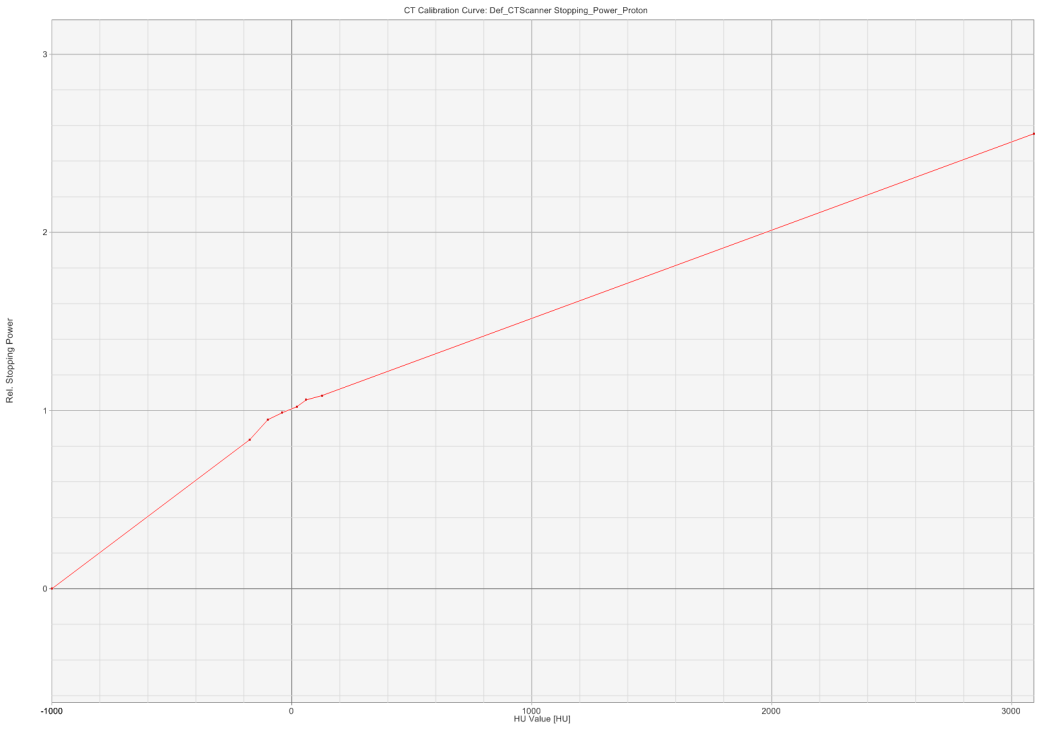

Figure 3.19: The CT value conversion curve from Varian Eclipse. Based on the stoichiometric method a CT calibration curve is obtained. In this plot the x-axis represents the HU values and the y-axis represent the relative proton stopping power.

Although the stoichiometric method provides a good estimate of the stopping power, it is important to note that the HU and the proton stopping power result from different physical processes and there is no clear-cut one-to-one relation between the two [38].

Proton Imaging

The systematic error of the conversion between the HU value and the proton stopping power is typically in the order of a few % [39] [15]. X-ray CT is like any other imaging modality prone to artefacts, in particular for imaging sites with metal implants such as dental fillings and medical prostheses.

To address this uncertainty one solution proposed is the use of proton CT. With a proton CT the proton beam is used to create an image of the patient. For proton CT the beam energy must be high enough for the protons to come to rest and deposit their Bragg peak beyond the patient, not inside the patient, along the beam axis. This energy is needed because proton CT is based upon the principle that the Bragg peak will be deposited in the detector behind the patient, and not in the patient, and with knowledge about the incoming proton beam energy and the distribution of the Bragg Peak position, one will obtain knowledge about the deposited energy in the patient and hence be able to deduce the stopping power of the patient tissue. Depending on what part of the body that is to be treated a maximum energy of more than 300 MeV is required from the accelerator.

Application of a Proton CT will give direct information regarding the proton behavior, in particular the range, in tissue, and it can potentially be less prone to artefacts due to high-Z materials [40]. In addition to this, the dose given to the patient during proton CT imaging can potentially be lower than for traditional X-ray CT with the same density resolution [41]. Using the treatment beam for imaging reduces the number of devices that otherwise would have to be in the treatment room. Most clinics today have X-ray imaging equipment in the treatment room, applied for positioning the patient and image guidance. This can either be a C-arm, which is a kV imaging system for planar images, a cone beam CT for acquisition of 3D imaging or even a full scale CT scanner on rails.

The X-ray CT is the working horse of medical imaging in cancer treatment and proton CT is still at the prototype level. The need for accurate dose predictions when applying protons is motivating the development of proton CT based dose plans and the need for such a development increases further with the rapid increase of the number of patients treated with protons. The development of better treatment delivery techniques will also depend upon an as correct as possible calculation of the proton range in a patient.

3.7 Pencil Beam Algorithms

A treatment plan will display the calculated dose distribution in the patient, and will provide instructions for the dose delivery equipment. The input is the patient geometry in terms of 3D CT information, and a radiation source with a set of given parameters, such as energy, beam shape and dose rate [42].

Pencil beam algorithms are currently the standard dose calculation algorithms for both scattered and scanned beam treatment. To calculate the dose to a given volume the dose distribution of multiple pencil beams are summed up. The calculated energy deposition is a function of radiological depth, and the lateral energy diffusion kernel K. The radiological depth in the patient accounts for the water-equivalent path length (WEPL) on the trajectory toward the point in question. The kernels are generated by Monte Carlo simulations or measurements, and they are radially symmetric for each pencil beam. Pencil beam dose calculation algorithms are fast and generally accurate, but have some shortcomings when introduced to inhomogeneities, especially lateral inhomogeneities [42] [15].

The geometry input for a pencil beam algorithm is a CT voxel geometry, and hence errors in the CT Hounsfield Unit value to proton stopping power conversion will lead to errors in the pencil beam algorithm's dose calculations.

Chapter 4

The Monte Carlo Simulation Method

An important goal of computer simulations within radiation therapy, is to make sure that the patient receives the correct dose through a detailed calculation of the interaction processes that takes place in the volume or medium under study. The Monte Carlo method is an accurate way of investigating particle interactions in a medium, and it is considered to be the "gold standard" within computer simulations where the aim is mimicking the fundamental interaction processes in nature. Monte Carlo simulations are widely used within radiation physics [15] [43].

Algorithms that are based on streams of random numbers are called Monte Carlo algorithms. The mathematical foundation for the Monte Carlo method is the Central Limit Theorem, which states that for a large number of independent random variables, the mean will be normally distributed [15] [43].

Particle Tracking Particle transport is a typical physical process described by cross sections, or interaction probabilities per unit length, and the Monte Carlo method is applied when describing particle transport through complex geometries. Each particle will have a pre-calculated probability for the various processes that can occur, and their outcome. The uncertainty in a Monte Carlo calculation depends on the number of histories, N. The error will be proportional to $1/\sqrt{N}$ [15] [43].

The tracking geometry is a geometrical model with well-defined materials that are characterized by their physical properties, such as elemental composition, electron density, mass density and mean excitation energy. This model can portray any geometry the user wants to investigate, for example

concrete shielding, beamlines or a patient anatomy. The results scored for a simulation run can be parameters such as; dose, energy loss, fluence, etc, this being determined by the user. The step size reflects the size of how far the particle under study moves between each calculation of probabilities for interactions in the defined geometry. The step size, chosen by the user, will affect the outcome. The step size should be small, to ensure a good resolution. However, smaller step size increases the computation time and the user should keep this in mind [15] [43].

Proton Physics

The accuracy of Monte Carlo simulations is obtained by the way the underlying physics is implemented in the code. The Bethe-Bloch equation addressed in chapter 2 governs the energy loss for protons downwards to 2 MeV. Other relevant theories such as Moliere's theory and Lewis's theory are implemented to ensure the scattering angle distribution and lateral displacement [15]. When creating a geometry in a Monte Carlo simulation, the elemental composition, the material density and the mean excitation energies are implemented for that given material. The material properties are often the latest recommended values given by ICRU (International Commission on Radiation Units and Measurements).

Monte Carlo based treatment planning algorithms are currently emerging, but are still too time consuming for daily clinical practice. However, as computing power continuously increase, Monte Carlo planning can become available for clinical use within the near future. Scanned beam delivery is likely to require a less complicated Monte Carlo model than scattered beam delivery since the latter relies on many different components in the beam line.

4.1 Monte Carlo Codes

4.1.1 FLUKA

FLUKA, abbreviated from FLUktuierende KAskade, is a general purpose tool for calculations of particle transport and interactions with matter. The original application of FLUKA was accelerator shielding, but its application now spans from investigating cosmic rays to radiation therapy. FLUKA can simulate the interactions of about 60 different particles in a large energy span. The FORTRAN language is used in the FLUKA Simulation tool [16].

Capabilities and limitations

To provide accurate simulations, modern physics models are implemented and the results checked against experimental data. Elements and composite materials are implemented in the geometry, with the recommended material properties from ICRU. The following list is a shortened excerpt from the FLUKA manual [16], summarising the physics behind transport of charged hadrons:

- Bethe-Bloch theory
- Mott correction to the Rutherford scattering cross section
- Optional delta-ray production and transport with account for spin effects and ionization fluctuations
- Shell and low-energy corrections derived from Ziegler
- Ionization potentials and density effect parameters according to Sternheimer, Berger and Seltzer
- Non-ionizing energy losses
- Displacements Per Atom (DPAs)
- Special transport algoritm, based on Molière's theory of multiple Coulomb scattering improved by Bethe
- Accurate treatment of boundaries and curved trajectories in magnetic and electric fields
- Automatic control of the step
- Path length correction
- Spin-relativistic effects at the level of the second Born approximation
- Nuclear size effects (scattering suppression) on option
- Fano correction for heavy charged particle multiple scattering
- Single scattering: algorithm based on the Rutherford formula with screening factor in the form used by Molière, integrated analytically without any approximation. Nuclear form factors and spin-relativistic corrections at the first or second Born approximation level accounted for by a rejection technique

- Correction for cross section variation with energy over the step
- Bremsstrahlung and electron pair production at high energy by heavy charged particles, treated as a continuous energy loss and deposition or as discrete processes depending on user choice
- Muon photonuclear interactions, with or without transport of the produced secondaries

FLUKA input

The user defined input to FLUKA is written in an ASCII standard input file with the extension .inp. A typical FLUKA input file may contain the following:

- Title and comments
- Description of the problem geometry
- Definition of the materials
- Material assignment
- Definition of the particle source
- Definition of requested detectors that the user wants to calculate varoius physical quantities such as dose, fluence, etc.
- Definition of biasing schemes
- Definition of problem settings such as energy cut-offs, step size, etc.
- Initialisation of the random number sequence
- Starting signal and number of requested histories

The user can define the beam by choosing the particle, particle energy or momentum, its starting position and direction directly in the input file. For more complex beams such as a therapeutic beam of protons, a special routine has to be written, compiled and linked to the input file.

Geometry

The user can define the geometry of the problem through assigning different bodies and regions. A "body" can for example be a cylinder with a certain position, length and radius, and a "region" is a zone with a material assigned to it. The regions are defined by the bodies.

The geometry defined for the setup must be surrounded by a region of "black hole". This is a fictitious material used to terminate particle trajectories.

4.1.2 Other Monte Carlo codes

Geant4

Geant4 (abbreviated from GEometry ANd Tracking) was designed in the 1990's by an international collaboration of institutes, high energy physics experiments and universities. The Geant4 Collaboration was established in January 1999 in order to continue the development and improvement, and to provide user support. Geant4 is based on object oriented programming in C++, and is the successor of the GEANT series of software toolkits developed by CERN [44].

MCNPX

MCNPX, abbreviated from Monte Carlo N-Particles eXtended, is written on Fortran 90 and is developed by Los Alamos National Laboratory. It is mainly used for simulation of nuclear processes [45].

VMCpro

VMCpro is a relatively new Monte Carlo tool, specifically developed to be a fast Monte Carlo treatment planning system. It is developed in order to simulate proton transport in human tissue [46].

Chapter 5

Monte Carlo Simulations, Methods and Results

The overall goal of this project has been an investigation of how a proton beam interacts with matter and how an introduction of different materials in the beam path will affect the key parameters relevant for a therapeutic proton beam. The parameters most prominent from a particle therapy point of view is; range, dose deposition and lateral spread. This chapter will describe the simulations performed as well as their motivation and the results.

Tools The FLUKA Monte Carlo code (version 2011) and Varian Eclipse Proton Planning have been used in this project. FLUKA was used in the two first parts, the investigation of proton range and the creation of a spread-out Bragg peak (section 5.1 and section 5.2), while both FLUKA and Eclipse were used in the final part, creating and comparing simple treatment plans (section 5.3). The program Gnuplot was used for plotting the data outcome.

FLUKA

As mentioned in chapter 4, FLUKA can simulate the interactions of about 60 different particles in a large span of energies.

All the geometry, the materials and the beam parameters are defined by the user. The resulting energy deposition, dose and dose deposition, fluence etc can be registered ("scored") for any region or plane defined by the user. The parameters needed to perform the simulations are registered or linked to the input card.

Varian Eclipse Proton Planning

The Varian Eclipse Proton Planning is Varian's treatment planning software for proton therapy treatment planning. The proton dose calculation algorithm supports both passive beam scattering and active beam scanning technique. The software is configured to enable correspondence between the treatment planning tool and a proton therapy machine. A proton beam delivery system has three main elements: the beam production area, the beam transport line system and the clinical beam application area. Eclipse contains no information about the beam production area or the beam line system leading to the nozzle (beam application). The nozzle contains most of the beam modifying elements used to manipulate the proton beam. The dose reported to the user is calculated on a three-dimensional array of voxels on a Cartesian grid. The calculation algorithm applied is the Proton Convolution Superposition (PCS) version 11.0.30/31 [35].

5.1 Range - Effects of inhomogeneities

Simulation set-up In order to investigate the effect that inhomogeneities have on the position of the Bragg peak, the FLUKA geometry editor, the *Geoviewer*, was used to design a simple cubic phantom of homogeneous water surrounded by air. Since the human body consists of approximately 60 % water [47], a phantom made of water is an appropriate media to work with in this context. The cube is $20 \times 20 \times 20$ cm^3. The simulations were typically performed with 5 cycles, with 10 000 primary protons each, in a pencil beam that was aimed in the positive z-direction with $x = y = 0$. A monoenergetic proton pencil beam with a lateral Gaussian distribution spread, with an FWHM value of 0.6 cm, was applied. The energies applied were 100 MeV and 150 MeV. The FWHM value is an approximation to the conditions in a real clinical beam [48]. The beam originates from $z = -1$ cm. When studying the effect of inhomogeneities, a small volume of varying material was implemented in the phantom geometry, positioned in the centre of the beam path, located at 5 cm depth. The proton beam in a homogeneous water phantom was used as a control set-up, the dose scoring from this reference phantom is shown in figure 5.2. Figure 5.1 displays the phantom design in Geoviewer.

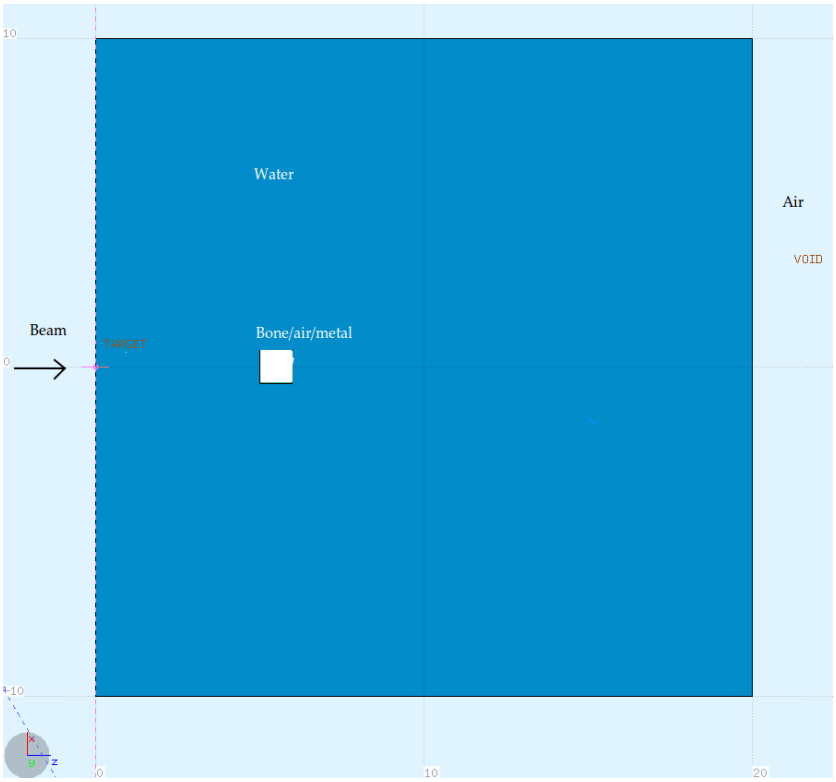

(a) A 2D layout of the phantom set-up in the FLUKA Geoviewer program.

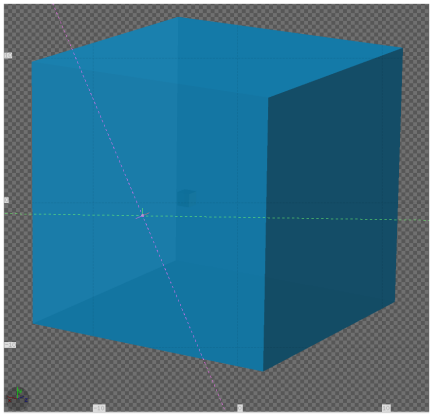

(b) The water phantom in 3D view. Image from the FLUKA Geoviewer program.

Figure 5.1: The $20 \times 20 \times 20$ cm^3 water phantom set up in FLUKA. At 5 cm depth there is a $1 \times 1 \times 1$ cm^3 cube of material that could be other than water.

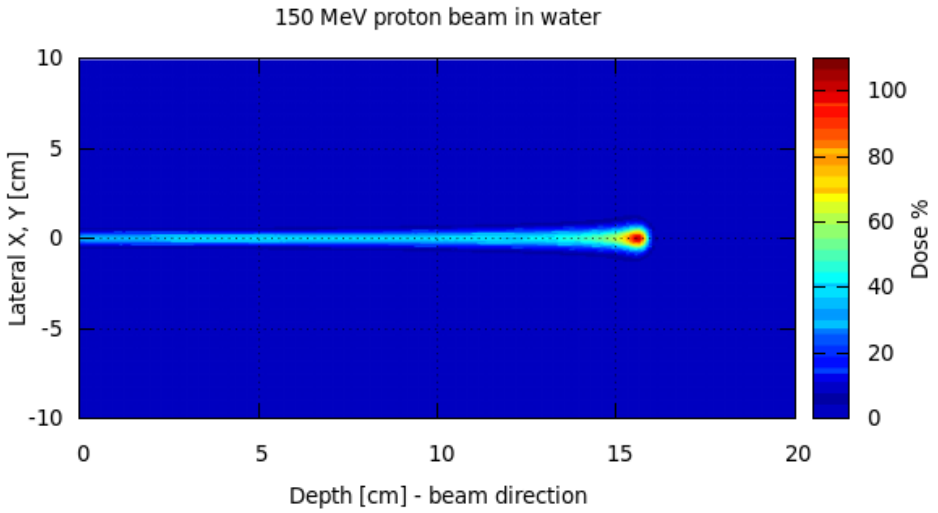

(a) The dose deposition as a function of depth.

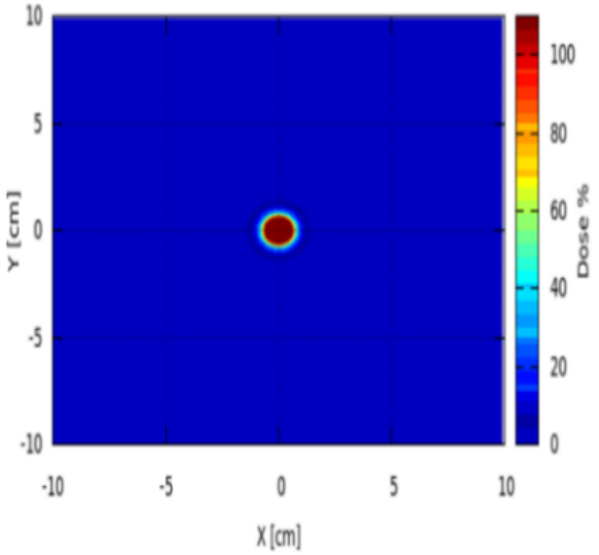

(b) The beam spot displayed as seen from the beams' eye-view.

Figure 5.2: FLUKA Monte Carlo simulation. A 2D display of the dose deposition from a 150 MeV proton beam in water. Image a) shows the dose distribution along the beam axis, with the distinct sharp dose deposition at the end of the proton range, and with the beam broadening as a result of scattering in the water. Image b) shows the dose deposition from the beam's point of view. A lateral spread of FWHM of 6 mm was applied for this simulation.

Bone

Human bone will vary in thickness and density depending on where in the body the bone is located, on the age and gender of the patient and also the on patient's health.

In FLUKA there is a material database containing different compounds available for description of the geometry and materials in the variety of different experiments that FLUKA is used for. There is a folder with biological compounds such as blood, skin and bone. There are also descriptions of different kinds of bone, with density ranging from 1.8 g/cm^3 (cortical bone, ages 2-5 years) to 1.92 g/cm^3 (cortical bone, adult). For this project the bone with the density 1.85 g/cm^3 was chosen as the standard. This bone density corresponds to a Hounsfield unit of +1450. Figure 5.3 shows the resulting dose profile from a proton pencil beam when traversing into a water phantom with a cube of bone positioned at 5 cm depth. As can be seen the Bragg peak is shifted about 0.8 cm in the negative Z-direction compared to the Bragg peak position for a similar proton beam in a homogeneous water phantom.

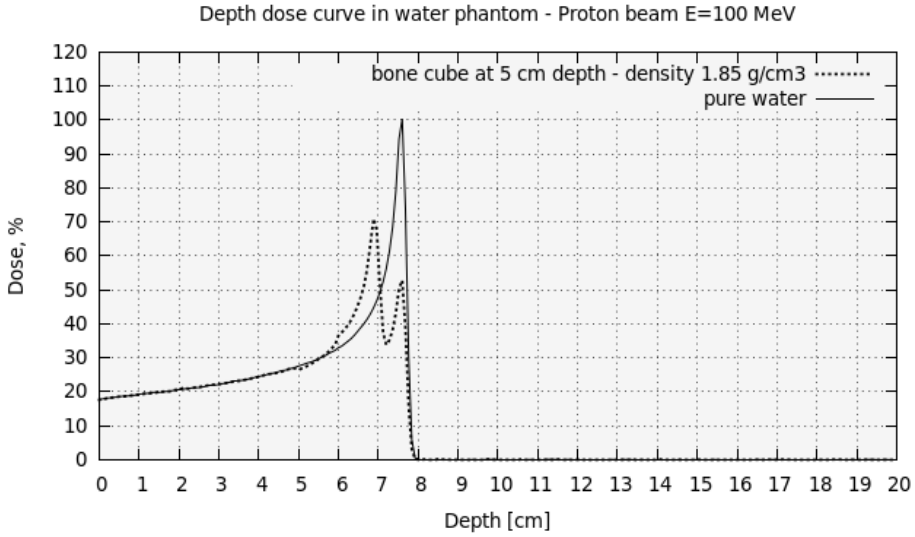

(a) A 100 MeV proton beam

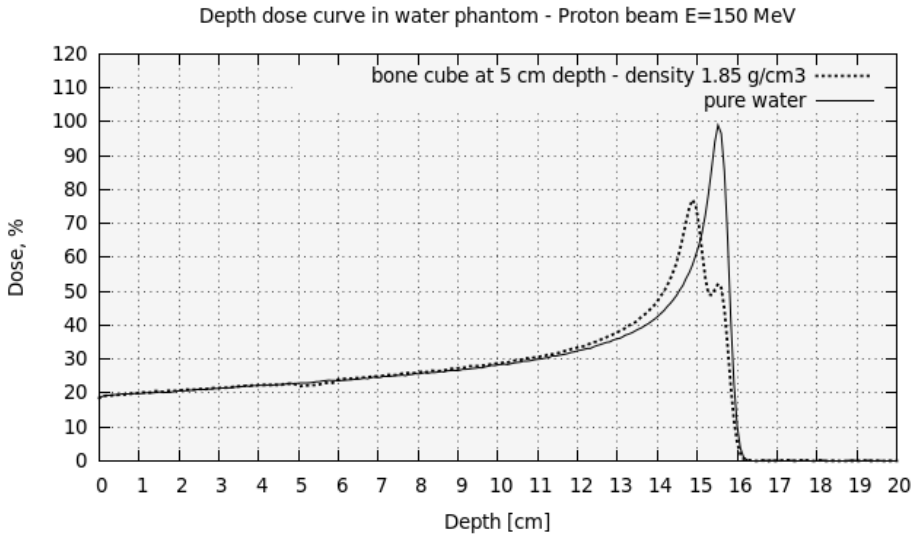

(b) A 150 MeV proton beam

Figure 5.3: FLUKA Monte Carlo simulation. Dose profile resulting from a proton beam traversing a water phantom with a bone cube located at 5 cm depth. Image a) result from a 100 MeV proton beam, image b) result from a 150 MeV proton beam

Air

Examples of anatomic sites with a high concentration of air are the lungs, the rectum and the intestines. The lungs are challenging to treat with radiation, not only due to the big differences in density, but also due to the respiratory movement. Head and neck cancers have been a treatment site that has been considered appropriate to treat with particles, since there is little movement of, in and around the target. The head and neck tumours can be relatively deep-seated and will almost always be located adjacent to sensitive structures. In addition the head and neck can be positioned and fixated with high precision and one can thus reduce the uncertainty due to patient movement. However, there can be physiological changes that include anatomical variations that can alter the proton range. Examples of this are the nasal cavities. These can be filled with fluid or they can be empty, in the latter case adding an air cavity in the geometry. This cavity filling can change from day to day or even during a day, causing an uncertainty in the water equivalent length for the proton track leading towards the target volume.

The impact air will have on the proton range and behaviour was estimated by using the phantom mentioned above, now with a cube of air located in the beam path, at 5 cm depth. The resulting depth dose profile can be seen in figure 5.4. As can be seen in the figure; the Bragg peak is shifted about 1.0 cm in the positive Z-direction compared to the situation for an otherwise equal proton beam traversing a homogeneous water phantom.

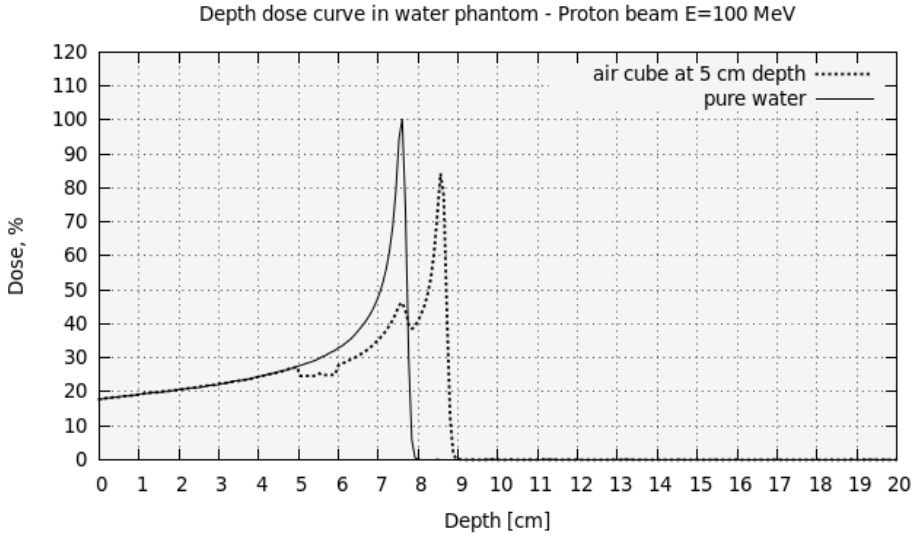

(a) A 100 MeV proton beam.

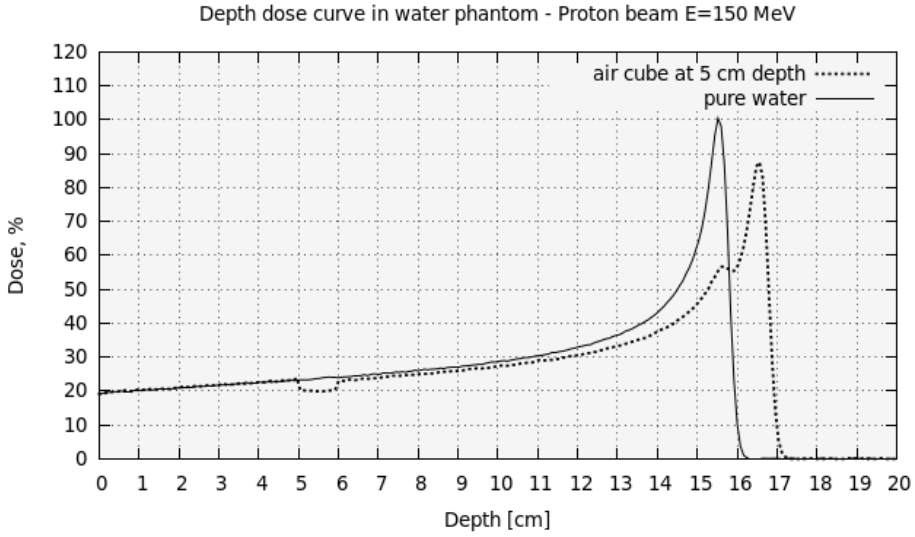

(b) A 150 MeV proton beam.

Figure 5.4: FLUKA Monte Carlo simulation. Dose profile resulting from a proton beam traversing a water phantom with a cube of air located at 5 cm depth. Image a) result from a 100 MeV proton beam, image b) result from a 150 MeV proton beam.

Implants made of metal

Implants are commonly used to replace or support teeth, joints and bone structures. The materials used varies with location and the functional criteria for the implant. In radiation therapy, medical implants can introduce complications. Since medical implants commonly consists of metal or metal alloys, their densities can be 2-3 times higher than the density of bone, which is otherwise the most dense material naturally occurring in the body. These high density materials can cause artefacts in CT images, which in turn can lead to errors in the dose calculations.

To investigate how the proton range is affected by implants, a cube of stainless steel (with density $\rho = 8.0\ g/cm^3$) and a cube of aluminium (with density $\rho = 2.7\ g/cm^3$ was applied in the simulations. The resulting depth dose profile can be seen in figure 5.5 and figure 5.6. The Bragg peak from the proton beam traversing the steel cube is shifted about 4.5 cm in the negative Z-direction and the Bragg peak from the proton beam traversing the aluminium cube is shifted about 1.1 cm in the negative Z-direction, both positions are relative to the position of the Bragg peak from an otherwise equal proton beam traversing a homogeneous water phantom.

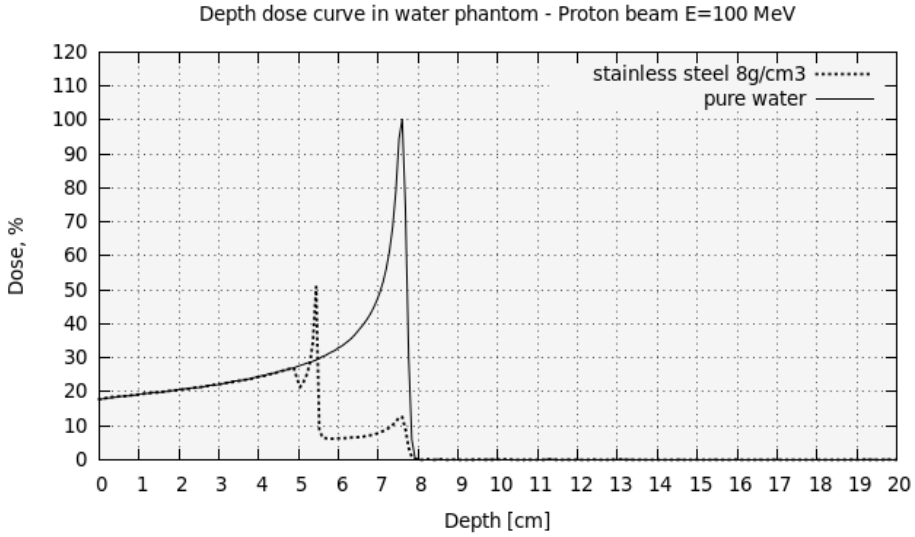

(a) A 100 MeV proton beam.

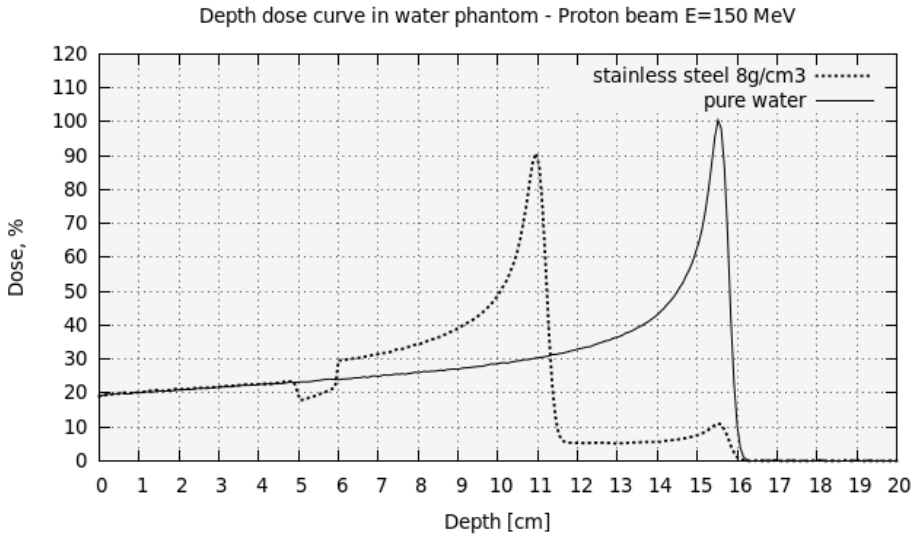

(b) A 150 MeV proton beam.

Figure 5.5: FLUKA Monte Carlo simulation. Dose profile resulting from a proton beam traversing a water phantom with a stainless steel cube located at 5 cm depth. Image a) result from a 100 MeV proton beam, image b) result from a 150 MeV proton beam.

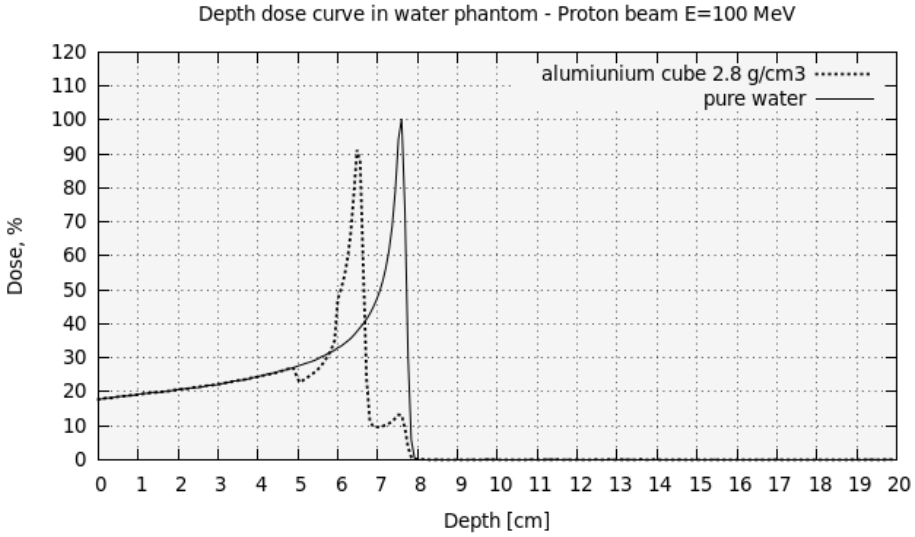

(a) A 100 MeV proton beam.

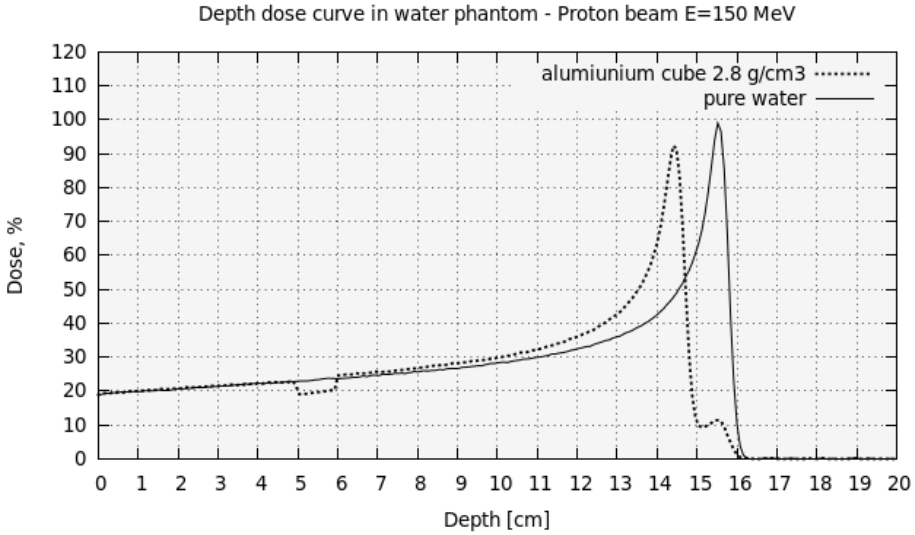

(b) A 150 MeV proton beam.

Figure 5.6: FLUKA Monte Carlo simulation. Dose profile resulting from a proton beam traversing a water phantom with an aluminium cube located at 5 cm depth. Image a) result from a 100 MeV proton beam, image b) result from a 150 MeV proton beam.

Summary of the Results

The range of the proton beam depends primarily on the density, atomic number and mean ionization energy of the media traversed. The figures 5.3, 5.4, 5.5 and 5.6 show how the depth dose distribution of a proton pencil beam is affected by a cube of the materials; bone, air, steel and aluminium respectively, all in turn located at and from 5 cm water depth in the proton beam path. In addition to a shift in the range, one can also notice a second consequence of inserting a material in the water phantom. Due to scattering in the phantom and the stochastic nature of the interaction mechanisms in nature, some protons will pass by the cube and thus only interact in water. This results in a small peak, located at the same depth as the Bragg peak in the unperturbed homogeneous water phantom. This effect will be less pronounced when the heterogeneity is broader or closer to the surface, since a larger fraction of the scattered protons can not pass by the edges. The proton fluence in 2D is shown in 5.7, here one can see that some protons pass outside the bone volume. Table 5.1 summarizes the shift in the Bragg peak position as a result of different material in the beam path.

Table 5.1: Range shift as a result of a 1 cm^3 material cube in beam path.

Material	*Range shift compared to beam in a homogeneous water phantom.*
Water	0 cm
Bone	-0.8 cm
Air	1.0 cm
Aluminium	-1.1 cm
Steel	-4.5 cm

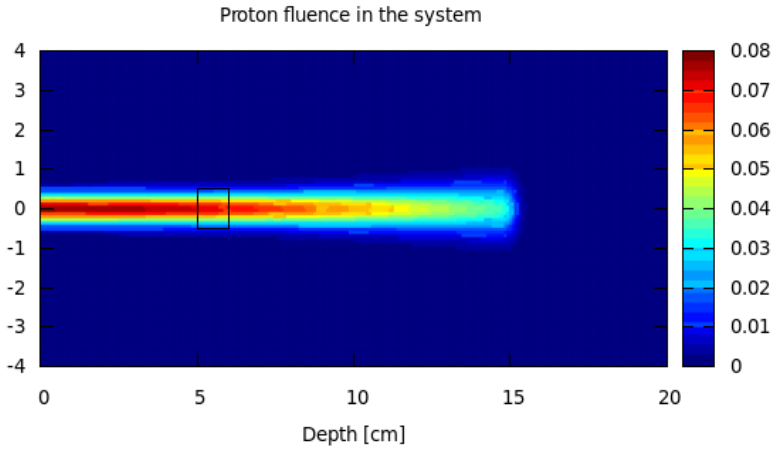

Figure 5.7: FLUKA Monte Carlo simulation: The 2D proton fluence distribution in units of protons pr cm^2 pr primary particle. The phantom applied in this simulation is a phantom with a cube of bone located at 5 cm depth (marked as a small square in figure). Although most the protons traverse through the cube, some have their path outside the bone volume, thus only interacting with water.

Since various materials have different impact on the proton range, anatomic sites with a heterogeneous structure need special care when considering proton therapy. In proton therapy clinics, the usual clinical routine when directing treatment fields towards the target volume in the dose planning stage involves avoiding beam directions through heterogeneous media. Especially sites with metal implants should be avoided, both due to the large impact on proton range, but also in order to minimize imaging artefacts.

5.2 Creation of Spread-out Bragg Peak

A tumour is extended in three dimensions and located at a certain depth in the body. This means that the treatment unit should be able to deliver a homogeneous dose to such a volume.

The Kleeman-Bragg rule gives us the relation between the energy (in MeV) of the particle and the resulting range. For a proton beam traversing water, the beam range (in cm) is given by equation 5.1 [49].

$$R = \alpha E^{p_0} \tag{5.1}$$

Where $\alpha = 0.0022$ and $p_0 = 1.77$

In order to produce an SOBP one needs to add several beams of different initial energy in a certain way. To obtain a flat dose plateau at a maximum depth R_0, with a width given by a fraction χ of the maximum depth, consisting of n different energy intervals, the range of each contributing beam $(k = 1, 2, ...n)$ will be determined by equation 5.2.

$$r_k = \left[1 - \left(1 - \frac{k}{n}\right)\chi\right] R_0 \tag{5.2}$$

The corresponding energy of each beam is given by equation 5.3

$$e_k = \left(\frac{r_k}{\alpha}\right)^{\frac{1}{p_0}} \tag{5.3}$$

The shape of the SOBP depends on the weight of each beam. The distal Bragg peak has the highest weight and the proximal Bragg peak has the lowest weight. The weight w_k of the beams is given in equation 5.4.

$$w_k = \begin{cases} 1 - \left(1 - \frac{1}{2n}\right)^{1-\frac{1}{p}} & \text{for} \quad k = 0 \\ \left[1 - \frac{1}{n}\left(k - \frac{1}{2}\right)\right]^{1-\frac{1}{p}} - \left[1 - \frac{1}{n}\left(k + \frac{1}{2}\right)\right]^{1-\frac{1}{p}} & \text{for} \quad k = 1, ..., n-1 \\ \left(\frac{1}{2n}\right)^{1-\frac{1}{p}} & \text{for} \quad k = n \end{cases} \tag{5.4}$$

The parameter p will vary slightly with energy, depth and the width of the SOBP. A constant p-value of 1.77 will produce an SOBP, but the dose plateau will be slightly tilted instead of flat, as noted by [49].

Using these equations one can create an SOBP. For this project the maximum depth of 15 cm for the dose plateau and an SOBP width of 5 cm was chosen. This was performed by two different methods;

- Modulation of the beam energy in a *passive* way by applying a range modulator in the beam. This modulator was a ridge filter.

- Modulation of the beam energy in an *active* by altering the energy and weight in the source.

5.2.1 Passive Modulation

When creating a therapeutic beam with passive modulation, the idea is to apply material in the beamline, and let the beam interact with the material, in order to produce a spread-out Bragg peak in the target volume. There are numerous materials and designs to choose from, as mentioned in chapter 3. For this project an aluminium ridge filter was chosen. A ridge filter is a static hardware component in the beamline and it is therefore less complicated to simulate, than for instance a moving or rotating component. Still the underlying principle is the same; the initially monoenergetic beam must pass through the material in a way that makes the resulting dose deposition shaped so that a spread-out Bragg peak is created. The position of the SOBP can be adjusted by interchanging the range shifters in the beam line.

The ridge filter is composed of ridges with a curved triangular shape. Accurate drawings of ridge filters in clinical use were not possible to retrieve due to company non-disclosure policy. Hence, the dimensions of the ridge filter used in the simulations were designed based on the SOBP formula shown above. In order to estimate how the thickness of aluminium affects the proton range in water, simulations of a 150 MeV proton beam in water was carried out while applying blocks of aluminium of varying thicknesses in front of the water phantom. A linear relation between the aluminium thickness and the resulting proton range in water was found and the resulting plot is shown in figure 5.8.

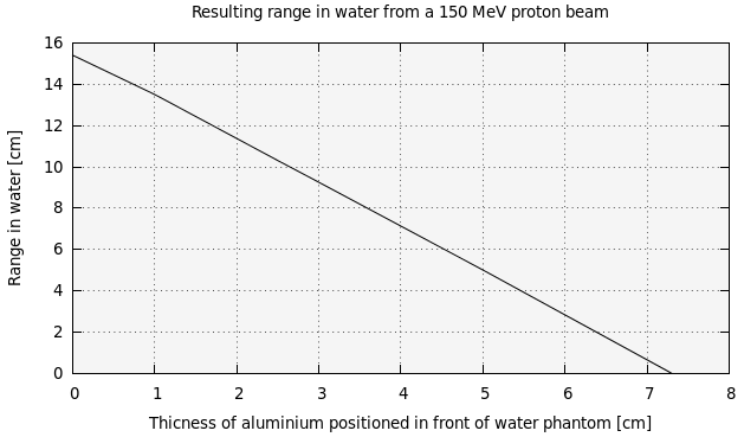

Figure 5.8: FLUKA Monte Carlo simulation. The resulting range in water from a 150 MeV proton beam traversing a block of aluminium located in front of the water phantom. The range in water depends linearly on the thickness of the block. This relation was used to design the ridge filter.

Based on this thickness-range relation and the SOBP formula with depth, modulation width and weighting factors, the ridge filter could be designed. Again an energy modulation width of 5 cm was chosen, with 10 intervals. Each ridge is 0.5 cm wide and about 2.7 cm deep, and consist of 20 "plates". Each plate have a thickness that corresponds to the weight of that given beam range, as can be seen in the figures 5.9 and 5.10. In table 5.2 the dimensions for each step in the ridge is given.

Table 5.2: Alumium thickness and step width.

Aluminium height [cm]	*Step width [mm]*
2.6	0.048
2.4	0.100
2.2	0.108
1.9	0.117
1.7	0.129
1.5	0.145
1.25	0.167
1.0	0.200
0.75	0.259
0.5	0.414
0.2	0.813

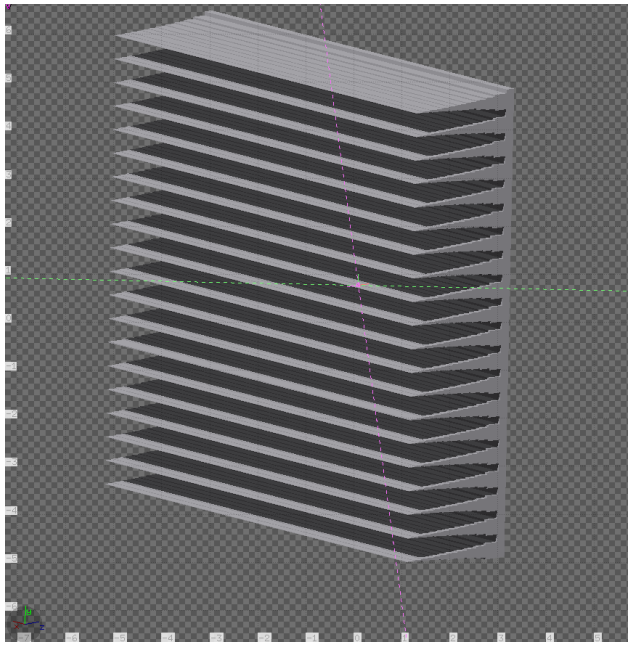

(a) A 3D image of the ridge filter.

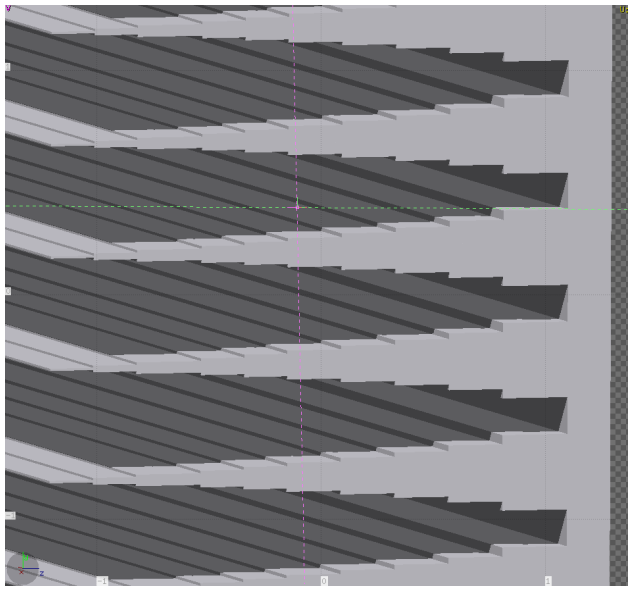

(b) A 3D close-up view of the ridge filter.

Figure 5.9: An aluminium ridge filter designed to create a spread-out Bragg peak. The ridges has a step-like design, where the width of each step (in the y-direction) corresponds the weight of the beam with energy determined by the thickness (in the z-direction).

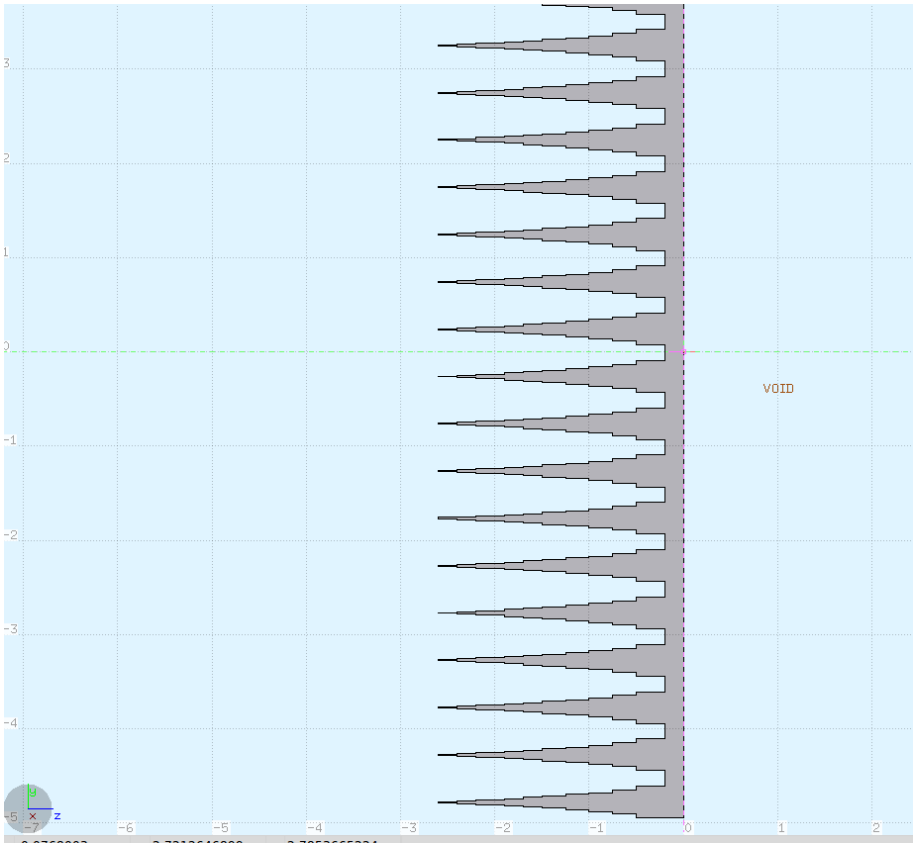

Figure 5.10: A 2D image of the ridge filter.

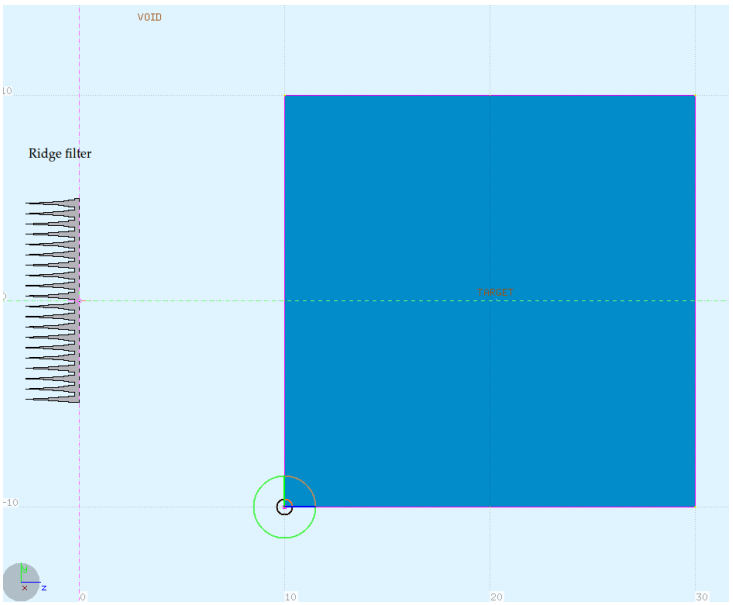

(a) The setup with 10 cm distance between the ridge filter and water phantom.

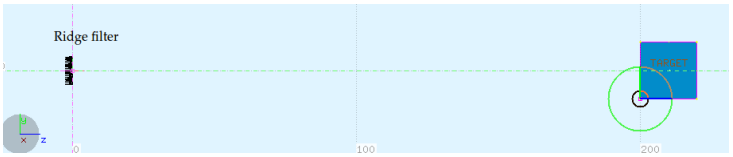

(b) The setup with 2 m distance between the ridge filter and water phantom.

Figure 5.11: Simulation geometry setup in FLUKA. The aluminium ridge filter is positioned in front of the water phantom in order to create an SOBP in the water phantom. In figure a) the distance between the ridge filter and the water phantom is 10 cm, and in figure b) the distance is 2 m. The void surrounding the setup is filled with air.

Results

Dose Deposition When a ridge filter is used in a clinical beam, the pencil beam originating from the particle accelerator will be scattered to create a homogeneous proton field. In the simulations run in this project a proton field with dimensions 5×5 cm^2 was applied. The effect of distance in air between the ridge filter and the phantom was investigated by positioning the ridge filter 2 m away from the phantom, and 10 cm from the phantom respectively, as illustrated in figure 5.11. The resulting SOBP is visualized in figure 5.12. The dose profile shows a relatively flat dose plateau at the desired depth (from 10 cm to 15 cm depth).

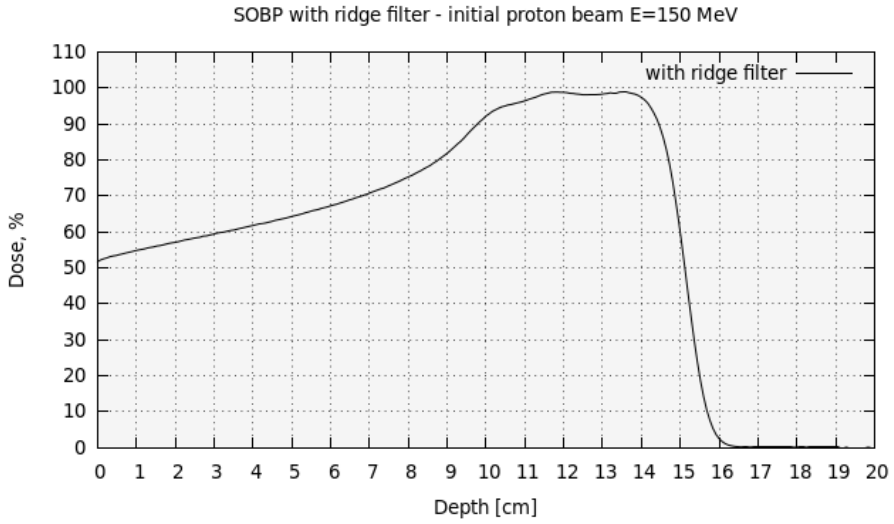

Figure 5.12: FLUKA Monte Carlo simulation. The SOBP as a result of a monoenergetic proton field of 150 MeV traversing an aluminium ridge filter.

In particle therapy clinics, the ridge filter station where the required ridge filter for each treatment situation will be inserted into the beamline is a component of the beamline equipment and this station is usually located around 2 meters from the patient. As can be observed in figure 5.13, the 2D dose distribution is sharper and more confined when the ridge filter is located close to the phantom. This is due to the scattering that the protons will experience while traversing air. In clinics where this type of energy modulator is used, the field is further adjusted to the target volume with collimators and compensators, which in turn is located close to the patient.

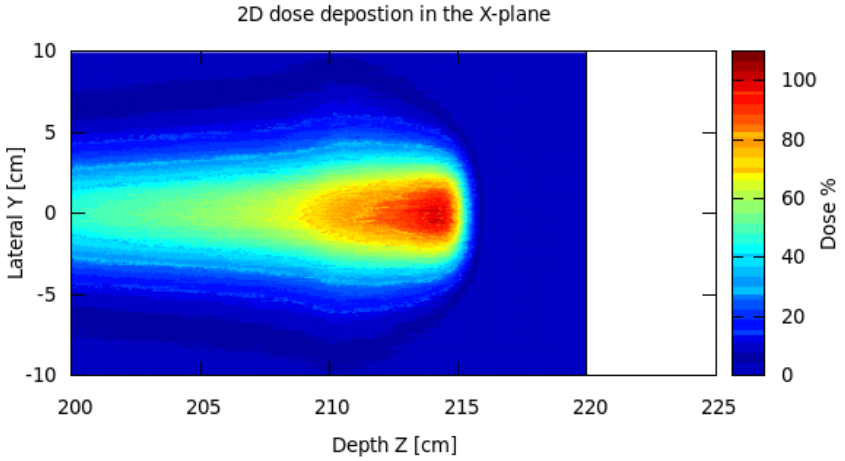

(a) The ridge filter located 2 m from the phantom.

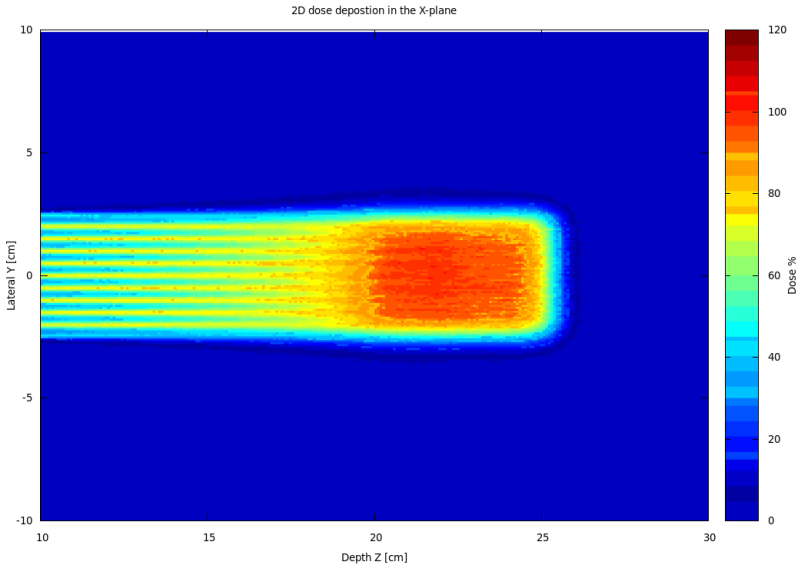

(b) The ridge filter located 10 cm from the phantom.

Figure 5.13: FLUKA Monte Carlo simulation. The 2D dose distribution in a water phantom, resulting from a 5×5 cm^2 150 MeV proton beam traversing an aluminium ridge filter located a) 2 meters from the phantom, and b) 10 cm from the phantom.

Neutron Production In addition to the investigation of dose distribution, the issue of radiation induced secondary particles is inherent in particle therapy. When beam losses occur, secondary radiation will be produced. By scoring the neutron fluence in the whole system, one can see that beamline components can induce neutron dose that is difficult to completely avoid. To reduce unwanted dose from radiation induced neutrons, the energy modulator should be positioned at some distance from the patient. If the ridge filter were located closer to the patient, neutron contamination from the ridge filter would be more pronounced. In figure 5.14 the neutron fluence for the whole geometry system, ie the ridge filter, the water phantom and the surrounding air, is visualized. This production of neutrons would come in addition to the neutron contamination from the collimator systems that is needed to tailor the field in order to limit the dose to the target volume. In order to thoroughly quantify the production of neutrons in all steps leading towards the patient, and its resulting additional dose to the patient, one needs a detailed model of a clinical beamline and gantry. This is beyond the scope of this master thesis project.

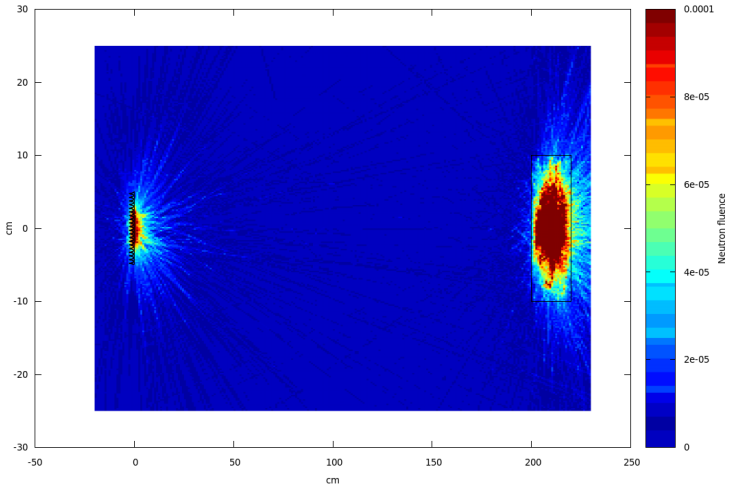

Figure 5.14: FLUKA Monte Carlo simulation. The neutron fluence is shown in color wash for the whole geometry system, with the ridge filter located 2 meters away from the phantom.

5.2.2 Active Modulation

In order to create an SOBP via active modulation, the energy distribution and beam position needed to be modulated by editing the `source.f` user routine in FLUKA. The `source.f` file must be written in FORTRAN code, compiled and linked to the input file for the simulation.

The SOBP formulas 5.2, 5.3 and 5.4 shown above were used to generate a list of energies and corresponding weights, reflecting the probabilities for each proton to be assigned that given energy. A do-loop sampled the energies and cumulative weights from the list and assigned it to the particles generated. Details from the script can be found in Appendix B. In table 5.2 the energies and weights needed in order to create an SOBP with maximum depth $R_0 = 15\ cm$, modulation width 5 cm and 10 energy intervals are listed. For these parameters, a p-value of 1.6 was chosen as it gave a resulting SOBP with a flat dose plateau at the desired depth. Table 5.3 summarizes 10 energy intervals, ie 11 beam energies and corresponding weights, which could be applied in order to create an SOBP with maximum depth 15 cm and a modulation width of 5 cm.

Table 5.3: Beam energies and weights calculated to create a spread-out Bragg peak with maximum depth of 15 cm, modulation width of 5 cm and 10 energy intervals.

Range in water [cm]	*Energy [MeV]*	*Weight*
10.0	116.5	0.01905
10.5	119.8	0.04007
11.0	123.0	0.04314
11.5	126.1	0.04691
12.0	129.2	0.05167
12.5	132.2	0.05793
13.0	135.1	0.06667
13.5	138.1	0.07996
14.0	140.9	0.10366
14.5	143.7	0.16577
15.0	146.5	0.32517

In order to obtain a smooth curve for the dose plateau covering the target volume, the SOBP was split into 51 energies with equally spaced energy intervals. The energies and weights were calculated and implemented in the source.f user routine. The energies were listed as `DATA ENEDGE` in units of GeV and the weighting factors were added to a cumulative spectrum listed in `DATA`

CUMPR. The full input card and source.f script are shown in appendix B. The simulations were run in 5 cycles each with 500 000 primaries in order to obtain good statistics and a smooth dose distribution. The simulation ran for about 1-2 hours.

Results

For the active modulation, a system resembling a spot scanning system was developed. The result is displayed in figure 5.15.

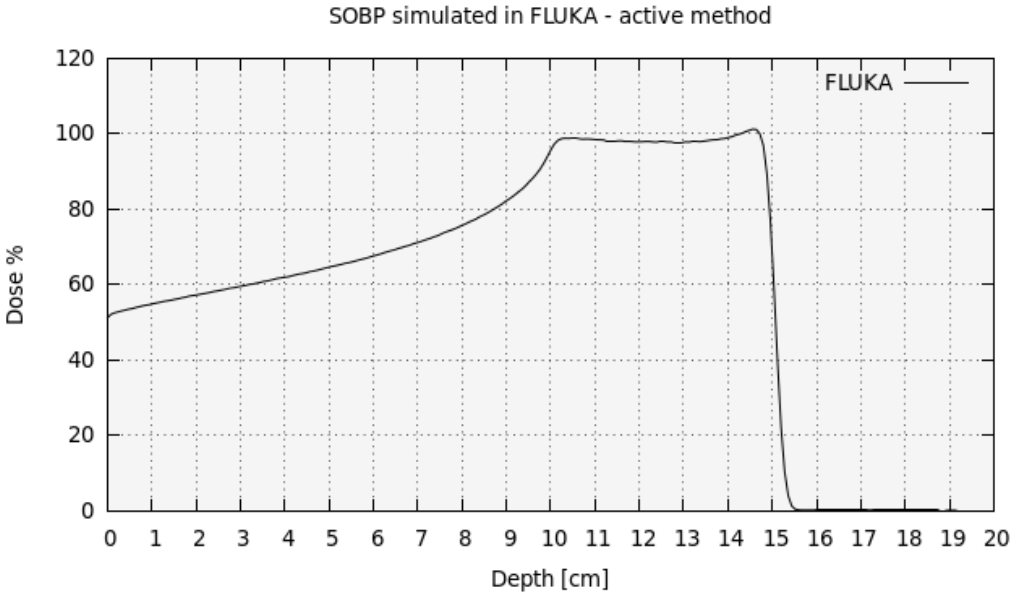

Figure 5.15: FLUKA Monte Carlo simulation. The SOBP produced with active modulation of the beam in FLUKA. The resulting beam is composed of 50 energy intervals, ie 51 equally spaced beam energies ranging from 116 MeV to 146 MeV.

The weighting scheme is generated with formula 5.4, referred to above. To find the optimal weighting of the energies to obtain the desired SOBP, the p-value needs to be adjusted. The p-value can vary for different depths and energies. For the depth chosen for this project (5 cm SOBP covering the depth from 10 cm to 15 cm), the p-value 1.6 proved to be an adequate choice. Figure 5.16 shows the resulting SOBP when using the three different p-values (1.3, 1.6, and 1.9). The dose plateau is tilted in one direction or the other if a suitable p-value is not applied.

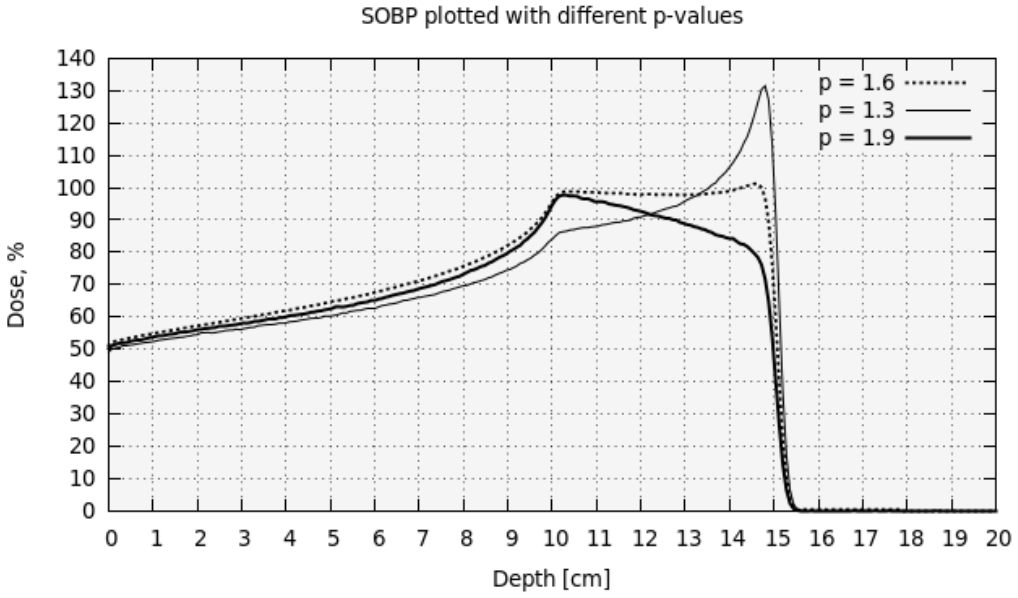

Figure 5.16: FLUKA Monte Carlo simulation. The SOBP plotted with three different weighting schemes. The beam energies are identical, but the p-value from the weighting formula 5.4 is different in the three cases with the p-values; 1.3, 1.6 and 1.9.

When the beam in not slowed down with material in the beam line, as is the case with passive modulation, the resolution of the treatment avoids to be degraded during energy modulation. In this context, the resolution of the treatment refers to in which degree the dose deposition is confined to the target volume, regardless of the shape and position of the target volume. Because the beam will be scattered both in the modulators and in the air in front of the patient, passive modulation will lead to a less precisely confined treatment beam than what is achievable with active modulation. With active modulation there will still be some scattering of the beam, but the newest gantries in proton clinics today, such as the Gantry 2 at PSI in Villigen, Switzerland, will enable the distance in air to be as short as possible [48]. This is obtained by a mechanism that allows an adjustment of the treatment snout position relative to the patient surface during treatment. The scattering of the beam inside the patient will still determine the lowest limit for the treatment resolution.

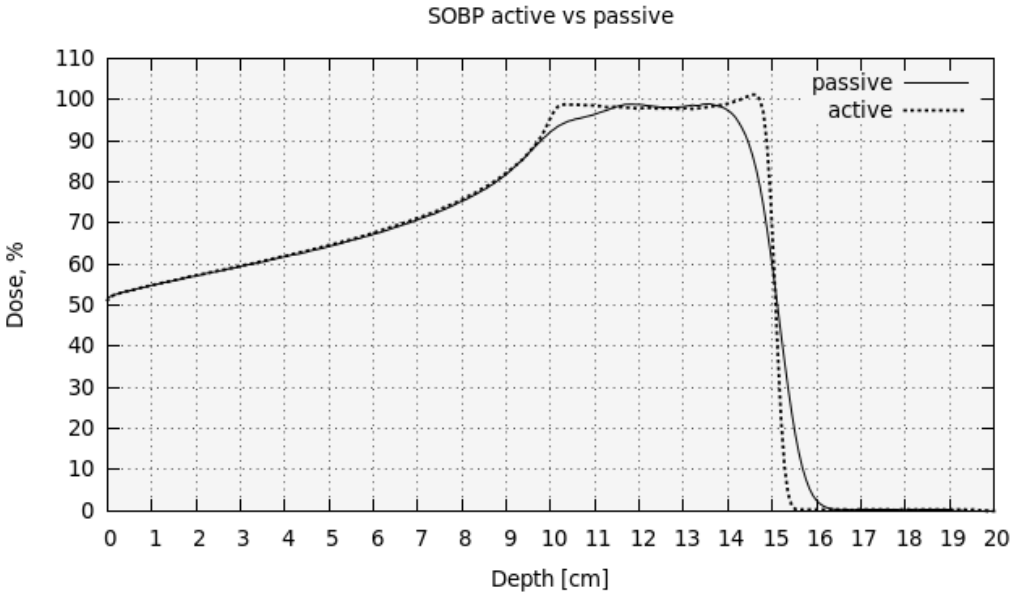

Figure 5.17: FLUKA Monte Carlo simulation. SOBP of modulation width 5 cm. Passive modulation and active modulation.

Figure 5.17 displays the SOBP produced both with passive (solid line) and with active modulation (dashed line). The distal dose falloff is steepest when applying active modulation. However it is important to note that there are ways of making the passive modulation more well defined than it was done in this work. By using other types of materials in the modulator, for instance PMMA, and in addition applying collimation systems in the beamline, one can obtain a sharper dose deposition than the one presented in figure 5.17. To simulate this would require detailed descriptions and technical drawings of a real clinical beamline, and this is beyond the scope of this master thesis project.

5.3 Homogeneous Dose to an Extended Volume

In the final simulations made in this project, the knowledge obtained in the work presented in the previous sections was applied in order to create treatment plans in FLUKA, and to compare these with the output from equivalent treatment plans created in Eclipse.

5.3.1 Phantoms

A few basic phantoms were designed. The basic geometry was, as in the previous sections, a water cube with dimensions $20 \times 20 \times 20$ cm^3. The volume to be treated is a $5 \times 5 \times 5$ cm^3 cube located at 10 cm depth with the central beam axis in its center.

- The first case is the homogeneous water phantom as described above. This is the simplest case to simulate, and one should expect the output from FLUKA and Eclipse to be almost identical.

- In order to see how the therapeutic beam is affected by different materials, a volume of bone, air or aluminium was added to the phantom. The volume was 1 cm thick (in z-direction), and with an area of 5×5 cm^2, located in the middle of the central beam axis to symmetrically cover the entrance of the treatment volume. In order to reach the target volume, the energy assigned to the proton beam should be adjusted according to the water equivalent depth in the phantom. The results from the previous sections were used to make these adjustments in FLUKA. The phantom design is shown in figure 5.18.

- The final phantom case is an asymmetrical set-up where the material volume from the previous case has been split in half, and thus only one half of the beam particles had the material in its forward path. Since a material other than water is blocking half the entrance to the target volume, the algorithm is modified to assign one set of energies to half the field, and a different set of energies to the other half of the field.

5.3.2 Simulation Set-up in Eclipse

In treatment planning software such as Eclipse, the input is the file containing the patient geometry, and the source and beamline properties and constraints. In this project treatment plans were generated using the multi-field uniform dose scanning technique, with one field direction. The treatment volume was defined as a Planning Target Volume (PTV), a $5 \times 5 \times 5$ cm^3

water cube located at 10 cm depth. For all the treatment plans, the lateral margins were set to 0.5 cm and the distal and proximal margins were set to 0 cm. As is common in all treatment planning systems, the target volume and the geometry (organ definition and delineation) is the input initially given by the user. The beam energy and the fluence weighting is calculated by the algorithm in order to meet the criteria set by the user. The user can make changes to the fluence weighting scheme after evaluating the initial dose distribution proposed by the algorithm.

In the clinical routine the goal is to create treatment plans with an acceptable dose coverage of the target volume, and at the same time keep the dose to the surrounding organs on an as low as possible level and according to the latest recommendations. A typical measure for the homogeneity of the dose in the target volume is the maximum and minimum dose in the target, and the fraction of the target that receives 100% dose. A "good" coverage can for instance be when the dose in target (PTV) lies between 95% and 105% of the prescribed dose. One should note that the purpose of this work is not to make clinically optimized treatment plans, but to investigate how the treatment planning system calculate the dose when introduced to various materials blocking the treatment volume (PTV). In table 5.4 the parameters modulation width, minimum energy and maximum energy from the Eclipse set-up is presented. Note that the target volume, a cube of $5 \times 5 \times 5$ cm^3 located at and from 10 cm depth, is the same for all the treatment plans.

After defining the target volume and setting the margins as mentioned above, the dose was calculated.

Table 5.4: Eclipse values

Fhantom	*SOBP width*	*Minimum energy*	*Maximum energy*
Homogeneous water phantom	5.09 cm	116.3 MeV	146.7 MeV
Bone volume, symmetric case	5.83 cm	120.2 MeV	151.7 MeV
Air volume, symmetric case	6.04 cm	113.2 MeV	143.8 MeV
Aluminium volume, symmetric case	6.51 cm	127.0 MeV	155.5 MeV
Bone volume, asymmetric case	5.77 cm	119.9 MeV	151.4 MeV
Air volume, asymmetric case	6.55 cm	109.6 MeV	147.2 MeV
Aluminium volume, asymmetric case	6.62 cm	120.3 MeV	156.3 MeV

5.3.3 Simulation Set-up in FLUKA

In order to create the treatment plans in FLUKA, the SOBP energy distribution had to be implemented in the source.f user routine. In addition, several

beam adjustments were done in order to make the FLUKA beam resemble an as realistic treatment beam as the beam modelled in Eclipse. This includes a Gaussian spread in both lateral position and in energy, which will add a certain spread or "blurriness" the dose deposition. Table 5.5 summarizes the modulation width, minimum energy and maximum energy applied in the treatment plans created in FLUKA.

Table 5.5: FLUKA values

Fhantom	*SOBP width*	*Minimum energy*	*Maximum energy*
Homogeneous water phantom	5.0 cm	116.2 MeV	146.5 MeV
Bone volume, symmetric case	5.0 cm	121.4 MeV	150.9 MeV
Air volume, symmetric case	5.0 cm	109.5 MeV	140.9 MeV
Aluminium volume, symmetric case	5.0 cm	122.7 MeV	152.0 MeV
Bone volume, asymmetric case	5.0 cm	116.2 MeV	150.9 MeV
Air volume, asymmetric case	5.0 cm	109.6 MeV	146.5 MeV
Aluminium volume, asymmetric case	5.0 cm	116.2 MeV	152.0 MeV

In the source.f user routine the spread in energy and lateral position is given with the Gaussian distributed parameters `RGAUSS, RGAUS1, RGAUS2`. The first gives a spread of energy with $\sigma = 0.008$, and `RGAUS1` and `RGAUS2` gives a lateral Gaussian distribution with $\sigma = 0.37\ cm$.

```
* Kinetic energy of the particle (GeV)
      CALL FLNRRN(RGAUSS)
      TKEFLK (NPFLKA) = ENERGY*(1+0.008D0*RGAUSS)
*  Particle coordinates
* To get a lateral dose profile with a gaussian blurryness at the edges
      CALL FLNRR2(RGAUS1, RGAUS2)
      XFLK (NPFLKA) = (-2.7 + 0.37D0*RGAUS1)+ FLRNDM(DUMMY)*5.4
      YFLK (NPFLKA) = (-2.7 + 0.37D0*RGAUS2)+ FLRNDM(DUMMY)*5.4
      ZFLK (NPFLKA) = -1.0
```

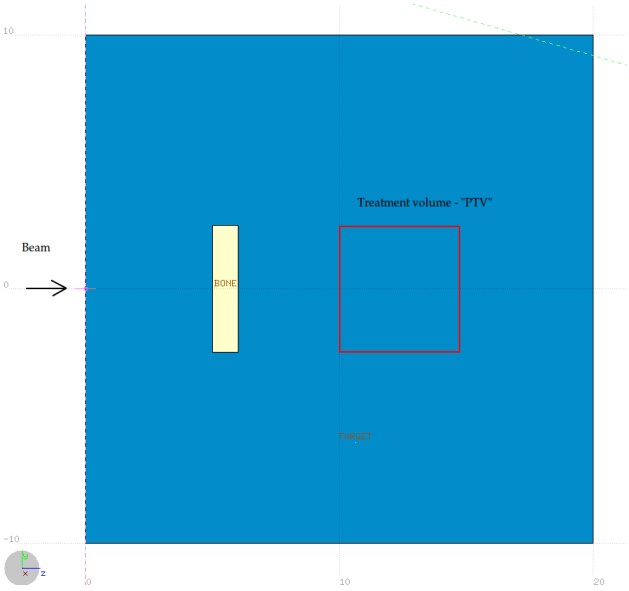

(a) The FLUKA phantom geometry.

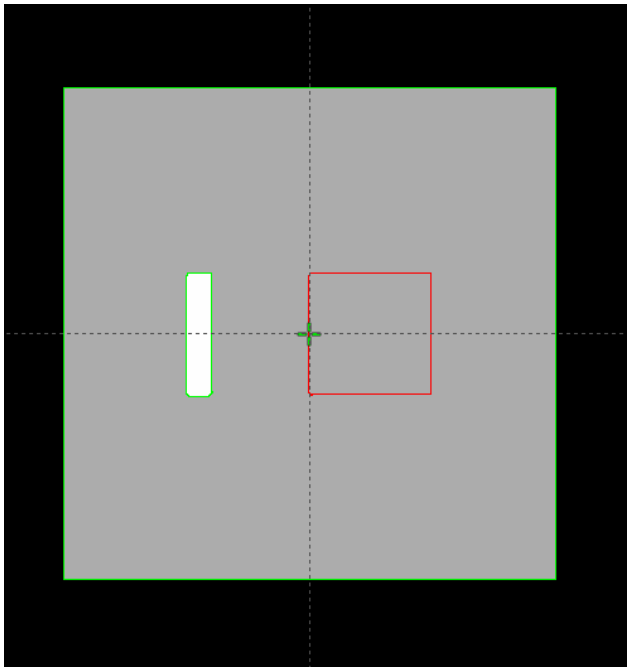

(b) The Eclipse phantom geometry.

Figure 5.18: Phantom design, the symmetric case. The volume of different materials is located at 5 cm depth. In image a) the FLUKA geometry is illustrated while in image b) the Eclipse geometry is illustrated. The phantoms were designed independently in both systems, but the dimensions and densities are similar in both systems.

5.3.4 Results

The following sections will focus on the results from the final part of the project; creating and comparing treatment plans with the Eclipse Proton Planning software and with the FLUKA Monte Carlo code. The properties displayed and compared are the dose profile in depth (longitudinal), and the dose profile in the lateral direction. In addition the 2D dose deposition in color wash will display and give an impression about how the two methods handle the various materials and material positions implemented to the phantoms.

One discrepancy between the FLUKA and Eclipse dose profiles that was present in all the treatment plans was the calculated entrance dose. As can be observed in the figures 5.19 through 5.36, the calculated entrance dose is generally slightly higher for the Eclipse calculation than for the FLUKA calculation, especially for the first 2-3 cm. The gap decreases towards the SOBP. This discrepancy was not further investigated, due to time constraints.

The following section will summarize the result from each phantom case.

Symmetric Phantoms

The figures 5.19 to 5.30 illustrate the resulting dose profiles for the phantoms with a symmetric geometry.

Homogeneous water phantom: The figures 5.19 and 5.20 display the dose deposition in the homogeneous water phantom in FLUKA and in Eclipse. As expected, the dose deposition for this phantom set-up is almost identical for the two systems. The SOBP calculated in Eclipse is slightly wider than the SOBP in FLUKA. This is due to how the SOBP has been determined for the two systems. In Eclipse the width is determined by the PTV defined as the target volume. The PTV is 5 cm in width, and Eclipse calculates the energies and weighting needed in order to provide an as good as possible coverage of the target volume. Despite setting the distal and proximal margins to zero, the calculation algorithm still adds the required spots in order to ensure that the PTV is covered in full depth. In FLUKA the energies are calculated from the formulas 5.2, 5.3 and 5.4, not taking into account the clinical purpose of the PTV. In figure 5.21, the energies in the FLUKA dose plan has been adjusted in order to fit the Eclipse dose profile. The result is two dose profiles that are almost identical.

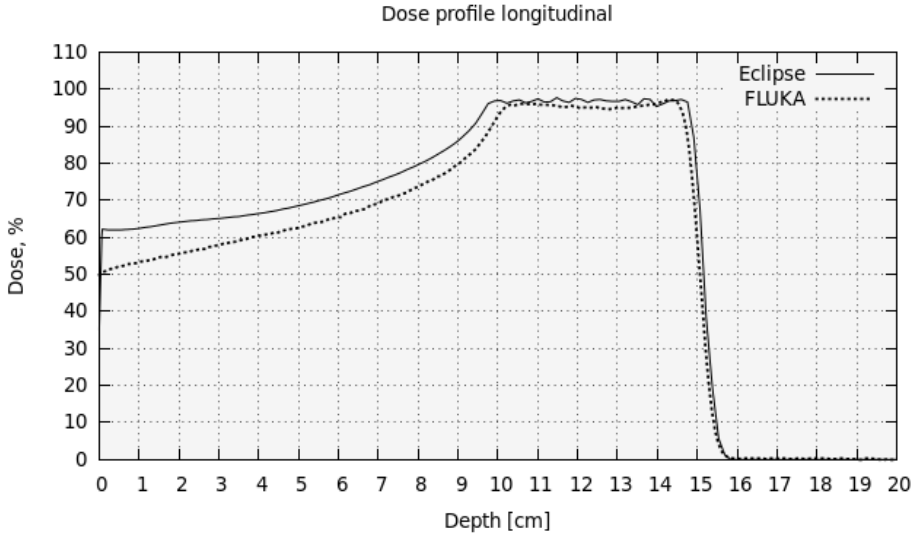

(a) Longitudinal (depth) dose profile from FLUKA and Eclipse.

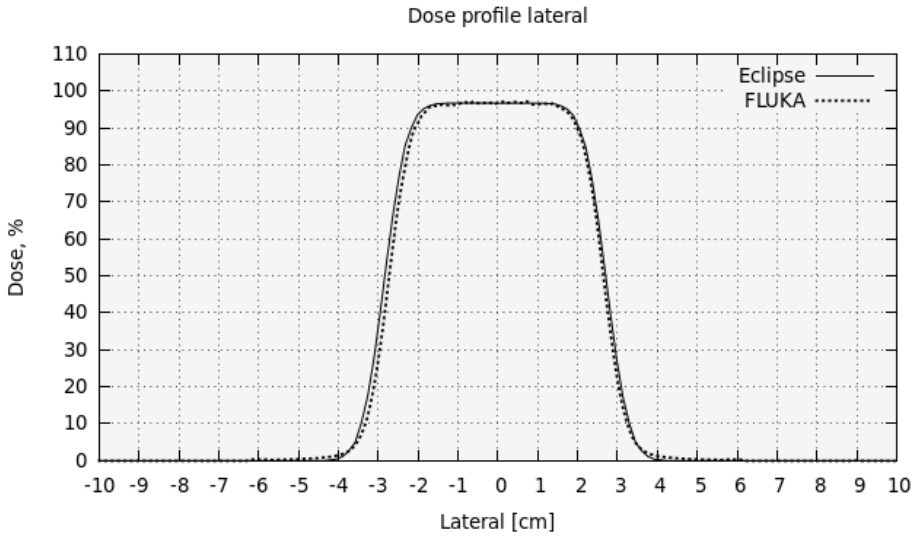

(b) Lateral dose profile from FLUKA and Eclipse.

Figure 5.19: FLUKA Monte Carlo simulation and Eclipse dose calculation. Results from dose prescription and calculation in a homogeneous water phantom. The target volume is located at 10 cm depth. In a) the longitudinal (depth) dose profile is shown and in b) the lateral dose profile is shown.

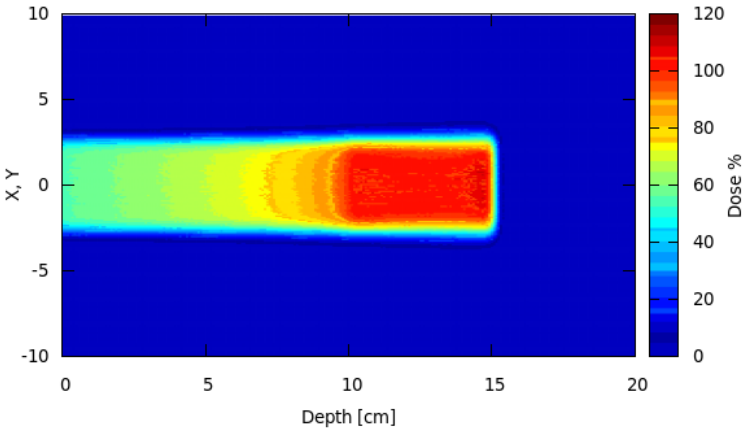

(a) The 2D dose distribution in FLUKA.

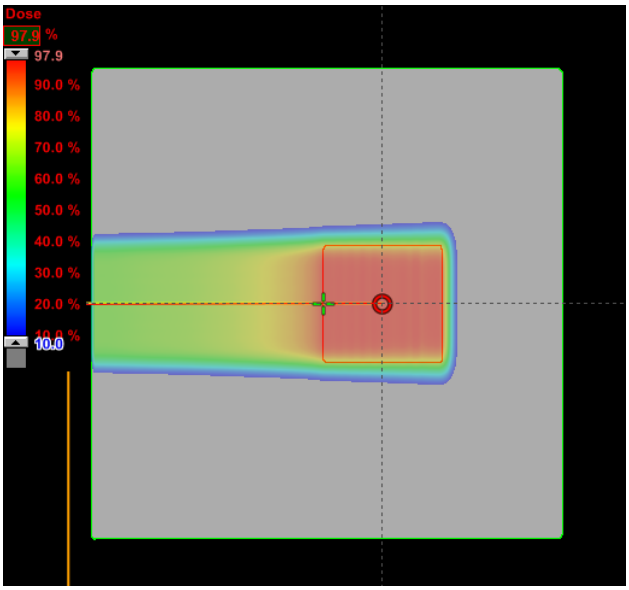

(b) The 2D dose distribution in Eclipse.

Figure 5.20: FLUKA Monte Carlo simulation and Eclipse dose calculation. The 2D dose distribution in the phantom, a) in FLUKA and b) in Eclipse.

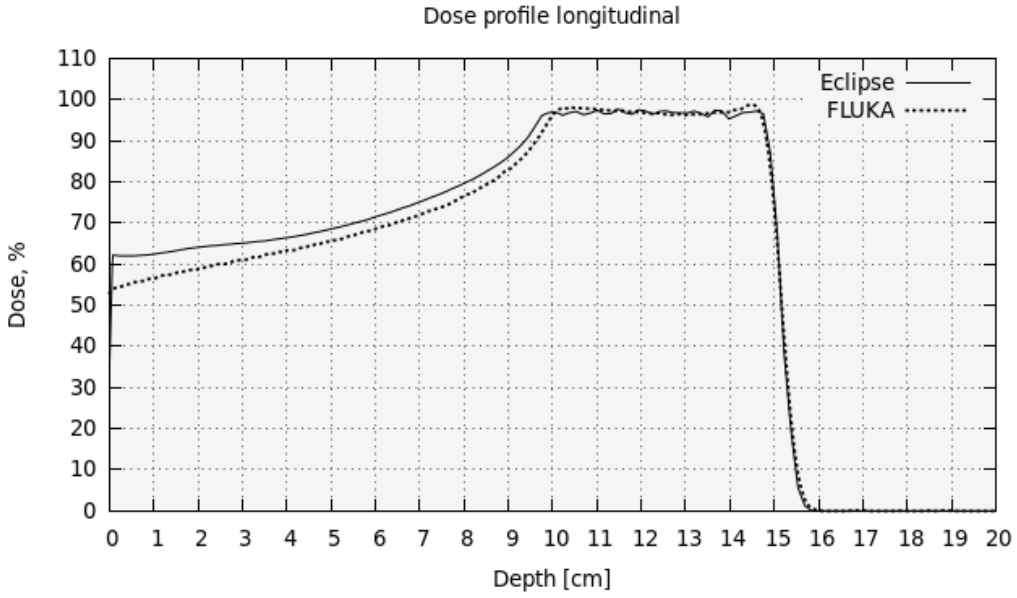

Figure 5.21: FLUKA Monte Carlo simulation and Eclipse dose calculation. Longitudinal dose profiles compared for FLUKA and Eclipse. In this simulation the energies and SOBP width from Eclipse are implemented into the FLUKA source routine, resulting in a dose profile almost identical. The energy distribution ranges from 115.5 MeV to 147.1 MeV.

Symmetric water phantom with bone volume: The figures 5.22 and 5.23 display the dose deposition in the water phantom with a bone volume located at 5 cm depth. The SOBP dose deposition are in good agreement for the two systems, however as with the previous case, Eclipse adds some extra SOBP width. Again a second FLUKA simulation was carried out, mimicking the energies and SOBP width obtained from Eclipse. The resulting dose profile is plotted in figure 5.24. The most striking feature, is the difference between the two calculations appearing at the depth of the bone volume. The FLUKA dose curve experience a discrepancy at the location of the bone, both with respect to dose level, which decrease about 5 % in the bone, and to the slope of the dose curve. On the other hand, the Eclipse dose curve only displays an increased slope at the same point. The reason for this is the different approach to interpretation of the geometry in the two systems. The Eclipse geometry has the Hounsfield Unit with a corresponding proton stopping power for the bone volume to calculate from, while FLUKA has the full elemental composition and the physical properties of the bone volume available. This difference in dose calculation will be further addressed in

section 5.3.5.

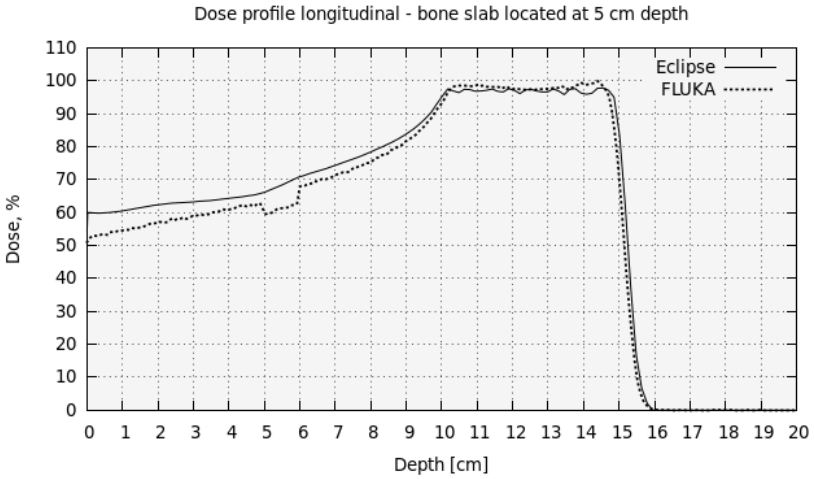

(a) Longitudinal (depth) dose profile.

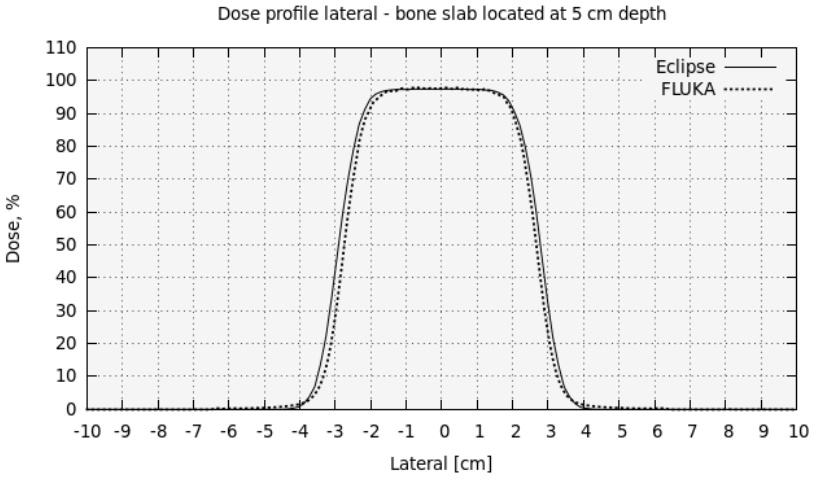

(b) Lateral dose profile.

Figure 5.22: FLUKA Monte Carlo simulation and Eclipse dose calculation. Dose profiles in the water phantom with a volume of bone located at 5 cm depth. a) Longitudinal (depth) dose profile and b) lateral dose profile.

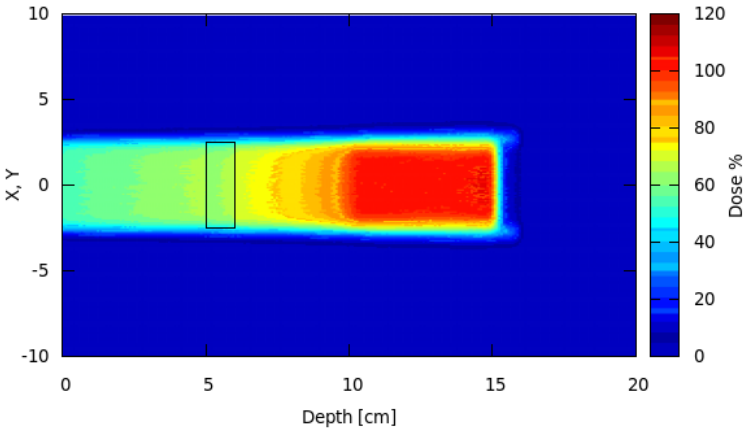

(a) The 2D dose distribution in FLUKA.

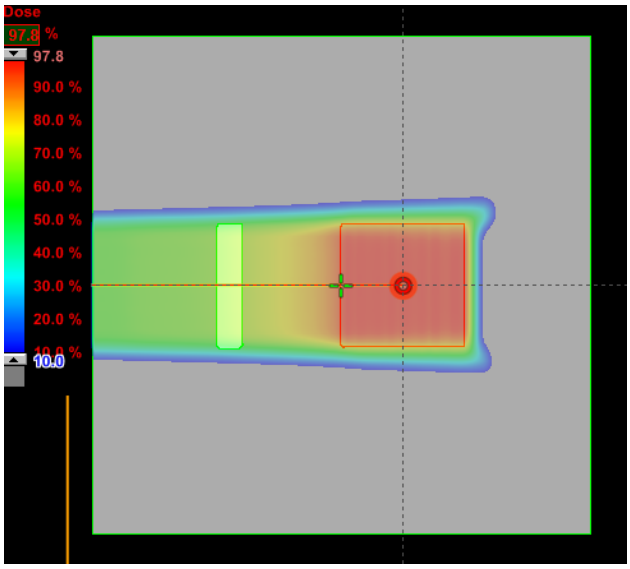

(b) The 2D dose distribution in Eclipse.

Figure 5.23: FLUKA Monte Carlo simulation and Eclipse dose calculation. The 2D dose distribution in the phantom with a volume of bone located at 5 cm depth, a) in FLUKA and b) in Eclipse.

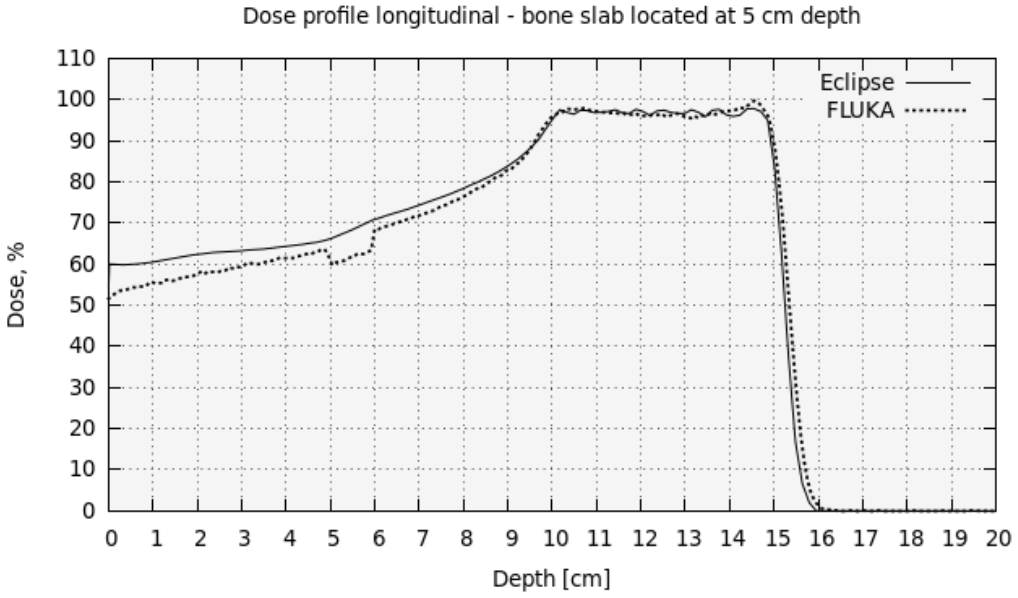

Figure 5.24: FLUKA Monte Carlo simulation and Eclipse dose calculation. Longitudinal dose profiles compared for FLUKA and Eclipse in the water phantom with a volume of bone located at 5 cm depth. In this simulation the energies and SOBP width from Eclipse are implemented into the FLUKA source routine, resulting in an almost identical SOBP. The energy distribution ranges from 117.5 MeV to 152.0 MeV.

Symmetric water phantom with a volume of air: The figures 5.25 and 5.26 display the dose deposition in the water phantom with a volume of air located at 5 cm depth. For this case Eclipse adds an additional 1.0 cm to the SOBP, which is visible in the distal part of the target. In figure 5.27, the energies and SOBP width from Eclipse is implemented in the FLUKA source code, leading to a good agreement between FLUKA and Eclipse concerning the proximal and distal edge of the SOBP. As in the previous case, the FLUKA dose curve experience a discrepancy at the location of the air volume. The slope decreases to almost zero, and the dose level drops about 15 % in the air volume. At the same time the Eclipse dose curve experience the same decrease in slope, but not the change in dose level. This phenomena are further addressed in section 5.3.5.

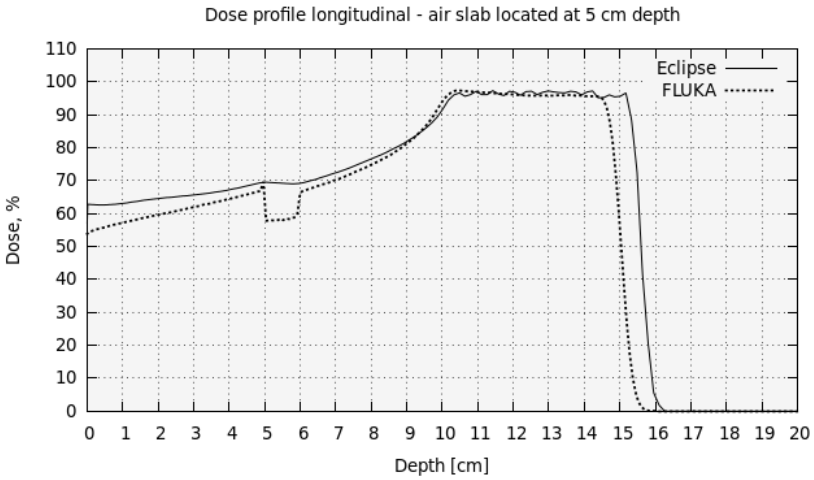

(a) Longitudinal (depth) dose profile.

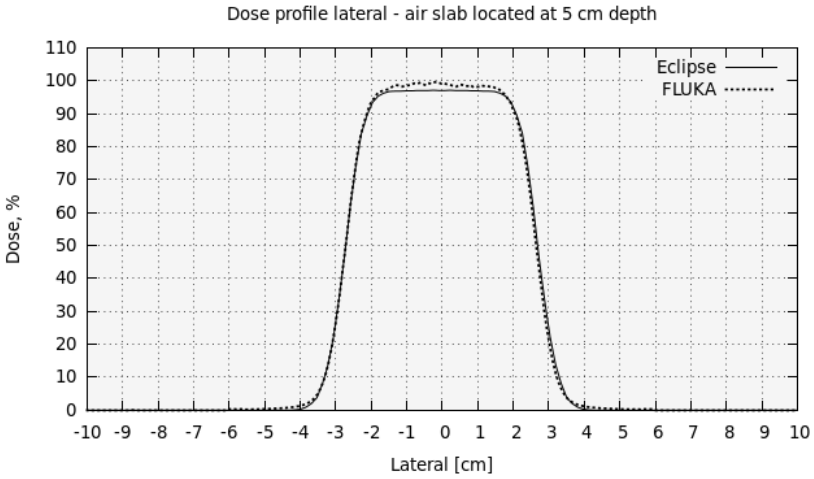

(b) Lateral dose profile.

Figure 5.25: FLUKA Monte Carlo simulation and Eclipse dose calculation. Dose profiles in the water phantom with a volume of air located at 5 cm depth. Image a) shows the longitudinal (depth) dose profile and b) the lateral dose profile.

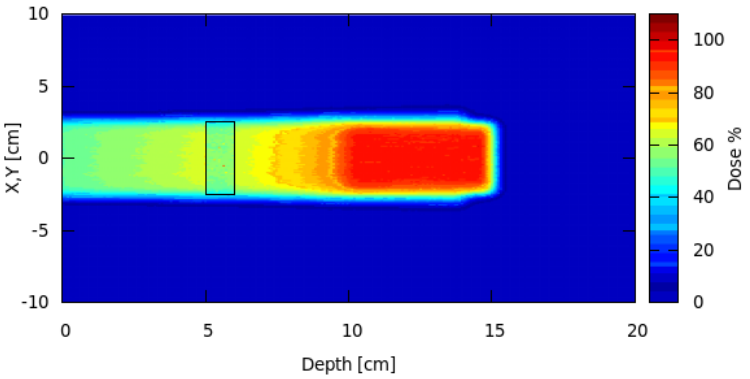

(a) The 2D dose distribution in FLUKA.

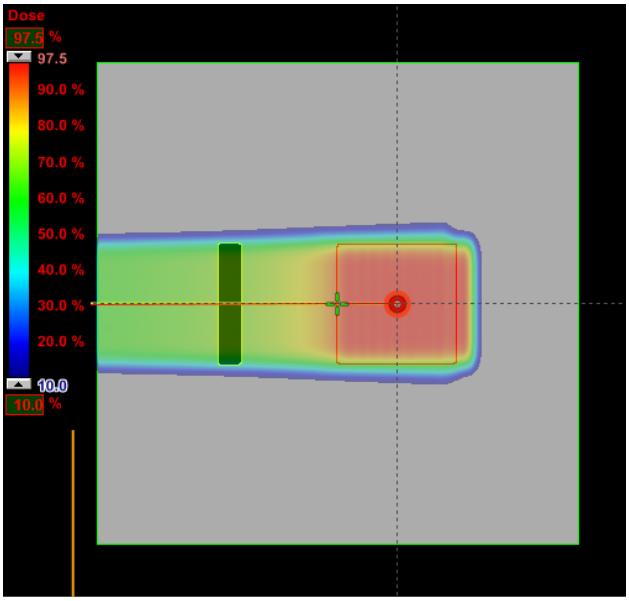

(b) The 2D dose distribution in Eclipse.

Figure 5.26: FLUKA Monte Carlo simulation and Eclipse dose calculation. The 2D dose distribution in the phantom with a volume of air located at 5 cm depth, a) in FLUKA and b) in Eclipse.

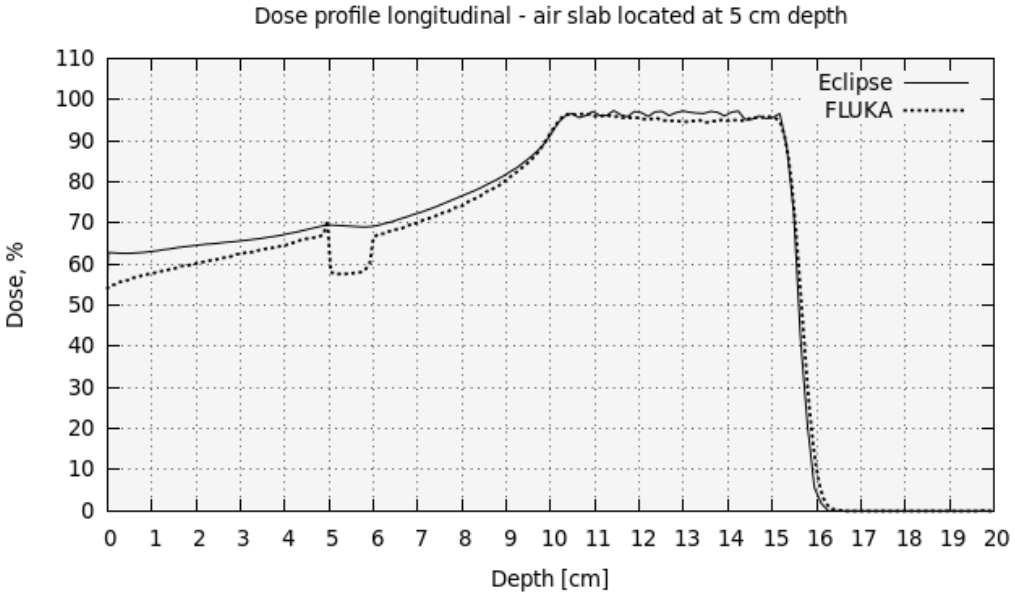

Figure 5.27: FLUKA Monte Carlo simulation and Eclipse dose calculation. Longitudinal dose profile compared for FLUKA and Eclipse in water phantom with a volume of air located at 5 cm depth. In this simulation the energies and SOBP width from Eclipse are implemented into the FLUKA source routine, resulting in an almost identical SOBP. The energy distribution ranges from 110.1 MeV to 144.3 MeV.

Symmetric water phantom with aluminium volume: The figures 5.28 and 5.29 display the dose deposition in the water phantom with an aluminium volume located at 5 cm depth. Eclipse adds an additional 0.5 cm to the SOBP, which is apparent in the distal part of the SOBP. Figure 5.30 shows the longitudinal dose profiles as the input energies in FLUKA is adjusted to match the Eclipse energy distribution. The FLUKA dose curve displays a large deviation at the position of the aluminium, causing a decrease in dose level of about 17 %. And as with the previous cases, the only impact on the Eclipse dose curve is the increase of the slope of the dose curve.

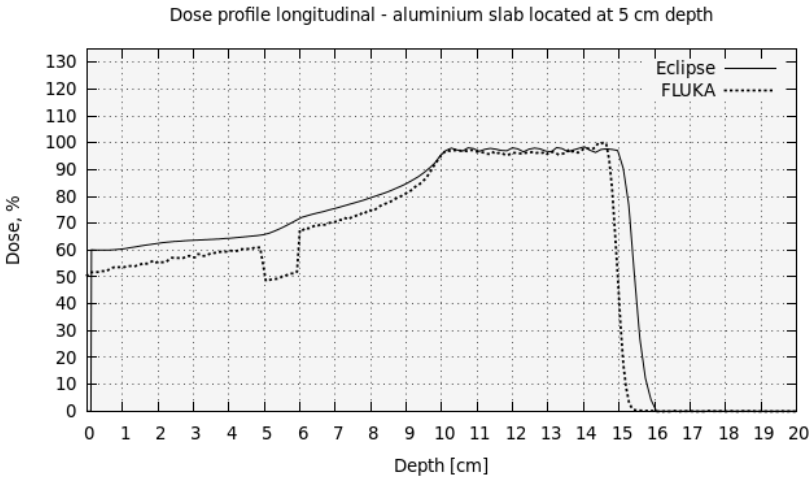

(a) Longitudinal (depth) dose profile.

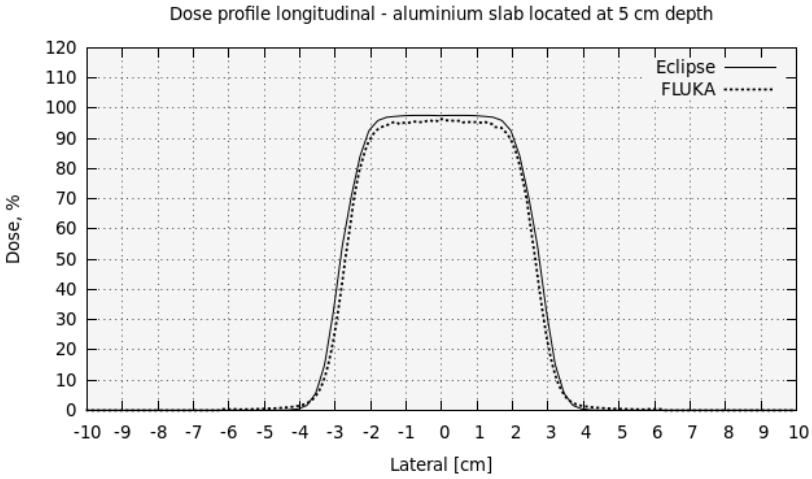

(b) Lateral dose profile.

Figure 5.28: FLUKA Monte Carlo simulation and Eclipse dose calculation. Dose profiles in the water phantom with a volume of aluminium located at 5 cm depth. Image a) shows the longitudinal (depth) dose profile and b) the lateral dose profile.

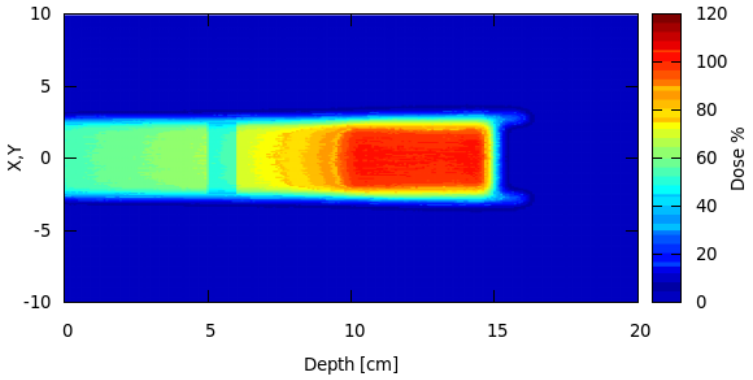

(a) The 2D dose distribution in FLUKA.

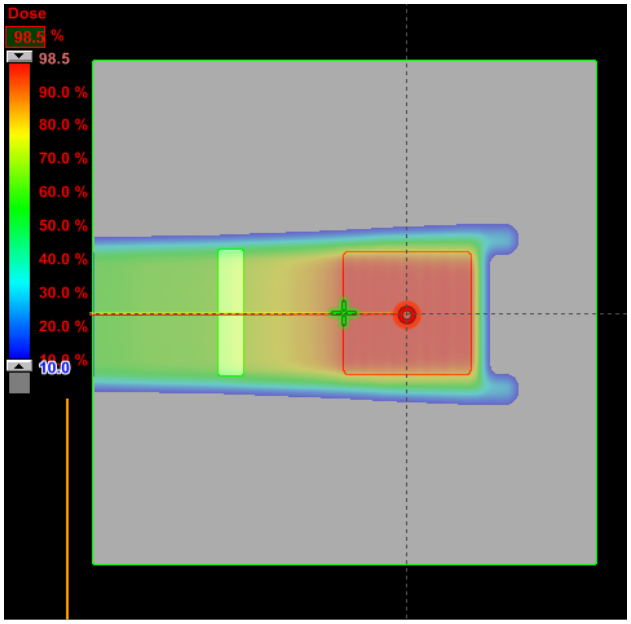

(b) The 2D dose distribution in Eclipse.

Figure 5.29: FLUKA Monte Carlo simulation and Eclipse dose calculation. The 2D dose distribution in the phantom with a volume of aluminium located at 5 cm depth, a) in FLUKA and b) in Eclipse.

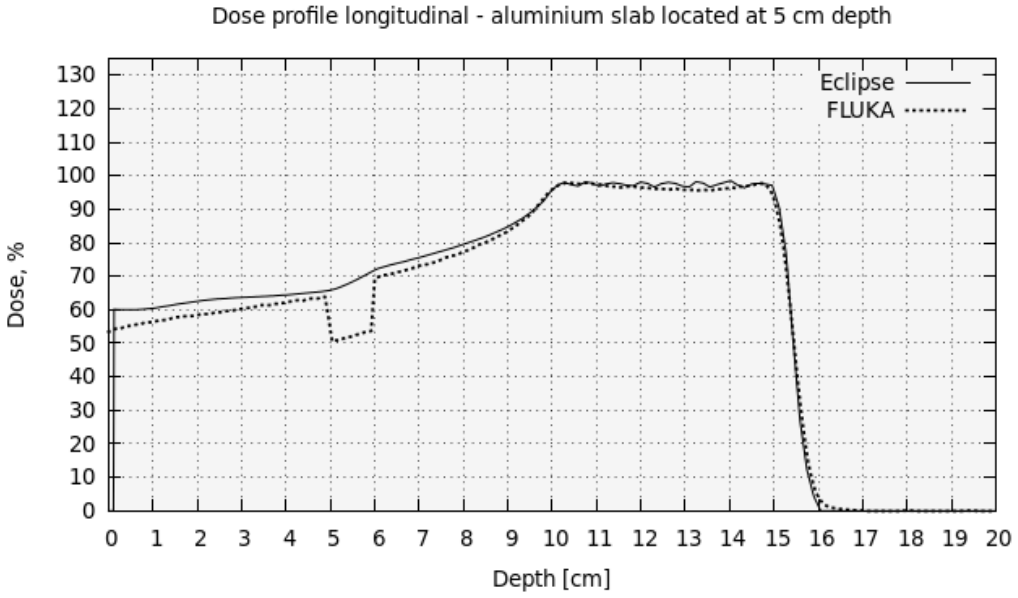

Figure 5.30: FLUKA Monte Carlo simulation and Eclipse dose calculation. Longitudinal dose profiles compared for FLUKA and Eclipse in the water phantom with a volume of aluminium located at 5 cm depth. In this simulation the energies and SOBP width from Eclipse are implemented into the FLUKA source routine, resulting in an almost identical SOBP. The energy distribution ranges from 122.6 MeV to 154.6 MeV.

Asymmetric Phantoms

Figures 5.31 through 5.36 illustrate the resulting dose profiles in the phantoms with an asymmetric geometry. An asymmetric phantom design will illustrate how the dose deposition will be affected as the beam must pass an interface with a high density gradient, orthogonal to the beam direction.

In addition to the discrepancy between FLUKA and Eclipse concerning the dose calculations at the position of the inhomogeneity, there is a difference in how the two models generate the beam distribution assigned to cover the target volume with homogeneous dose. In FLUKA the method used to create this distribution of proton energies were the approach where one half of the phantom (y=[-10:0]) was treated like a homogeneous water phantom, while the other half of the phantom (y=[0:10]) was treated like the phantom with a material volume inserted into the beam path, as described above. Eclipse has a different approach. As can be observed in the 2D dose distribution, the dose distribution in the whole system seems altered by the block of material other than water covering half the entrance area for the beam path leading towards the target volume. The lateral field in Eclipse is generally broader and more asymmetric than in FLUKA, despite the target volume, the $5 \times 5 \times 5\ cm^3$ cube located at 10 cm depth, is constant for all the treatment plans. The details in the calculation algorithm is not available for the Eclipse user, and the algorithm can not be edited by the user. However, Eclipse is a tool created for clinical use and when faced with heterogeneous geometry and sharp density edges the calculation algorithm invokes additional beam spots in order to cover the target volume with dose. In all the simulations there is a slight discrepancy in the position of the SOBP concerning the proximal and the distal edge between FLUKA and Eclipse. As in the case with the symmetrical phantoms presented in the previous section, the energies calculated to produce the SOBP are not identical for the two systems. This discrepancy was addressed in the previous section and will not be elaborated in this section. The characteristics considered regarding the SOBP in this section are the shape of the SOBP and the slope and sharpness of the distal dose falloff.

Asymmetric water phantom with bone volume: Figures 5.31 and 5.32 display the longitudinal, lateral and 2D dose distribution calculated with FLUKA and Eclipse. The SOBP dose plateau from both programs follow the same shape, this is the case also for the shape of the distal falloff. The lateral dose profile differs by 1.0 cm at the side with the bone volume. Like in the previous examples, the FLUKA and Eclipse algorithms approach the dose calculation differently. The FLUKA routine distributes the dose without any clinical considerations towards the volume. Being a system developed for clinical use, Eclipse adds beam spot to the lateral edges in order to fully cover the target volume, hence a broader lateral distribution will appear.

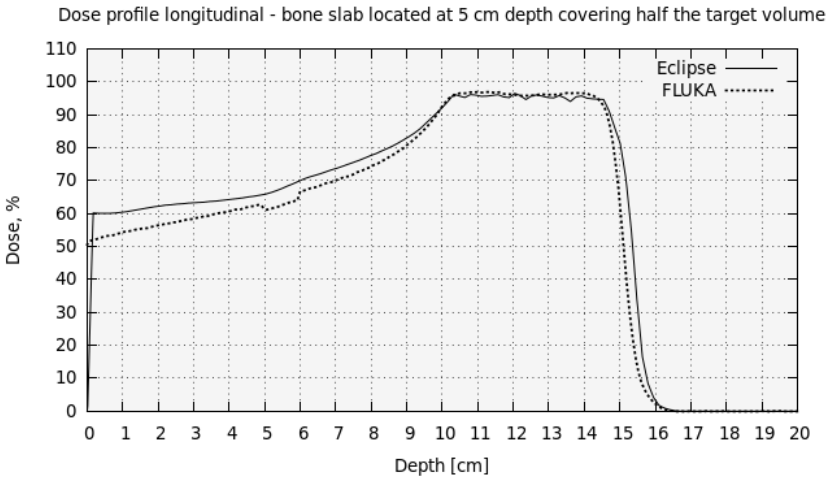

(a) Longitudinal (depth) dose profile.

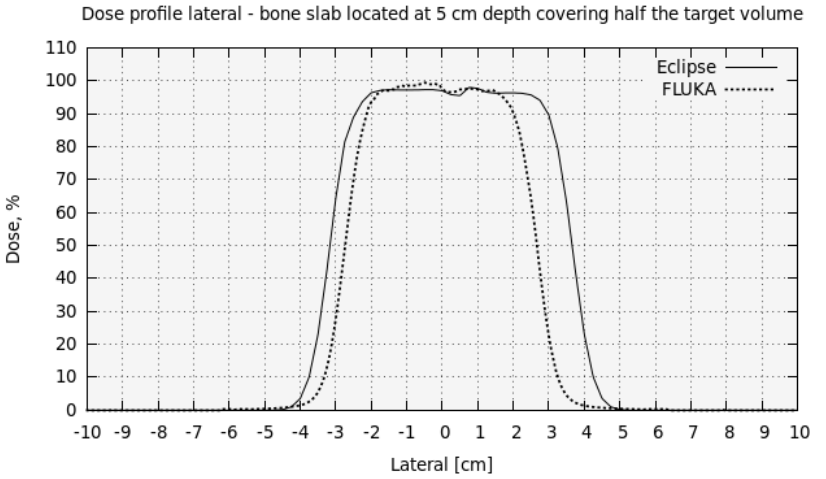

(b) Lateral dose profile.

Figure 5.31: FLUKA Monte Carlo simulation and Eclipse dose calculation. Dose profiles in the water phantom with a volume of bone located at 5 cm depth, thus blocking half the target volume as seen in the beam's eye view. The figure displays a) the longitudinal (depth) dose profile and b) the lateral dose profile, averaged at the centre of the PTV (at 12.5 cm depth).

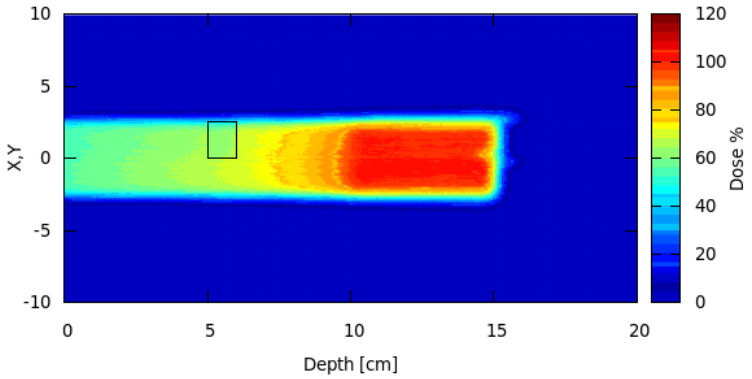

(a) The 2D dose distribution in FLUKA.

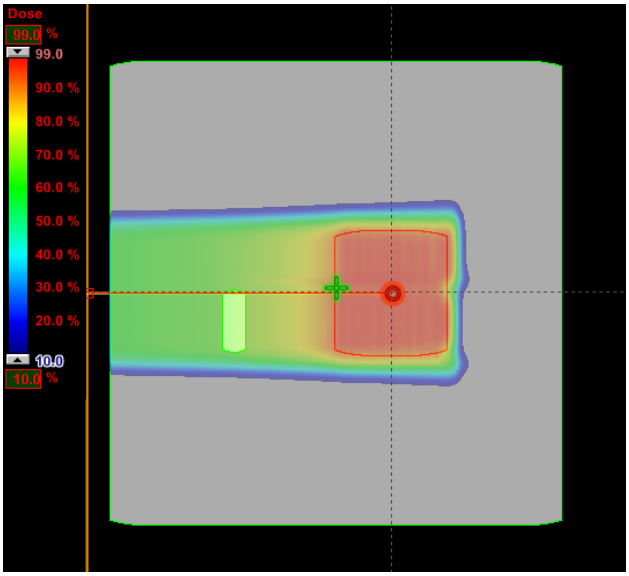

(b) The 2D dose distribution in Eclipse.

Figure 5.32: FLUKA Monte Carlo simulation and Eclipse dose calculation. The 2D dose distribution in a water phantom with a volume of bone located at 5 cm depth, thus blocking half the target volume as seen in the beam's eye view. The figure displays the 2D dose distribution a) in FLUKA and b) in Eclipse.

Asymmetric water phantom with air volume: Figures 5.33 and 5.34 display the longitudinal, lateral and 2D dose distribution calculated with FLUKA and Eclipse. Air can be challenging for dose planning of a proton beam. A beam will deposit very little energy in air, but beam scattering and the corresponding beam divergence can be significant for a proton beam traversing through air. The SOBP from FLUKA and Eclipse are consistent when compared to each other and the distal dose falloff has the same shape, due to the air disturbance the distal edge is less sharp than the distal shape calculated for a homogeneous water phantom. As with the calculations for homogeneous phantoms, Eclipse adds some width to the SOBP. From the 2D dose distribution one can see that the Eclipse dose distribution in the homogeneous part of the phantom is altered by the volume of air located on the other side. A similar dose disturbance can not be seen in the FLUKA calculated dose deposition. As previously mentioned, the FLUKA beam algorithm treats the homogeneous side like a homogeneous geometry, and the inhomogeneous side like an inhomogeneous geometry, ie the beam assigned to cover the target at one lateral edge is not influenced by the geometry at the other lateral edge, 5 cm away.

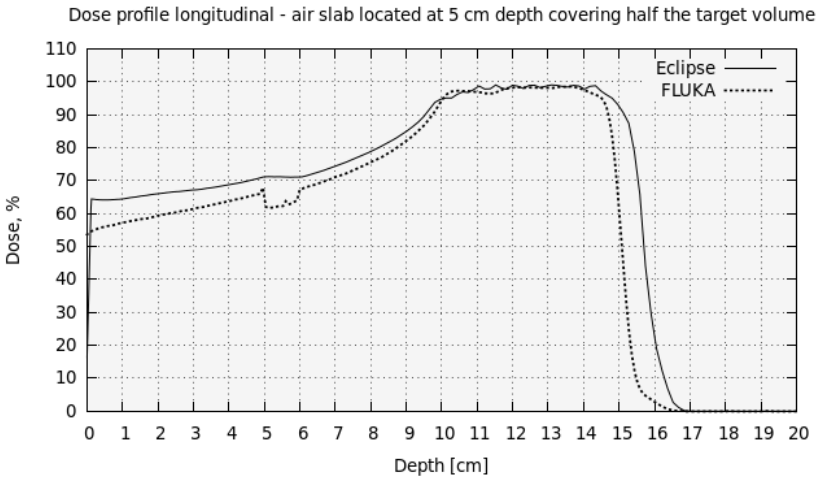

(a) Longitudinal (depth) dose profile.

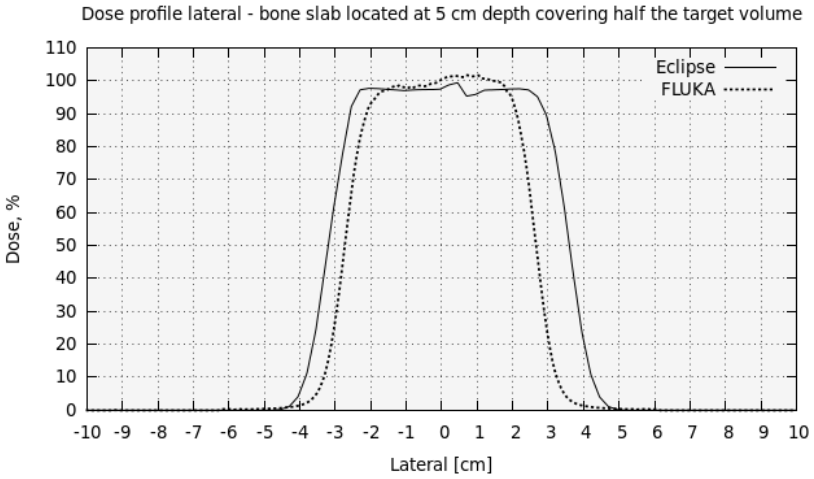

(b) Lateral dose profile.

Figure 5.33: FLUKA Monte Carlo simulation and Eclipse dose calculation. Dose profiles in the water phantom with a volume of air located at 5 cm depth, thus blocking half the target volume as seen in beam's eye view. The figure displays a) the longitudinal (depth) dose profile and b) the lateral dose profile.

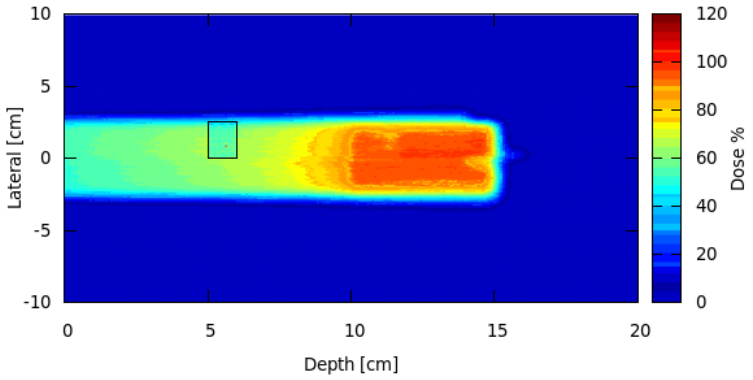

(a) The 2D dose distribution in FLUKA.

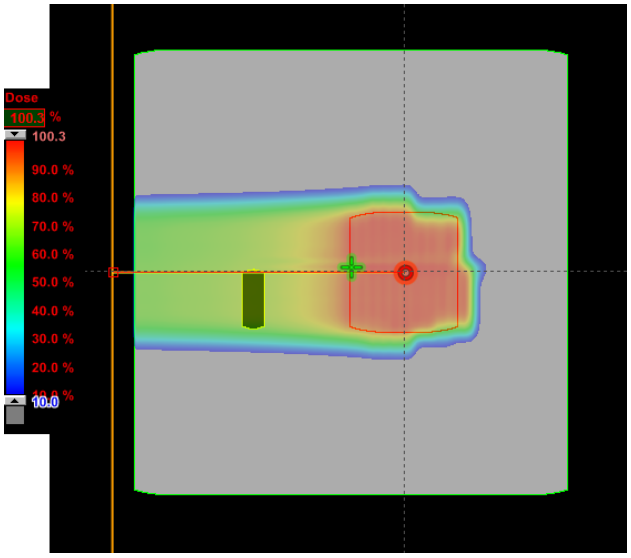

(b) The 2D dose distribution in Eclipse.

Figure 5.34: FLUKA Monte Carlo simulation and Eclipse dose calculation. 2D dose distribution in the phantom with a volume of air located at 5 cm depth, thus blocking half the target volume as seen in the beam's eye view. The figure displays the dose distribution a) in FLUKA and b) in Eclipse.

Asymmetric water phantom with an aluminium volume: Figures 5.35 and 5.36 display the longitudinal, lateral and 2D dose distribution calculated with FLUKA and Eclipse. The dose profiles from the asymmetric phantom with aluminium covering half the treatment field, is consistent in FLUKA and Eclipse, both regarding SOBP, lateral dose profile and 2D dose distribution. Some discrepancy between the two methods is visible in the SOBP. However this is due to where the dose profile is plotted in the geometry. For all the treatment plans, the center of the treatment volume has been the standard position for the average dose output. The inconsistency can be caused by the deviation between the Eclipse versus FLUKA geometry design. When creating volumes in FLUKA, the exact coordinates are assigned by the user. The exact coordinates are not available as input numbers when creating volumes in Eclipse due to the limited resolution of the geometry. This can lead to a slight variation in the eclipse geometry compared to FLUKA, in the order of 1-2 mm.

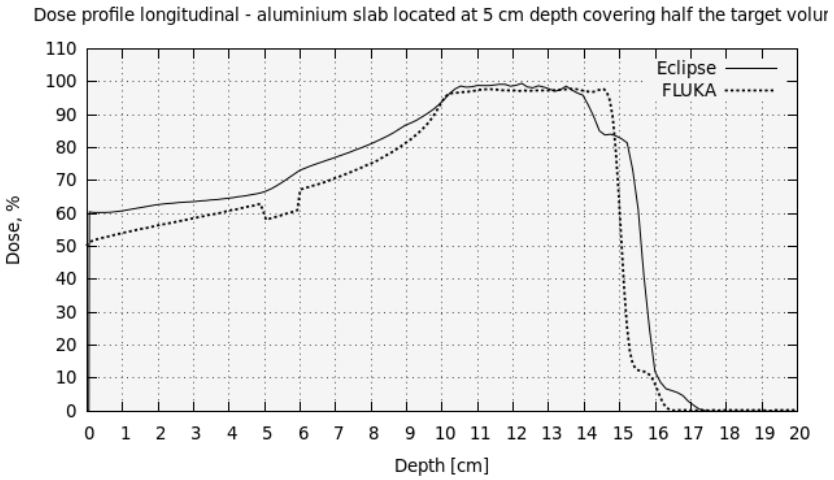

(a) The longitudinal (depth) dose profile.

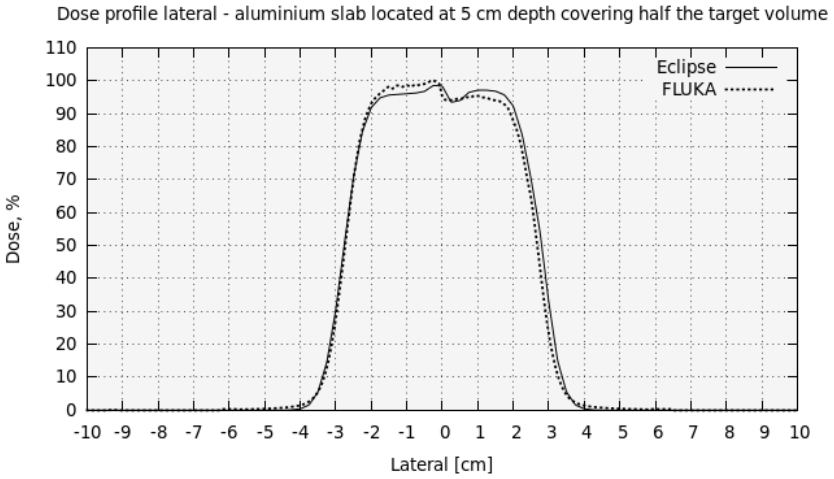

(b) Lateral dose profile.

Figure 5.35: FLUKA Monte Carlo simulation and Eclipse dose calculation. Dose profiles in the water phantom with a volume of aluminium located at 5 cm depth, thus blocking half the target volume as seen in the beam's eye view. The figure displays a) the longitudinal (depth) dose profile and b) the lateral dose profile.

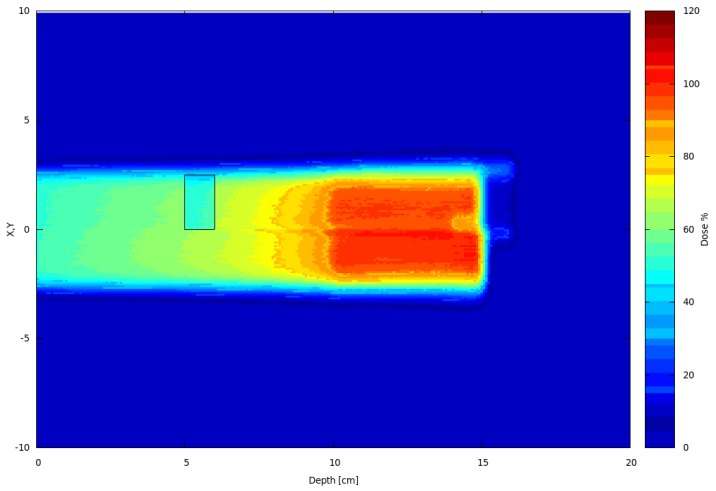

(a) The 2D dose distribution in FLUKA.

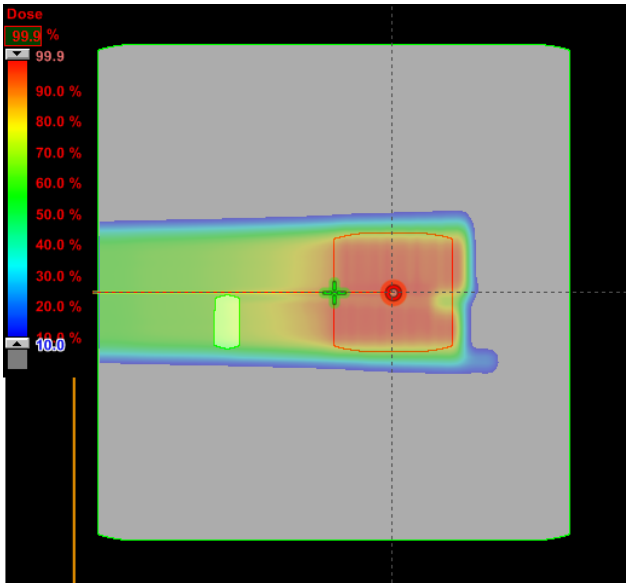

(b) The 2D dose distribution in Eclipse.

Figure 5.36: FLUKA Monte Carlo simulation and Eclipse dose calculation. 2D dose distribution in the phantom with a volume of aluminium located at 5 cm depth, thus blocking half the target volume as seen in the beam's eye view. The figure displays the dose distribution a) in FLUKA and b) in Eclipse.

5.3.5 Calculated Dose and Energy Loss

The Bethe Bloch equation is expressing energy loss by charged particles as they traverse matter. The parameters specific for the absorbing material traversed are density ρ in units of $[\frac{g}{cm^3}]$, the ratio of atomic number and atomic weight $\frac{Z}{A}$, and finally the mean ionization energy I in units of $[eV]$.

Table 5.6: Mean ionization energy for various materials [6]

Material	$I\,[eV]$
Graphite	78
Mg	156
Cu	322
Al	166
Fe	286
Au	790
Pb	823
Si	173
NaI	452
N_2	82
O_2	95
H_2O	75
lucite	74
Air	85.7
BGO	534
Plastic scint.	64.7

From the simulations performed in FLUKA one can see a discontinuity in the depth dose curve at the point where the material volume is located. In the Eclipse calculations these discontinuities are not present. This is partly due to the information available in a microscopic Monte Carlo simulation tool as FLUKA as opposed to Eclipse, which applies simplifications that does not provide or apply the same amount of information into the algorithm.

In FLUKA, the geometry input is of a different kind than the geometry input in Eclipse. When the phantoms were designed in FLUKA, the materials in the geometry have been assigned with elemental composition and tabulated material properties. As a result of this, FLUKA has the information required to solve the Bethe-Bloch equation throughout the geometry. On the other hand, Eclipse has a more limited set of parameters available, and more approximations are applied in order to calculate the dose based on the geometry input. In the clinical routine, a set of slice-by-slice CT scans of

the patient is imported into the treatment planning software, in this instance Eclipse. The proton stopping power is estimated based on these CT numbers, using the stoichiometric method addressed in section 3.5.1. When designing a phantom in Eclipse, the user can create different shapes and assign various materials into the geometry. However, the user assigns only a HU to the material in a phantom geometry, and Eclipse calculates the physical density of the material based on the HU value the user has provided. Two materials with the same physical density but with different elemental composition and mean ionization energy will by this method be treated as identical materials in a phantom created in Eclipse. The algorithm models only water, ie there are no other materials in an Eclipse geometry than water, only the physical density can vary. The CT based HU value is interpreted into stopping power, hence the "water" is scaled by altering the density. The other main parameters affecting energy deposition, for instance the mean ionization energy, will be universally the same for the whole Eclipse geometry [50]. This means that when adding for instance a structure of aluminium into the phantom, one can only apply a Hounsfield number which Eclipse in turn interprets to a physical density. Aluminium has the physical density $\rho = 2.7\ g/cm^3$, which would give a HU value of around +2800. For Eclipse a structure of aluminium will appear to be a volume of very dense water, still with a mean ionization energy of 75 eV [35], as opposed to 166 eV which is the mean ionization energy of aluminium.

To investigate this "water density scaling method" simulations were run in FLUKA with materials of constant density, but with different elemental compositions. In figure 5.37 one can see the resulting depth dose curve of a 150 MeV proton beam hitting a target consisting of; bone, beryllium and epoxy respectively. In the material database in FLUKA these materials are listed with the same physical density, $\rho = 1.85\ g/cm^3$. The material database even contains bone with equal density, but with different mean ionization energy. The result when scoring the dose from a 150 MeV proton beam can be seen in figure 5.38. To investigate how this effect can alter the position of an SOBP, a bone volume of 4 cm was positioned in a water phantom geometry, from 3 cm to 7 cm depth. The result from a simulation on this set-up can be seen in figure 5.39. As can be seen in this figure, the distal falloff is pushed about 2-3 mm deeper, ie about 2 % of the total range, for the bone with the highest mean ionization energy (106.4 eV) compared to the bone with an ionization energy of 91.9 eV. These variations in mean ionization energy will not be possible to identify in a CT image, thus an Eclipse dose calculation based on this CT geometry would give two identical curves.

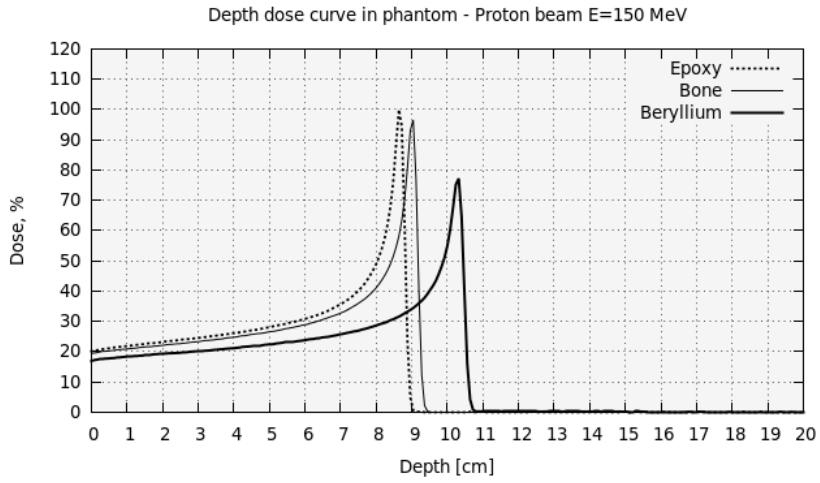

Figure 5.37: FLUKA Monte Carlo simulation. Depth dose profile from a 150 MeV proton beam in 3 different materials; bone, beryllium and epoxy. These materials all have the same density.

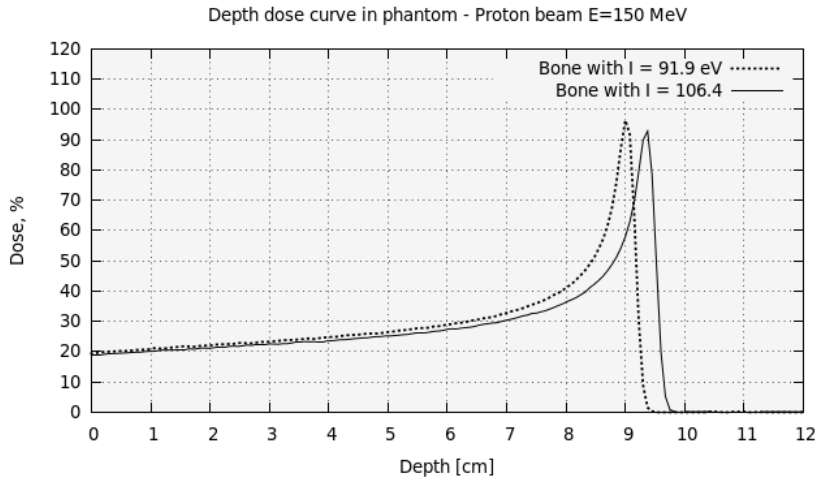

Figure 5.38: FLUKA Monte Carlo simulation. Depth dose profile from a 150 MeV proton beam in 2 different types of bone. The densities for these two types of bone are the same (1.85 g/cm^3), but the elemental composition and mean ionization energy are different. The solid line shows the dose in bone with a mean ionization energy of 106.4 eV, while the dashed line shows the dose in bone with a mean ionization energy of 91.9 eV.

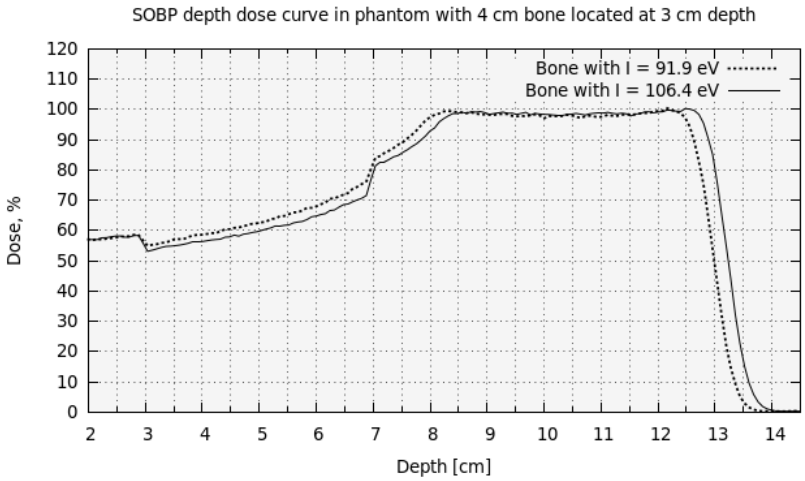

Figure 5.39: FLUKA Monte Carlo simulation. The SOBP with the same energy spectrum and weight distribution impinging on a water phantom with a 4 cm thick volume of bone located at 3 cm depth. As in the previous figure, the density of the bone is similar in both cases, however the mean ionization energy is different.

Chapter 6

Conclusion and outlook

The overall purpose of this project has been to simulate a therapeutic proton beam using the FLUKA Monte Carlo code, and to create proton therapy plans with a clinically optimized proton therapy dose planning software, in order to illustrate the difference in calculated dose using Monte Carlo simulation compared to a commercial treatment planning system, the Varian Eclipse proton planning software.

A spread-out Bragg peak was created with the use of both passive and active energy modulation, based on the formula presented by [49]. In the passive case, an aluminium ridge filter was designed with thickness and widths calculated to produce an SOBP from a 150 MeV proton field. The ridge filter was modelled based on acquired information regarding the stopping power of aluminium and the weighting formula 5.4 required to create an SOBP. The resulting SOBP produced with the ridge filter shows a satisfactory dose profile for this purpose, a confined dose plateau at the desired depth. The scattering of the beam in the ridge filter, and in the air between the filter and the phantom, makes the distal falloff less steep than when no material is present in the beam.
A sharper SOBP was obtained with the use of active energy modulation. Based on the SOBP formulas by [49], a user subroutine was written and linked to the FLUKA input card. The resulting SOBP displayed a flat dose plateau and a sharp distal falloff. In order to make the beam as realistic as possible and representative for a clinical beam, a Gaussian spread in energy and lateral position was implemented, making the distal dose falloff and the lateral spread appear in good agreement with the Eclipse calculation for dose deposited in a homogeneous water phantom. With the active method, the beam can be programmed to be modulated in the desired fashion, leading to additional degrees of freedom compared to the passive method, which

provides a more rigid and cumbersome modulation of the dose distribution. An active method, not depending on extensive use of beamline hardware, will be flexible and one can assume that in a clinical regime, an active beam delivery can potentially be adaptive to changes in patient throughout the treatment course.

Seven dose plans were created in FLUKA and in Eclipse. The geometry was a water cube with and without an inhomogeneity made of either bone, air or aluminium. The resulting dose profiles, lateral and in depth were compared, as well as the 2D dose distribution. Dose profiles calculated for the phantoms containing a volume of material displayed some discrepancies between FLUKA and Eclipse. In the position of the material volume, the dose profile calculated by FLUKA yielded a change of dose level in the order of 5 % to 15 %, depending on the material, in addition to a change in the slope of the depth dose curve. For the equivalent dose profile calculated by Eclipse, no change in dose level was observed, however the depth dose curve did possess the same change in slope as the dose profile calculated by FLUKA. Due to the fact that the Eclipse algorithm only models water, all other materials are scaled by density enhancement, there is a void with respect to the information required to accurately predict the dose, or to predict the deposited energy in the medium. The largest deviation with reference to the dose distribution in a homogeneous water phantom, occurs when introducing aluminium into the geometry. In Eclipse, the aluminium was represented in a volume of material with a HU of +2800, which will correspond to the physical density for aluminium. Eclipse will interpret this as dense water, and hence an increase of the slope of the dose distribution will occur. In FLUKA, the material will be represented by its density, and in addition the parameters such as the mean ionization energy and atomic number. Hence, FLUKA have all the information necessary to, in a very accurate way, calculate the dose deposition by the proton beam.

The stoichiometric method was developed in order to obtain an improved relation between the CT HU value and the proton stopping power. The principle method is to find the HU of various ICRU standard materials representing human tissue, and calculating the theoretical proton stopping power in these tissues using the Bethe-Bloch equation, and by this find a one-to-one relation between the two entities. One should note that this method is developed for use on human tissues, with densities and mean ionization energies in the same order of magnitude as for water. When introducing non-biological materials such as aluminium, the conversion from CT HU value to stopping power is less accurate. For many clinical situations, metals and alloys are

present in a patient to support or replace bone structures in the body. When prescribing radiation therapy to patients with such implants one should avoid irradiating through such structures.

Future Outlook FLUKA is a versatile tool and there are many challenges that can be addressed, building upon the methods and results from this project:

- In order to isolate the shortcomings of a given dose calculation algorithm, one should apply the exact same geometry and beam set-up in both the treatment planning system, and in the Monte Carlo module, thus importing CT DICOM files into the FLUKA geometry.
- The beamline components will affect the beam entering the patient. A realistic model of the beamline materials, geometry and dimensions would provide additional information about the resulting dose profile.
- In order to create treatment plans in FLUKA that to an even larger degree is mimicking the clinical beam, magnetic fields could be modelled into the beam source.
- The effect of target movement.
- Other particles than protons and carbons, for instance helium- or lithium-ions, should be studied.
- Quantitative studies of production of secondary particles, for instance neutrons, for various modalities.

In addition to challenges addressed with the use of FLUKA, there are numerous topics to study within the field of clinical dose planning. A comparison between different commercial dose planning software on the market should be studied, with the Monte Carlo simulations as a validation tool.

Bibliography

[1] International Agency for Research on Cancer. Globocan 2008, 2010.

[2] Levernes Sverre. Stråleterapi i norge - generelle trender 2001-2010.strålevernrapport 2012:7. Technical report, Statens Strålevern, 2012.

[3] Helse Vest, Helse Sør-Øst, Helse Midt-Norge, Helse Nord, and Helsedirektoratet. Planlegging av norsk senter for partikkelterapi. Technical report, Helsedirektoratet, 2013.

[4] Santosh Yajnik. *Proton Beam Therapy - How Protons are Revolutionizing Cancer Treatment*. Springer New York, 2013.

[5] Robert R. Wilson. Radiological use of fast protons. Technical report, Research Laboratory of Physics, Harvard University Cambridge, 1946.

[6] W. R. Leo. *Techniques for Nuclear and Particle Physics Experiments*. Springer-Verlag, 1994.

[7] Gopal B Saha Ph.D. *Physics and Radiobiology of Nuclear Medicine*. Springer New York, 2013.

[8] Martin J Butson, Peter K.N Yu, Tsang Cheung, and Peter Metcalfe. Radiochromic film for medical radiation dosimetry. *Material Science and Engineering*, 2003.

[9] Center for X-ray Optics and Advanced Light Source. X-ray data booklet. Lawrence Berkeley National Laboratory, October 2009.

[10] Jean Pouliot, Ali Bani-Hashemi, Josephine Chen, Michelle Svatos, Farhad Ghelmansarai, Matthias Mitschke, Michele Aubin, Ping Xia, Olivier Morin, Kara Bucci, Mack Roach, Paco Hernandez, Zirao Zheng, Dimitre Hristov, and Lynn Verhey. Low-dose megavoltage cone-beam ct for radiation therapy. *International Journal of Radiation Oncology*Biology*Physics*, 2005.

[11] Faiz M. Khan. *The Physics of Radiation Therapy, third edition.* Lippincott Williams and Wilkins, 530 Walnut Street, Philadelphia, PA 19106 USA, 2003.

[12] Kristian Ytre-Hauge. Measurements of neutron doses from radiotherapy with ^{12}c ions and photons. Master's thesis, University of Bergen, 2009.

[13] Camilla Hanquist Stokkevåg. Measurements of the photonuclear neutron yield during radiotherapy using bubble detectors and thermoluminescence detectors. Master's thesis, University of Bergen, 2010.

[14] W.-M. et. al. Yao. Review of particle physics. *Journal of Physics G*, 33:1+, 2006.

[15] Harald Paganetti. *Proton Therapy Physics.* CRC Press, Taylor and Francis Group, 2012.

[16] A. Ferrari A. Fasso, J. Ranft, P. R. Sala, G. Battistoni, F. Cerutti, M. Chin, T. Empl, M.V. Garzelli, M. Lantz, A. Mairani, S. Muraro, V. Patera, S. Roesler, G. Smirnov, F. Sommerer, and V. Vlachoudis. *FLUKA-2011 manual.* http://fluka.org, 2011.

[17] IAEA. *Radiation Biology: A Handbook for teachers and Students.* IAEA, 2010.

[18] Paganetti H, Niemierko A, Ancukiewicz M, Gerweck LE, Loeffler JS, Goitein M, and et al. Relative biological effectiveness (rbe) values for proton beam therapy. *International Journal of Radiation Oncology, Biology, Physics*, 2002.

[19] Van der Kogel A. and Joiner M. *Basic Clinical Radiobiology.* A Hodder Arnold Publication, 2009.

[20] Barendsen GW. Responses of cultured cells, tumours and normal tissue to radiation of different linear energy transfer. *Curr Topics Radiat Res Q*, 1968.

[21] ICRP. Icrp publication 72. annals of the icrp 26. Technical report, ICRP, 1996.

[22] Lee W. Goldman. Principles of ct and ct technology. *Journal of Nuclear Medicine Technology*, 2007.

[23] Katia Parodi. *On the feasability of dose quantification with in-beam PET data in radiotherapy with ^{12}C and proton beams.* PhD thesis, University of Dresden, 2004.

[24] David M. Brizel. Pharmacologic approaches to radiation protection. *Journal of Clinical Oncology*, 2007.

[25] Hirohiko Tsujii, Junetsu Mizoe, Tadashi Kamada, Masayuki Baba, Hiroshi Tsuji, Hirotoshi Kato, Shingo Kato, Shigeru Yamada, Shigeo Yasuda, Tatsuya Ohno, Takeshi Yanagi, Reiko Imai, Kenji Kagei, Hiroyuki Kato, Ryusuke Hara, Azusa Hasegawa, Mio Nakajima, Norio Sugane, Noriaki Tamaki, Ryo Takagi, Susumu Kandatsu, Kyosan Yoshikawa, Riwa Kishimoto, and Tadaaki Miyamoto. Clinical results of carbon ion radiotherapy at nirs. *Journal of Radiation Research*, 2007.

[26] Shannon M. MacDonald, Salahuddin Ahmed, Stefanos Kachris, Betty J. Vogds, Melissa DeRouen, Alicia E. Gittleman, Keith DeWyngaert, and Maria T. Vlachaki. Intensity modulated radiation therapy versus three-dimensional conformal radiation therapy for the treatment of high grade glioma: a dosimetric comparison. *Journal of Applied Clinical Medical Physics*, 2007.

[27] Steve Webb. Vmat: its role in radiotherapy. *Physics in Medicine and Biology*, 2009.

[28] Camilla Hanquist Stokkevåg. *Secondary Cancer Risk Estimation in Paediatric Cancer Patients following Radiotherapy.* PhD thesis, University of Bergen, 2013, ongoing work.

[29] Kristian Ytre-Hauge. *Measurements and Monte Carlo Simulations of Neutron Doses from Radiation Therapy with Photons Protons and Carbon Ions.* PhD thesis, University of Bergen, 2013.

[30] Jäkel O. Medical physics aspects of particle therapy. *Radiat Prot Dosimetry*, 2009.

[31] Thomas F. DeLaney, Hanne M. Kooy, Jr., and Anne E. Jacobs. *Proton and Charged Particle Radiotherapy.* Lippincott Williams and Wilkins, 2008.

[32] CNAO Centro Nazionale di Adroterapia Oncologica. Website, 2013.

[33] Helmholtz-Zentrum Berlin (HZB). Picture of range shifter wheel, 2013.

[34] Rinecker Proton Therapy Center. Image of energy modulating wedge, 2013.

[35] *Eclipse Proton Algorithm Reference Guide.*

[36] Marc Marcel. Proton therapy: scattering versus scanning. http://medicalphysicsweb.org/cws/article/opinion/42793, May 2010.

[37] Uwe Schneider, Eros Pedroni, and Antony Lomax. The calibration of ct hounsfield units for radiotherapy treatment planning. *Phys. Med. Biol*, 1996.

[38] Ming Yang, X Ronald Zhu, Peter C Park, Uwe Titt, Radhe Mohan, Gary Virshup, James E Clayton, and Lei Dong. Comprehensive analysis of proton range uncertainties related to patient stopping power ratio estimation using the stoichiometric calibration. *Phys. Med. Biol.*, 2012.

[39] ICRU. 6 treatment planning. *Journal of the ICRU*, pages 95–122, 2007.

[40] Kavita Lalwani, editor. *Development of Proton Computed Tomography (pCT) Detector for Cancer Therapy.* DAE Symp. on Nucl. Phys., 2012.

[41] Vladimir Bashkirov, Reinhard Schulte, George Coutrakon, Bela Erdelyi, Kent Wong, Hartmut Sadrozinski, Scott Penfold, Anatoly Rosenfeld, Scott McAllister, and Keith Schubert. Development of proton computed tomography for applications in proton therapy.

[42] Marco Schwarz. Treatment planning in proton therapy.

[43] D. E. Raeside. Monte carlo principles and applications. *Phys. Med. Biol.*, 1976.

[44] S. Agostinelli et al. Geant4—a simulation toolkit. *Nuclear Instruments and Methods in Physics Research Section A: Accelerators, Spectrometers, Detectors and Associated Equipment*, 506(3):250 – 303, 2003.

[45] Los Alamos National Laboratory. Mcnpx home page, http://mcnpx.lanl.gov/, 2011.

[46] Fippel M, Soukup M., Weber A., and Heufelder J. Implementation of geometry modules into the monte carlo dose calculation algorithm vmcpro to modulate proton beams for the treatment planning of occular tumours. *Biomedizinische Technik*, 2005.

[47] Arthur Guyton. *Textbook of Medical Physiology.* W.B. Saunders, 8th edition, 1991.

[48] Switzerland Paul Scherrer Institute. Psi winter school. Course participation, 2013.

[49] Weimin Chen David Jette. Creating a spread-out bragg peak in proton beams. *Phys. Med. Bio.*, 2011.

[50] Varian Eclipse Team. Proton algorithm. Personal communication.

Appendix A

Patient Statistics from PTCOG

Hadron Therapy Patient Statistics (data recieved from centers per end of March 2013)

Patient Statistics (for the facilities out of operation):

WHERE		PARTICLE	FIRST PATIENT	PATIENT TOTAL	LAST PATIENT	
Belgium	Louvain-la-Neuve	p	1991	21	1993	ocular tumors only
Canada	Vancouver (TRIUMF)	π^-	1979	367	1994	ocular tumors only
Germany	Darmstadt (GSI)	C-ion	1997	440	2009	
Japan	Tsukuba (PMRC, 1)	p	1983	700	2000	
Japan	Chiba	p	1979	145	2002	ocular tumors only
Japan	WERC	p	2002	62	2009	
Russia	Dubna (1)	p	1967	124	1996	
Sweden	Uppsala (1)	p	1957	73	1976	
Switzerland	Villigen PSI (SIN-Piotron)	π^-	1980	503	1993	
Switzerland	Villigen PSI (OPTIS 1)	p	1984	5458	2010	ocular tumors only
CA., USA	Berkeley 184	p	1954	30	1957	
CA., USA	Berkeley	He	1957	2054	1992	
CA., USA	Berkeley	ion	1975	433	1992	
IN., USA	Bloomington (MPRI, 1)	p	1993	34	1999	ocular tumors only
MA., USA	Harvard	p	1961	9116	2002	
NM., USA	Los Alamos	π^-	1974	230	1982	
				19790	**Total**	
			thereof	2054	He	
				1100	pions	
				440	C-ions	
				433	other ions	
				15763	protons	

Patient Statistics (for facilities in operation end of 2012):

WHERE		PARTICLE	FIRST PATIENT	PATIENT TOTAL	DATE OF TOTAL	
Canada	Vancouver (TRIUMF)	p	1995	170	Dec-12	ocular tumors only
Czech Rep.	Prag (PTCCZ)	p	2012	1	Dec-12	
China	Wanjie (WPTC)	p	2004	1078	Dec-12	
China	Lanzhou	C ion	2006	194	Dec-12	
England	Clatterbridge	p	1989	2297	Dec-12	ocular tumors only
France	Nice (CAL)	p	1991	4692	Dec-12	ocular tumors only
France	Orsay (CPO)	p	1991	5949	Dec-12	4748 ocular tumors
Germany	Berlin (HMI)	p	1998	2084	Dec-12	ocular tumors only
Germany	Munich (RPTC)	p	2009	1377	Dec-12	
Germany	HIT, Heidelberg	C ion	2010	980	Dec-12	
Germany	HIT, Heidelberg	p	2010	252	Dec-12	
Italy	Catania (INFN-LNS)	p	2002	293	Nov-12	ocular tumors only
Italy	Pavia (CNAO)	p	2011	42	Dec-12	
Italy	Pavia (CNAO)	C ion	2012	3	Dec-12	
Japan	Chiba (HIMAC)	C ion	1994	7331	Jan-13	72 with scanning
Japan	Kashiwa (NCC)	p	1998	1226	Mar-13	
Japan	Hyogo (HIBMC)	p	2001	3198	Dec-11	
Japan	Hyogo (HIBMC)	C ion	2002	1271	Dec-11	
Japan	Tsukuba (PMRC, 2)	p	2001	2516	Dec-12	
Japan	Shizuoka	p	2003	1365	Dec-12	
Japan	Koriyama-City	p	2008	1812	Dec-12	
Japan	Gunma	C ion	2010	537	Dec-12	
Japan	Ibusuki (MMRI)	p	2011	490	Dec-12	
Korea	Ilsan, Seoul	p	2007	1041	Dec-12	
Poland	Krakow	p	2011	15	Dec-12	ocular tumors only
Russia	Moscow (ITEP)	p	1969	4300	Dec-12	estimated
Russia	St. Petersburg	p	1975	1386	Dec-12	
Russia	Dubna (JINR, 2)	p	1999	922	Dec-12	
South Africa	iThemba LABS	p	1993	521	Dec-11	
Sweden	Uppsala (2)	p	1989	1267	Dec-12	
Switzerland	Villigen-PSI, incl OPTIS2	p	1996	1409	Dec-12	498 ocular tumors
USA, CA.	UCSF - CNL	p	1994	1515	Dec-12	ocular tumors only
USA, CA.	Loma Linda (LLUMC)	p	1990	16884	Dec-12	
USA, IN.	Bloomington (IU Health PTC)	p	2004	1688	Dec-12	
USA, MA.	Boston (NPTC)	p	2001	6550	Oct-12	
USA, TX.	Houston (MD Anderson)	p	2006	3909	Dec-12	
USA, FL	Jacksonville (UFPTI)	p	2006	4272	Dec-12	
USA, OK.	Oklahoma City (ProCure PTC)	p	2009	1045	Dec-12	
USA, PA.	Philadelphia (UPenn)	p	2010	1100	Dec-12	
USA, NY.	New Jersey ProCure PTC)	p	2012	137	Dec-12	
USA, IL.	CDH Warrenville	p	2010	840	Dec-12	
USA, VA.	Hampton (HUPTI)	p	2010	489	Dec-12	
				88448	**Total**	
			thereof	10316	C-ions	
				78132	protons	

Total for all facilities (in operation and out of operation):

2054	He
1100	pions
10756	C-ions
433	other ions
93895	protons
108238	**Grand Total**

Appendix B

FLUKA Script

B.1 Input Card 1

Input for the simulations used to determine the range in the phantom with heterogeneities.

```
TITLE

* Set the defaults for precision simulations
DEFAULTS                                                              HADROTHE
* Define the beam characteristics
BEAM            -0.1                            -0.6      -0.6        PROTON
* Define the beam position
BEAMPOS                               -1.
GEOBEGIN                                                              COMBNAME
    0    0
* Black body
SPH blkbody    0.0 0.0 0.0 100000.0
* Void sphere
SPH void       0.0 0.0 0.0 10000.0
RPP vann       -10. 10. -10. 10. 0.0 20.
RPP bein       -0.5 0.5 -0.5 0.5 5.0 6.0
END
* Black hole
BLKBODY      5 +blkbody -void
* Void around
VOID         5 +void -vann
* Target
TARGET       5 +vann -bein
bein         5 +bein
END
GEOEND
MATERIAL         15. 30.973761      1.82                               PHOSPHO
* Cort. Bone  Ages 2-5
* from: Woodward and White, Brit. J. Radiology, vol. 59, 1216 (1986).
MATERIAL                              1.8                             Cortical
COMPOUND       -20.1   CALCIUM     -10.1   PHOSPHO      -4.0  HYDROGENCortical
COMPOUND       -15.7    CARBON      -4.5  NITROGEN     -45.4    OXYGENCortical
COMPOUND        -0.2  MAGNESIU                                        Cortical
* ..+....1....+....2....+....3....+....4....+....5....+....6....+....7..
ASSIGNMA    BLCKHOLE   BLKBODY
```

```
ASSIGNMA          AIR      VOID
ASSIGNMA        WATER    TARGET
ASSIGNMA    Cortical      bein
USRBIN           10.      DOSE      -41.       12.       12.       22.Dose
USRBIN          -12.      -12.       -2.      250.      250.      250. &
* Set the random number seed
RANDOMIZ         1.0
* Set the number of primary histories to be simulated in the run
START         10000.
STOP
```

B.2 Surce.f code to produce SOBP

```
*$ CREATE SOURCE.FOR
*COPY SOURCE
*
*=== source ===========================================================*
*
      SUBROUTINE SOURCE ( NOMORE )

      INCLUDE '(DBLPRC)'
      INCLUDE '(DIMPAR)'
      INCLUDE '(IOUNIT)'
*----------------------------------------------------------------------*
*
*
      DIMENSION CUMPR(0:51), ENEDGE(52)
*----------------------------------------------------------------------*
*
      INCLUDE '(BEAMCM)'
      INCLUDE '(CASLIM)'
      INCLUDE '(FHEAVY)'
      INCLUDE '(FLKSTK)'
      INCLUDE '(IOIOCM)'
      INCLUDE '(LTCLCM)'
      INCLUDE '(PAPROP)'
      INCLUDE '(SOURCM)'
      INCLUDE '(SUMCOU)'
*
      LOGICAL LFIRST
      SAVE LFIRST
      DATA LFIRST / .TRUE. /
*----------------------------------------------------------------------*
*   Proton energy group boundaries
      DATA ENEDGE /
     & 116.5273483522E-03,
     & 116.8572207934E-03,
     & 117.511318736E-03,
     & 118.1626328485E-03,
     & 118.8112018355E-03,
     & 119.4570634973E-03,
     & 120.1002547594E-03,
     & 120.7408117005E-03,
     & 121.3787695801E-03,
     & 122.0141628644E-03,
     & 122.6470252507E-03,
     & 123.2773896923E-03,
     & 123.9052884206E-03,
```

```
     & 124.5307529678E-03,
     & 125.1538141879E-03,
     & 125.7745022769E-03,
     & 126.3928467928E-03,
     & 127.0088766743E-03,
     & 127.6226202587E-03,
     & 128.2341052997E-03,
     & 128.8433589843E-03,
     & 129.4504079485E-03,
     & 130.0552782933E-03,
     & 130.6579955999E-03,
     & 131.2585849436E-03,
     & 131.8570709084E-03,
     & 132.4534776E-03,
     & 133.0478286592E-03,
     & 133.6401472743E-03,
     & 134.230456193E-03,
     & 134.8187777345E-03,
     & 135.4051338006E-03,
     & 135.9895458867E-03,
     & 136.5720350922E-03,
     & 137.1526221309E-03,
     & 137.7313273407E-03,
     & 138.3081706934E-03,
     & 138.8831718036E-03,
     & 139.456349938E-03,
     & 140.0277240236E-03,
     & 140.5973126567E-03,
     & 141.1651341103E-03,
     & 141.7312063425E-03,
     & 142.295547004E-03,
     & 142.8581734451E-03,
     & 143.4191027234E-03,
     & 143.9783516104E-03,
     & 144.5359365983E-03,
     & 145.0918739064E-03,
     & 145.6461794876E-03,
     & 146.1988690346E-03,
     & 146.5259180059E-03/

*   Cumulative spectrum
      DATA CUMPR / 0.D0,
*...+....1....+....2....+....3....+....4....+....5....+....6....+....7..
     & 0.0037617826,
     & 0.0113572171,
     & 0.0190511735,
     & 0.026847045,
     & 0.0347484179,
     & 0.0427590866,
     & 0.0508830711,
     & 0.0591246358,
     & 0.0674883104,
     & 0.0759789135,
     & 0.0846015784,
     & 0.0933617824,
     & 0.1022653795,
     & 0.1113186368,
     & 0.1205282764,
     & 0.1299015219,
     & 0.1394461518,
     & 0.14917056,
     & 0.1590838253,
```

```
     & 0.1691957909,
     & 0.1795171563,
     & 0.1900595838,
     & 0.2008358222,
     & 0.211859852,
     & 0.2231470558,
     & 0.2347144202,
     & 0.246580777,
     & 0.2587670911,
     & 0.2712968098,
     & 0.2841962879,
     & 0.2974953106,
     & 0.311227742,
     & 0.3254323398,
     & 0.3401537886,
     & 0.3554440301,
     & 0.3713639983,
     & 0.3879859229,
     & 0.4053964425,
     & 0.4237009038,
     & 0.4430294459,
     & 0.4635458611,
     & 0.4854609439,
     & 0.5090534391,
     & 0.5347046021,
     & 0.5629589238,
     & 0.5946399536,
     & 0.6310973585,
     & 0.6748275437,
     & 0.7315147259,
     & 0.822172059,
     & 1/


*---------------------------------------------------------------------*
*...+....1....+....2....+....3....+....4....+....5....+....6....+....7..
*---------------------------------------------------------------------*
      NOMORE = 0
*  +--------------------------------------------------------------------*
*  |  First call initializations:
      IF ( LFIRST ) THEN
*  |  *** The following 3 cards are mandatory ***
        TKESUM = ZERZER
        LFIRST = .FALSE.
        LUSSRC = .TRUE.
*  |  *** User initialization ***
      END IF
*  |
*  +--------------------------------------------------------------------*
*  In order to cover the target volume in depth the energy must be
*  sampled from the ENEDGE, with cumulative weights from CUMPR
*  Sample the energy group
      XI = FLRNDM(DUMMY)
      DO 500 K = 1, 52
        IF(XI .LE. CUMPR(K)) THEN
          ENERGY = ENEDGE(K) -
     &    (XI-CUMPR(K-1))*(ENEDGE(K)-ENEDGE(K+1))/(CUMPR(K)-CUMPR(K-1))
          GO TO 600
        END IF
 500  CONTINUE
      STOP ' Failed to sample the energy group'
```

```
 600  CONTINUE
      kount=kount+1
*
*  Npflka is the stack counter: of course any time source is called it
*  must be =0
      NPFLKA = NPFLKA + 1
* Wt is the weight of the particle
      WTFLK (NPFLKA) = ONEONE
      WEIPRI = WEIPRI + WTFLK (NPFLKA)
* Particle type (1=proton.....). Ijbeam is the type set by the BEAM
* card
*  +-------------------------------------------------------------------*
*  |  Heavy ion:
      IF ( IJBEAM .EQ. -2 ) THEN
         IJHION = IPROZ  * 1000 + IPROA
         IJHION = IJHION * 100 + KXHEAV
         IONID  = IJHION
         CALL DCDION ( IONID )
         CALL SETION ( IONID )
         ILOFLK (NPFLKA) = IJHION
*  |
*  +-------------------------------------------------------------------*
*  |  Normal hadron:
      ELSE
         IONID  = IJBEAM
         ILOFLK (NPFLKA) = IJBEAM
      END IF
*  |
*  +-------------------------------------------------------------------*
* From this point .....
* Particle generation (1 for primaries)
      LOFLK (NPFLKA) = 1
* User dependent flag:
      LOUSE  (NPFLKA) = 0
* User dependent spare variables:
      DO 100 ISPR = 1, MKBMX1
         SPAREK (ISPR,NPFLKA) = ZERZER
 100  CONTINUE
* User dependent spare flags:
      DO 200 ISPR = 1, MKBMX2
         ISPARK (ISPR,NPFLKA) = 0
 200  CONTINUE
* Save the track number of the stack particle:
      ISPARK (MKBMX2,NPFLKA) = NPFLKA
      NPARMA = NPARMA + 1
      NUMPAR (NPFLKA) = NPARMA
      NEVENT (NPFLKA) = 0
      DFNEAR (NPFLKA) = +ZERZER
* ... to this point: don't change anything
* Particle age (s)
      AGESTK (NPFLKA) = +ZERZER
      AKNSHR (NPFLKA) = -TWOTWO
* Group number for "low" energy neutrons
      IGROUP (NPFLKA) = NEUGRP
* Kinetic energy of the particle (GeV)
* With Gaussian sigma 0.008 GeV
      CALL FLNRRN (RGAUSS)
      TKEFLK (NPFLKA) = ENERGY*(1+0.008D0*RGAUSS)
* Particle momentum
      PMOFLK (NPFLKA) = SQRT ( TKEFLK (NPFLKA) * ( TKEFLK (NPFLKA)
     *                      + TWOTWO * AM (ILOFLK(NPFLKA)) ) )
```

```
*  Cosines (tx,ty,tz)
      TXFLK  (NPFLKA) = UBEAM
      TYFLK  (NPFLKA) = VBEAM
      TZFLK  (NPFLKA) = WBEAM
*     TZFLK  (NPFLKA) = SQRT ( ONEONE - TXFLK (NPFLKA)**2
*    &                       - TYFLK (NPFLKA)**2 )
* Polarization cosines:
      TXPOL (NPFLKA) = -TWOTWO
      TYPOL (NPFLKA) = +ZERZER
      TZPOL (NPFLKA) = +ZERZER
* Particle coordinates
* cover the volume in X and Y direction
* Gaussiuan sigma 0.37 cm to account for lateral spread in beam
      CALL FLNRR2(RGAUS1, RGAUS2)
      XFLK (NPFLKA) = (-2.7 + 0.37D0*RGAUS1)+ FLRNDM(DUMMY)*5.4
      YFLK (NPFLKA) = (-2.7 + 0.37D0*RGAUS2)+ FLRNDM(DUMMY)*5.4
      ZFLK (NPFLKA) = -1.0
*  Calculate the total kinetic energy of the primaries: don't change
      IF ( ILOFLK (NPFLKA) .EQ. -2 .OR. ILOFLK (NPFLKA) .GT. 100000 )
     &   THEN
         TKESUM = TKESUM + TKEFLK (NPFLKA) * WTFLK (NPFLKA)
      ELSE IF ( ILOFLK (NPFLKA) .NE. 0 ) THEN
         TKESUM = TKESUM + ( TKEFLK (NPFLKA) + AMDISC (ILOFLK(NPFLKA)) )
     &          * WTFLK (NPFLKA)
      ELSE
         TKESUM = TKESUM + TKEFLK (NPFLKA) * WTFLK (NPFLKA)
      END IF
*  Flag this is prompt radiation
      LRADDC (NPFLKA) = .FALSE.
      RADDLY (NPFLKA) = ZERZER
*  Here we ask for the region number of the hitting point.
*     NREG (NPFLKA) = ...
*  The following line makes the starting region search much more
*  robust if particles are starting very close to a boundary:
      CALL GEOCRS ( TXFLK (NPFLKA), TYFLK (NPFLKA), TZFLK (NPFLKA) )
      CALL GEOREG ( XFLK  (NPFLKA), YFLK  (NPFLKA), ZFLK  (NPFLKA),
     &              NRGFLK(NPFLKA), IDISC )
*  Do not change these cards:
      CALL GEOHSM ( NHSPNT (NPFLKA), 1, -11, MLATTC )
      NLATTC (NPFLKA) = MLATTC
      CMPATH (NPFLKA) = ZERZER
      CALL SOEVSV
      RETURN
*=== End of subroutine Source ===========================================*
      END
```